

2007

Solid state diffusion in the lubricious film formation on iron by mixed tertiary butyl phenyl phosphates under static conditions

Steven Kent Shaeffer
University of Dayton

Follow this and additional works at: https://ecommons.udayton.edu/graduate_theses

Recommended Citation

Shaeffer, Steven Kent, "Solid state diffusion in the lubricious film formation on iron by mixed tertiary butyl phenyl phosphates under static conditions" (2007). *Graduate Theses and Dissertations*. 5517.
https://ecommons.udayton.edu/graduate_theses/5517

This Dissertation is brought to you for free and open access by the Theses and Dissertations at eCommons. It has been accepted for inclusion in Graduate Theses and Dissertations by an authorized administrator of eCommons. For more information, please contact mschlange1@udayton.edu, ecommons@udayton.edu.

SOLID STATE DIFFUSION IN THE LUBRICIOUS FILM FORMATION ON IRON
BY MIXED TERTIARY BUTYL PHENYL PHOSPHATES UNDER STATIC
CONDITIONS

Dissertation

Submitted to

The School of Engineering of the

UNIVERSITY OF DAYTON

In Partial Fulfillment of the Requirements for

the Degree

Doctor of Philosophy in Materials Engineering

by

Steven Kent Shaeffer


UNIVERSITY OF DAYTON

Dayton, Ohio

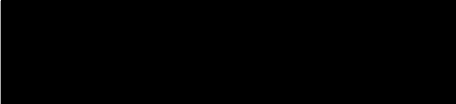
May 2007

SOLID STATE DIFFUSION IN THE LUBRICIOUS FILM FORMATION ON IRON
BY MIXED TERTIARY BUTYL PHENYL PHOSPHATES UNDER STATIC
CONDITIONS

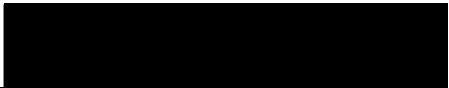
APPROVED BY



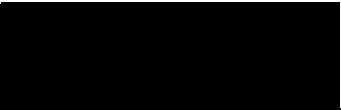
Kevin J. Myers, D.Sc., P.E.
Advisory Committee Chairman
Professor, Chemical and Materials
Engineering Department




Paul T. Murray, Ph.D.
Committee Member
Professor, Materials Engineering
Department



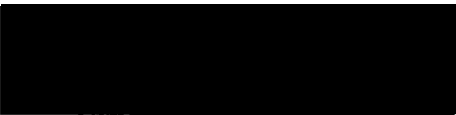
Nelson H. Forster, Ph.D.
Committee Member
Research Scientist, Mechanical
Systems Branch, Air Force
Research Laboratory



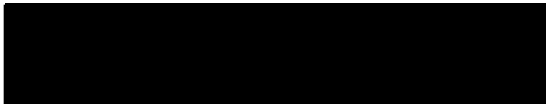
Peter John, Ph.D.
Committee Member
Senior Research Physicist
University of Dayton Research Institute




Donald L. Moon, Ph.D.
Associate Dean
Graduate Engineering Programs & Research
School of Engineering



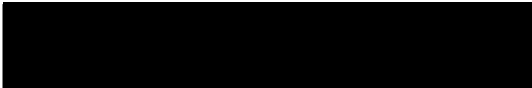
James A. Snide, Ph.D.
Committee Member
Professor Emeritus, Chemical
and Materials Engineering
Department



Muhammad N. Islam, Ph.D.
Committee Member
Professor, Mathematics
Department



Robert L. Wright, Jr., Ph.D.
Committee Member
Turbine Branch, Air Force
Research Laboratory



Joseph E. Saliba, Ph.D., P.E.
Dean, School of Engineering

ABSTRACT

SOLID STATE DIFFUSION IN THE LUBRICIOUS FILM FORMATION ON IRON BY MIXED TERTIARY BUTYL PHENYL PHOSPHATES UNDER STATIC CONDITIONS

Name: Shaeffer, Steven Kent
University of Dayton, 2007

Advisor: Dr. Kevin J. Myers

The reaction between vaporous aryl phosphate esters and iron is known to yield a lubricious product film at high temperatures. The rate law exhibited in the growth of this film is consistent with a diffusion controlled process. In this work the actual movement of elements during this growth process was characterized using laminated metal foil samples consisting of a 1,000 Å iron film deposited on a platinum substrate. The interface between the platinum and iron served as a reference datum against which the movement of the elements was observed. Iron was found to be the lone mobile element that diffuses through the product layer where it reacts with the vapor at the exposed surface generating more product. The change in the concentration profiles of the iron within the product served as a means to evaluate the diffusivity of the iron during the product growth. In this case the diffusivity of iron was found to be greater than its self

diffusivity and within the range of values typical of iron oxide. This data in combination with the estimated activation energy for the process suggested that the diffusion was of a nature similar to the vacancy diffusion displayed in the oxidation of iron. The data suggests that the diffusion of iron through the product is the rate controlling step in the product growth process.

ACKNOWLEDGMENTS

The funding for this work was supplied by the Mechanical Systems Branch, Air Force Research Laboratory. Special thanks to Dr. R. Wright, III, for allowing the use of his facilities for this work and to Dr. T. Wittberg, University of Dayton, for AES data, Dr. J. Sanders, Air Force Research Laboratory, for the iron/platinum PVD, and Dr. Nelson Forster, Air Force Research Laboratory, for his invaluable suggestions and advice. Special thanks also to Dr. T. Murray for his suggestions in interpreting AES data. Many thanks also to Dr. K. Myers, my advisor, for his advice and direction in navigating this research effort to its successful conclusion.

TABLE OF CONTENTS

ABSTRACT	iii
ACKNOWLEDGMENTS	v
LIST OF ILLUSTRATIONS	viii
LIST OF TABLES	xii
CHAPTER	
I. INTRODUCTION	1
Synopsis	
Motivation	
Selection of Materials	
Reactivity of Liquid Lubricant Base Stock	
Reactivity on the Addition of Phosphorous Based Compounds	
Reactivity in VPL Utilizing Phosphorous Based Compounds	
Potential Role of Diffusion in VPL Reactions	
Summary	
II. EXPERIMENTAL	24
TBPP	
Carrier Gases	
Iron Foil	
1010 Steel Foil	
Iron/Platinum Laminated Foil	
Silicon Nitride	
Iron (III) Phosphate	
Experimental Equipment and Procedures	
III. RESULTS	51
Carrier Gas Effects	

	Product Formation	
	Product Formation Model	
IV.	DISCUSSION	112
	Equipment	
	Carrier Gases	
	Sample Constituents	
	Product Constituents	
	Product Formation	
V.	CONCLUSIONS	140
VI.	RECOMMENDATIONS FOR FUTURE WORK	143
	REFERENCES	145

LIST OF ILLUSTRATIONS

1. Schematic representation of product formation process	3
2. Phosphate ester molecular structures: TCP (A), TBPP (B)	7
3. Molecular structure of TCP (A), tolyl-TCP (B), and <i>t</i> -butyl phenol (C)	18
4. Molecular structure of di(<i>t</i> -butyl phenyl) phenyl phosphate	25
5. FTIR diffuse reflectance spectra of TBPP on iron	27
6. SEM image of iron foil surface	29
7. EDS of iron foil surface	30
8. Concentration-depth profile of iron/platinum laminated foil; ○-platinum, □-iron, Δ-oxygen, *-carbon	33
9. Diagram of the modified TGA and vapor generator assembly	35
10. Evaporation rate of TBPP in several gases	43
11. Syringe pump output	45
12. TGA weight change anomaly at start-up	47
13. TGA furnace temperature change on start-up	49
14. Weight gain by 1010 steel in nitrogen carrier gas	53
15. Weight gain by iron in nitrogen carrier gas	54
16. Weight gain by iron in helium carrier gas	55
17. Iron weight gain on exposure to TBPP vapor in nitrogen carrier gas; ○ - 300° C, □ - 400° C.....	58

18. Iron weight gain on exposure to TBPP vapor in nitrogen carrier gas; Δ - 450° C, \circ - 500° C, \square - 600° C	59
19. Iron weight gain on exposure to TBPP vapor in helium carrier gas; Δ -400° C, \circ -500° C, \square -600° C	60
20. Weight gain by iron/platinum laminated foil on exposure to TBPP vapor in helium carrier gas at 500° C	61
21. Normalized weight gain by iron (III) phosphate on exposure to TBPP vapor in the nitrogen carrier gas at 400° C	63
22. Normalized weight gain by iron (III) phosphate on exposure to TBPP vapor in the nitrogen carrier gas at 500° C.....	64
23. SEM micrograph of iron sample after exposure to TBPP vapor in nitrogen carrier gas at 400° C	66
24. SEM micrograph of the edge of an iron sample after exposure to TBPP vapor in the nitrogen carrier gas at 400° C	67
25. SEM micrograph of detached product on iron sample surface after exposure to TBPP vapor in nitrogen carrier gas at 400° C	68
26. SEM micrograph of the product attached to an iron sample after exposure to TBPP vapor in nitrogen carrier gas at 400° C	69
27. FTIR scan of product formed on iron by exposure to TBPP vapor at 300° C in helium	70
28. FTIR scan of substrate beneath product form on iron by exposure to TBPP vapor at 300° C in helium	71
29. FTIR scan of product formed on iron by exposure to TBPP vapor at 400° C in helium	72
30. FTIR scan of substrate beneath product formed on iron by exposure to TBPP vapor at 400° C in helium	73
31. FTIR scan of product formed on iron by exposure to TBPP vapor at 500° C in helium	74
32. FTIR scan of substrate beneath product formed on iron by exposure to TBPP at 500° C in helium	75

33. FTIR scan of product formed on iron by exposure to TBPP vapor at 600° C in helium	76
34. FTIR scan of substrate beneath product formed on iron by exposure to TBPP at 600° C in helium	77
35. EDS of iron foil exposed to TBPP vapor in nitrogen at 400° C	80
36. Iron/platinum laminated foil sample after exposure to TBPP vapor at 500° C	82
37. Concentration-depth profile for a laminated iron/platinum foil. ○-Platinum, □-Iron, Δ-Oxygen, +Phosphorous, *-Carbon	83
38. Concentration-depth profile for a laminated iron/platinum foil after a 30 minute exposure to a helium/TBPP mixture. ○-Platinum, □-Iron, Δ-Oxygen, +Phosphorous, *-Carbon	84
39. Concentration-depth profile for a laminated iron/platinum foil after a 70 minute exposure. ○-Platinum, □-Iron, Δ-Oxygen, +Phosphorous, *-Carbon	85
40. Concentration-depth profile for a laminated iron/platinum foil after a 70 minute exposure to trace TBPP vapor in helium, ○-Platinum, □-Iron, Δ-Oxygen, +Phosphorous, *-Carbon	86
41. Peak Auger electron energies for phosphorous, 110.00 eV, 112.50 eV, ----- 115.00 eV, ——— 116.25 eV	91
42. Adjusted concentration-depth profile for a laminated iron/platinum foil after a 30 minute exposure to TBPP vapor in helium, ○ -Platinum, □ -Iron, Δ-Oxygen, +Phosphorous, * -Carbon	95
43. Adjusted concentration-depth profile for a laminated iron/platinum foil after a 70 minute exposure to TBPP vapor in helium, ○ -Platinum, □ -Iron, Δ -Oxygen, +Phosphorous, * -Carbon	96
44. Adjusted concentration-depth profile for a laminated iron/platinum foil after a 70 minute exposure to trace TBPP vapor in helium, ○ -Platinum, □ -Iron, Δ -Oxygen, +Phosphorous, * -Carbon	97
45. Identification of zones on concentration-depth profile	98
46. Change in product concentration-depth profiles for 30 (left) and 70 (right) minute samples	101

47. Model of changing concentration-depth profile	102
48. Arrhenius plot of product growth rate constant	110
49. Extent of reaction in nitrogen (\square) and helium (\circ) carrier gases	115

LIST OF TABLES

1. Fluid flow data and calculated Reynolds numbers (N_{re}) for helium and nitrogen gases within the TBPP vapor generator	37
2. Auger electron energies of the elements within the iron layer of an unexposed sample of laminated foil	87
3. Auger electron energies of the elements within the iron layer of a sample of the laminated foil exposed for 30 minutes to TBPP vapor in helium at 500° C	88
4. Auger electron energies of the elements within the iron layer of a sample of the laminated foil exposed for 70 minutes to TBPP vapor in helium at 500° C	89
5. Model correlation coefficients for TBPP vapor/helium reaction on iron	107
6. Model correlation coefficients for TBPP vapor/nitrogen reaction on iron	108
7. Thermal expansion properties for various materials	125
8. Densities of selected iron compounds	131
9. Iron diffusivities in various iron oxides	137

CHAPTER I

INTRODUCTION

Synopsis

Previous work has clearly demonstrated that mixed tertiary butyl phenyl phosphates (TBPP) in vapor form will interact with ferrous surfaces at high temperatures to form a solid product that exhibits lubricious characteristics. This interaction involves chemical reactions that yield a surface product through which a diffusion of reactants and/or products may take place and contribute to the further formation of this product. Heretofore it has remained unknown which of these elements move within the product, the driving force for this movement, and to what extent this movement contributes to and/or controls the overall rate at which the product forms. The discourse within this and subsequent chapters describes the work performed to identify any mobile elements within the product and to explore the origin and effect that this motion has on the overall rate of the product formation.

The results of this work demonstrate that the mechanism involved in the product formation just after an initial product has formed is a type of flat-plate variation of the classic "shrinking core" model for solid-gas reactions. In this particular case the overall process is controlled by iron diffusion through the solid product layer where it is made available to chemically react with the vapor at the exterior surface generating additional

product. This model is displayed graphically in Figure 1. Furthermore, the results suggest that the iron diffuses through the product layer in the form of cations where the rate of diffusion is controlled by concentration gradient of iron throughout the thickness of the product layer.

Motivation

The potential for higher power and greater fuel efficiency in gas turbine and internal combustion engines is motivating the development of new engines which are smaller, lighter, and able to operate at higher temperatures. A widely recognized critical piece of this development is the creation of a new ensemble of heat-tolerant, high specific strength structural materials. An equally important but often less recognized piece of this development is the formulation of heat-tolerant operational fluids and lubricants. The fluids used in these advanced systems must perform reliably while operating at temperatures reaching well in excess of 300° C where conventional liquid lubricants suffer from excessive oxidation, thermal decomposition, and a detrimental loss of viscosity [1-3]. In response to this need, specialty synthetics, additives, and alternative lubrication schemes continue to be devised. One such alternative scheme is the use of solid phase materials as opposed to the conventional liquid phase lubricants. In solid phase schemes a solid lubricious film is either directly pre-applied to the load bearing surfaces under static conditions or the film is generated from a powdered material that is continuously fed to the surfaces under dynamic load conditions. Although solid phase lubricants are very tolerant of high temperatures, they have thus far been unable to provide sufficient lubrication for extended periods of time and for bearing speeds

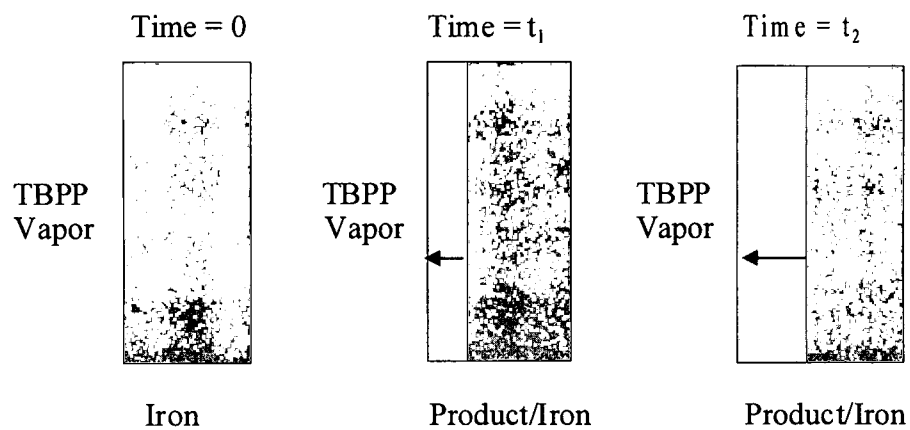


Figure 1. Schematic representation of overall product formation process.

characteristic of gas turbine engines, viz., 1.5 - 2.5 million DN (product of shaft diameter in millimeters and shaft speed in rpm) [4]. A somewhat more unconventional scheme which also generates a solid film lubricant is known as vapor phase lubrication (VPL). In VPL the solid film is generated by the use of a vaporous chemical reactant as opposed to a solid phase material. In the VPL scheme, a chemical compound precursor is first vaporized and then continuously transferred to the load bearing surfaces where it chemically reacts to form a lubricious solid film product that is continuously regenerated. This regeneration takes place as the solid product is worn away exposing the underlying surface to the surrounding vapor which reacts with the surface to produce more of the product. As in the case of solid phase lubricants, the presence of this solid film prevents or minimizes the surface-to-surface contact which leads to adhesion and subsequent friction and wear [5, 6]. Since in this scheme the lubricating precursor is used in the form of a vapor, unlike lubricants in a liquid form, the cooling of the precursor compound or the lubricating reaction product is unnecessary. Without the need for a cooling system such as that used in conventional liquid lubricants, a system based on VPL might weigh as little as 10 percent of a comparable lubrication system based on a conventional low-temperature liquid lubrication scheme [7]. For a typical gas turbine engine this reduction in lubrication system weight could lead to an overall engine weight reduction on the order of 15 percent. In addition, since some engines utilize the system's fuel to help cool the conventional liquid lubricant, the use of VPL would eliminate this need to use the fuel as a heat sink and would reduce the overall heat load on the fuel in these cases. Former engine related work [7, 8] has demonstrated that VPL is able to maintain sufficient lubrication of high speed bearings for limited periods of time, viz., several hours. For this

reason, VPL has been considered for use by the U.S. Air Force in small expendable gas turbine engines and the possible lubrication of back-up bearings in the magnetic bearing subsystems intended for manned rated engines.

Although in recent years the focus on VPL as an alternate lubrication scheme has diminished, there remains a desire to understand the process by which the vapor interacts with solids to form this lubricious film. To this end, this work builds on previous work by focusing on the portion of the process that directly follows the initial reaction between the vapor and the solid and provides a more complete understanding of this process.

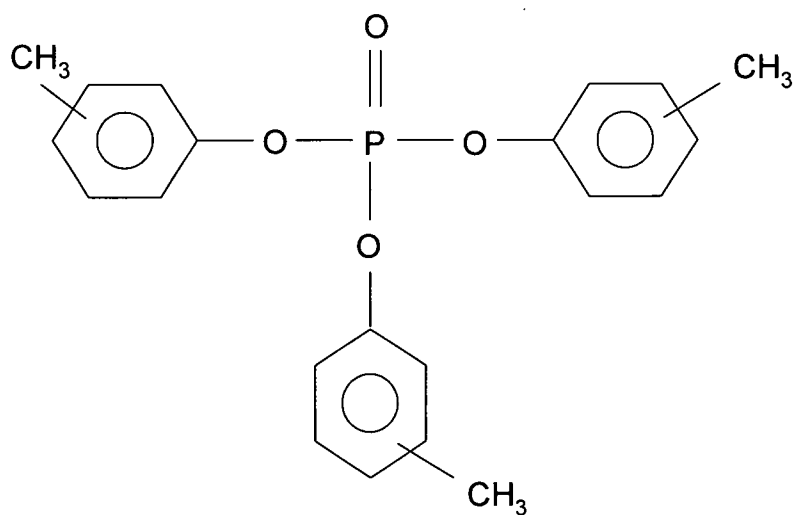
Selection of Materials

The search for compounds that react with ferrous metal surfaces to yield a lubricious film product has been ongoing for more than 40 years. The compounds which have been investigated are quite diverse and include hydrocarbons, halogenated hydrocarbons, sulfides, and alkyl or aryl phosphate esters [9-26]. The aryl phosphate esters as a class have been found to possess characteristics which are very different from these other types of compounds and exhibit particular advantages in VPL schemes. These characteristics include low vapor pressures, high flash points, high auto-ignition temperatures and excellent thermal, hydrolytic, and oxidative stability especially as compared to the hydrocarbons [27]. The aryl phosphate esters thus pose a relatively low risk of fire and explosion hazard when used in mixtures with air at high temperatures. Tricresyl phosphate (TCP) is one such aryl phosphate ester that is commercially available and has demonstrated an exceptional potential to perform both as an anti-wear liquid lubricant additive and as a potential VPL precursor. With an established record of successful use

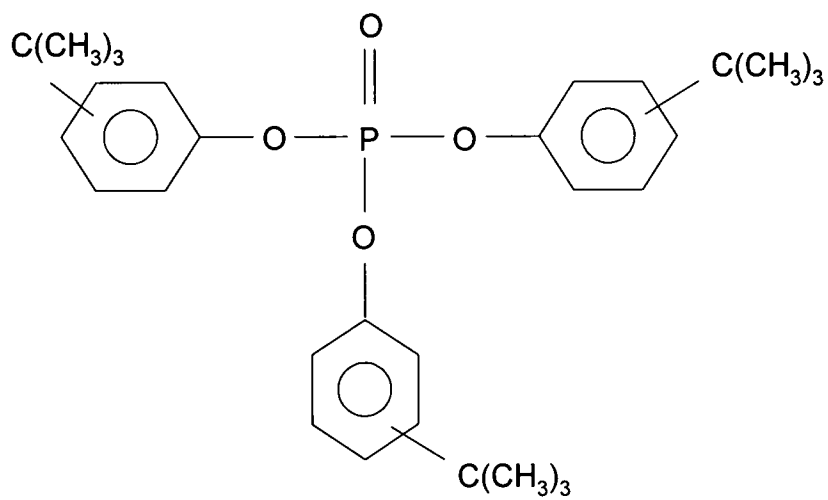
as an anti-wear additive, TCP remained the focus of a great deal of lubricant related research for many years especially in work related to VPL. Commercial formulations of TCP involve a mixture of structural isomeric forms in which the differences among the isomers are found in the toluene moiety of the molecule. The isomers themselves have been found to exhibit toxicities over a wide range [26, 28-31]. Additionally, commercial formulations of lubricants which contain TCP also often contain trimethylol propane esters which in high temperature environments may react with other less toxic isomeric forms of TCP to form compounds with acute neurotoxic properties [32]. Concerns regarding this toxicity motivated research efforts to be redirected toward the development of other less toxic but chemically similar compounds with a performance that matches that of TCP. Tertiary butyl phenyl phosphates are structurally similar types of aryl phosphate esters which behave chemically much like TCP but exhibit a reduced propensity for neuroleptic activity. It is for this reason that TBPP has been selected for use in this work. The structural similarity between TCP and TBPP can be seen in Figure 2.

Reactivity of Liquid Lubricant Base Stock

Before the advent of the VPL schemes, research was being conducted on the use of phosphate esters including TCP as potential extreme pressure and anti-wear additives to liquid lubricants. TCP has since become one of the most common anti-wear additives used in aviation engine lubricants. As the name implies, these additives serve to reduce the wear that occurs under the boundary lubrication conditions imposed by high loads. Here, as in VPL schemes, the additive chemically reacts with the surfaces to form a



(A)



(B)

Figure 2. Phosphate ester molecular structures: TCP (A), TBPP (B).

product which inhibits the adhesion that results in high friction and wear. However, the chemical reactions taking place on surfaces treated with an additized lubricant are not confined to the additive compounds only. Neat base stock materials such as mineral oil at relatively low temperatures will undergo chemical changes on load bearing surfaces. This adds to the complexity in attempts to describe the overall surface reaction. Additional complexity is encountered when other factors are considered. For example, a number of researchers have attributed the formation of lubricious materials between load bearing surfaces to the mechanical action imposed on the liquid by the movement and contact between the surfaces. Examples of work that would appear to substantiate this claim include that by DeKoven and Mitchell [35] who reported that in the relatively low temperature range of 80° to 130° C and under the dynamic conditions of friction testing, poly-phenyl ether will react on the surface of both clean and oxidized steel. The reaction product is composed of both aliphatic and oxidized carbon with the reaction occurring to the greatest extent within the contact zone as opposed to other surfaces. Others have found that a lubricious polymer can form between two load bearing surfaces via a process referred to as "tribopolymerization" [33]. This type of process has also been suggested as being instrumental in the formation of a lubricious product from hydrocarbon vapors on un-reactive ceramic surfaces at temperatures between 120° and 165° C [34]. In most if not all of these cases, the solid surfaces have not been credited with any chemical involvement in the reaction(s) taking place, either as a reactant or as a catalyst. However, it is well known that the interaction between metal surfaces and hydrocarbon based oils especially in the presence of dissolved oxygen leads to the formation of organic surface deposits. In relation to this, the desire to develop hydrocarbon fuels that are resistant

to high heat loads has prompted a great deal of this type of research and a number of fuel additives have been developed to keep these deposits from forming on the surfaces of engine fuel hardware. At 250° C this process is characterized by an oxidative degradation that yields an organo-metallic product [36]. The presence of excess oxygen has been found to accelerate the reaction between steel surfaces and fluorinated alkyl ethers in the liquid phase without the involvement of mechanical contact at temperatures between 200° and 400° C [37].

The chemically bound oxygen within a reactant promotes similar behavior. Based on work with poly-glycols, Cowley et al. suggested that the boundary lubrication properties of these glycols is due to the oxidation products such as carboxylic acid forming on and subsequently reacting with metallic surfaces [38]. This oxidative decomposition was reported to include the formation of iron oxide and was believed to be initiated by the available "frictional energy." At higher temperatures, amorphous carbonaceous surface compounds are formed from hydrocarbon vapors. For example, Lauer and Dwyer [14] investigated the product formation on various ceramic surfaces in contact with each other while enveloped by hydrocarbon vapors at temperatures ranging from 25° to 700° C. They found the surface product to be a deposit composed of a carbon rich material formed by the pyrolysis of the adsorbed gases. A similar finding was reported by Barnick et al. [25]. They found that acetylene/nitrogen mixtures formed a lubricious carbonaceous film on both ceramic and metallic surfaces at 520° C during pin-on-disk friction testing.

Reactivity on the Addition of Phosphorous Based Compounds

This work on liquid and gas phase hydrocarbons provided a background for similar work involving organo-phosphorous compounds. Most initial work was geared toward understanding the mechanism by which organo-phosphorous compounds were able to impart certain anti-wear properties to the hydrocarbon based liquid lubricants for which they served as anti-wear additives. The results of early work with organo-phosphorous lubricant additives by Beeck et al. led to the initial postulation that the additives reduced wear via a chemical polishing process. In this proposed process, a reaction takes place between the metallic surface and the additive creating a low melting point metal phosphide eutectic mixture [39, 40]. Under load this eutectic compound would then be plastically deformed and/or melted and wiped across the surface by the mechanical action of the sliding contact resulting in the creation of a smoother surface which could be better lubricated. Since the temperature within the contact zone can easily approach the melting point of the materials in contact loading [41], this appeared to be the most plausible explanation. Following this, Furey [42] used TCP in a ball-on-cylinder metal wear testing device to demonstrate that although the use of TCP resulted in a decrease in wear, it did not smooth the contacting surfaces to any significant extent. Later work with ferrous alloys and aryl phosphate esters including TCP also refuted this chemical polishing explanation suggesting rather that the surface wear reduction was due to the presence of a surface reaction product consisting principally of iron phosphate instead of a eutectic reaction product [43-47, 59]. Using commercial grade TCP containing radioactive P^{32} , Klaus and Bieber [48] found that the interaction between a ferrous surface and TCP also involved reactions with the polar acid phosphate impurities

contained in the original mixture of TCP and base stock oil or those generated during the surface interactions. Typical commercial production processes for technical grade TCP are known to generate small amounts of byproduct consisting of chlorinated compounds and acid phosphates which appear as contaminants [40, 49, 50]. Additionally, aryl phosphate esters such as TCP, along with alkyl phosphate esters, can thermally decompose to a certain extent on heating. Along with this decomposition, other reactions can take place. One example is the polymerization that can occur on the exposure of liquid phosphate ester materials to oxygen at relatively low temperatures [58]. These same materials can to a greater extent oxidize or hydrolyze in the presence of air and moisture to form acid phosphates especially in the presence of metals and metal oxides [39, 44, 48, 49, 51-55]. These acid phosphate impurities were then presumed to react with ferrous surfaces in a manner similar to that of phosphoric acid. This reaction is known to form a product consisting of mixed ferric and ferrous phosphates [56]. The concentration of acid phosphate impurities was found to somewhat correlate with the extent to which the mixture provided anti-wear protection. For this reason, the wear reduction capability of aryl phosphate esters such as TCP was for a time attributed to the iron phosphate products resulting from the reaction of iron with the various acid phosphates ever present as original contaminants and decomposition byproducts [49]. Although there is no doubt that to some extent the phosphate acids contribute to the production of a lubricious surface film, other work has shown that they are not the primary reacting species. Work by Goldblatt and Appeldoorn [54] opposed that of Klaus and Bieber by suggesting that the lubricating ability of TCP is actually independent of any oxidation or hydrolysis products in the TCP. Using X-ray photoelectron spectroscopy

(XPS), Faut and Wheeler [57] found that phosphorous, exclusively in the form of iron phosphate, was generated on the surface of iron pins during friction testing. They utilized a pin-on-disk tribometer with M-50 tool steel disks at temperatures ranging from 280° to 390° C. Phosphorous in the form of iron phosphate was also found through the use of X-ray diffraction and Auger Electron Spectroscopy (AES) to be the predominant product formed in the electro-deposition reaction between steel and liquid mixed organic phosphate materials [53]. Kasrai et al. [60, 61] compared the XPS spectra of several known phosphate glasses to the spectra of the product film formed on steel when exposed to mixtures of zinc dialkyl dithio phosphate under both static and dynamic wear conditions at 150° C. They found that phosphate polymers were formed with oxygen serving as the bridge between individual polymer molecules. Fuller et al. [62] found that in air, the decomposition of several types of alkyl and aryl zinc dithio phosphates would occur at lower temperatures when in the presence of steel but would require high temperatures when no steel surface was present. The decomposition product in this case was a polyphosphate compound. They also reported that the aryl substituted form of the additive was more stable at higher temperatures than the alkyl form. Tung et al. [47] found that a product containing a mixture of amorphous and microcrystalline phases was formed on cast iron surfaces when exposed to dilauryl hydrogen phosphate mixed with mineral oil. This product was formed by passing low level electrical current normal to the oil/iron interface. X-ray diffraction analysis suggested that the film was composed of a mixture of iron (II) orthophosphate and iron carbonate. After subjecting this coated cast iron surface to 30 hours of wear at temperatures equal to or less than 100° C, the content

of the product was found to consist mainly of carbon and a smaller amount of oxygen and phosphorous.

Changes in chemical bonding at relatively low temperature (viz. 80° C) in elastohydrodynamic sliding contacts between steel and diamond were investigated by Cann and Spikes [63] using bisoctyl phenyl phosphonate as an additive to several base stock oils. They found that a product film developed which contained inorganic material based on phosphorous, oxygen, and metal along with a lesser amount of organic material. Changes in infrared (IR) absorption during dynamic loading indicated that the product formation involved the development of a $\text{P=O} \rightarrow \text{Fe}$ bond. Without reference to temperature, Ma et al. [64] reported that iron oxide in the form of an "oxy-nitrided" surface film actually promoted the surface reaction with TCP in the liquid phase. In this work they found surface product films consisting of iron phosphate. Placek and Shankwalker [24] investigated the product formation on steel surfaces using liquid TCP, trioctyl phosphate, and isopropyl phenyl phosphate at various temperatures. They found that at temperatures below 250° C the product film contained high levels of hydrocarbon, lower levels of iron phosphates and poly-phosphates, and small amounts of iron phosphide. At a temperature of 300° C, the resulting product contained a lower proportion of hydrocarbon and high levels of iron phosphates and poly-phosphates. The role played by iron in these types of surface reactions was investigated by Wang and Tung [65] using an electrochemical cell. In this work, a mixture of acid phosphate and mineral oil was placed in a small gap between two cast iron electrodes while electrical current traversed the gap at room temperature. The product film consisted of an iron phosphate and organic material at the anode that was consistently found to be thicker than that

which was found at the cathode. They concluded from this work that the generation of ferrous ions by the loss of two or more electrons may be integral to the overall reaction mechanism.

In an attempt to better define the mechanism involved in the reaction between TCP and iron, Wheeler and Faut [17] used XPS to examine the vaporous adsorption of TCP onto, and the subsequent reaction with, an iron surface under partial vacuum conditions. At room temperature the adsorption rate of TCP vapor by clean iron and iron oxide (Fe_2O_3) surfaces were found to be the same. They also found that a chemical reaction on the iron and iron oxide surfaces only took place at temperatures higher than 200°C . The reaction on both of these types of surfaces produced a product consisting of iron phosphate and iron organo-phosphate. This reaction resulted in the loss of toluene groups from each of the TCP molecules. The proposed adsorption/reaction mechanism involved P-O-Fe and $\text{P}=\text{O} \rightarrow \text{Fe}$ bond formation. The establishment of this phosphoryl-iron bond formation was also found by Lacey, Kelsall, and Spikes [66] on the exposure of iron to various phosphonates at lower temperatures ($\leq 180^\circ\text{C}$). They reported that the phosphoryl-iron bond was found to be stable at a temperature of 170°C . The surface product appeared to be a polymer consisting of Fe (III) complexed with mono-alkyl phosphate ligands. Much of the liquid phase work described above served as a forerunner to the work investigating the use of phosphorous based compounds in VPL.

Reactivity in VPL Utilizing Phosphorous Based Compounds

The development of VPL as a viable high-temperature lubrication scheme actually originated with work performed by Klaus [10]. In his work with Graham it was

discovered that VPL using di-*t*-butyl phenyl di-phenyl phosphate at 370° C was as effective at wear reduction as the use of mineral oil in the liquid phase at room temperature. This work involved the use of a 4-ball wear tester modified to accept vaporous lubricant to quantify the wear reduction provided by vaporous aryl phosphate esters. Similarly, vaporous TCP at 370° C was found to reduce wear to the same extent as that found using liquid phase 10 W 30 SF-CD motor oil at room temperature [18]. As one might expect, much of the chemistry involved in the surface reactions of these anti-wear additives in the liquid phase has also been found to be involved in the surface reactions with vapor phase lubricants. Klaus et al. investigated the rate of the reaction between TCP and a variety of materials, viz. quartz, tungsten, nickel, copper, stainless steel, and iron under static conditions and over a temperature range of 500° to 800° C. A solid product film was found to form on all surfaces. The activation energy associated with this product formation was estimated to be 26.8 Kcal/mole for the copper, 37.1 Kcal/mole for the stainless steel, and 59.8 Kcal/mole for the quartz surfaces. For an extended reaction time, the resulting thick deposit on stainless steel was found to be associated with an activation energy of 51.9 kcal/mole.

Makki and Graham [67, 68] investigated the reaction of vaporous TCP on the ceramic surfaces of silicon carbide, silicon nitride, and also on a chrome-nickel alloy that contained 14 percent iron. The exposures lasted 60 seconds at temperatures ranging from 500° to 900° C. They found that the deposits which formed on the surface of the alloy were adherent while the deposits which formed on the ceramics were lacking texture and did not adhere to the substrate to any great extent. They concluded from this that the initial deposit which formed on the ceramics was due to physical adsorption and that

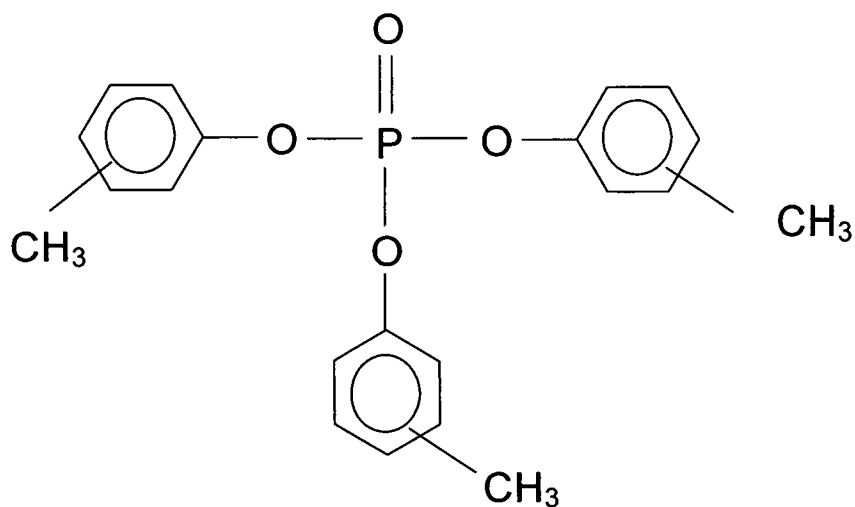
which formed on the alloy was due to chemisorption. Hanyaloglu and co-workers [15, 16] found that an adherent product would not form from vaporous TCP on the ceramic sialon or on a nickel based super-alloy at a temperature of 500° C. They found that if iron oxide (Fe_2O_3) was first deposited on the surface, then the product which formed would adhere to the surface. Wear testing of the films at 500° C resulted in the formation of a polymeric substance consisting of phosphorous, carbon, and oxygen with an average molecular weight of 30,000 g/mole. Other work by Forster and Trivedi [69, 70] has shown that bearing systems lubricated with vaporous TBPP and unformulated polyalpha olefins performed better when the bearing surfaces were composed of a ferrous material as opposed to a nonferrous material. Using the same type of wear testing equipment used by Klaus et al. [71] showed that iron phosphate was formed on steel when exposed to TCP and oleic acid vapor in a nitrogen carrier gas at 370° C. Using steel balls and a silicon nitride disk, they also found that the surface of the silicon nitride was oxidized during these tests. Other work such as that by Makki and Graham (mentioned earlier) has shown that the inclusion of oxygen as a reactant leads to an increase in the rate of the surface product formation.

This influence of surface oxygen on the reaction mechanism and subsequently on the reaction rate for ferrous substrates has also been established by the unpublished work of Johnson et al. [72] and in recent published work by Saba and Forster [73]. When oxygen is readily available at the surface, TCP vapor will react at the surface to yield vaporous byproducts with the predominant species being cresol. This implies that the P-O bond of the TCP is cleaved during the process. When less oxygen is present the dominant byproduct is tolyl-TCP implying the cleavage of the C-O bonds. Reactions under similar

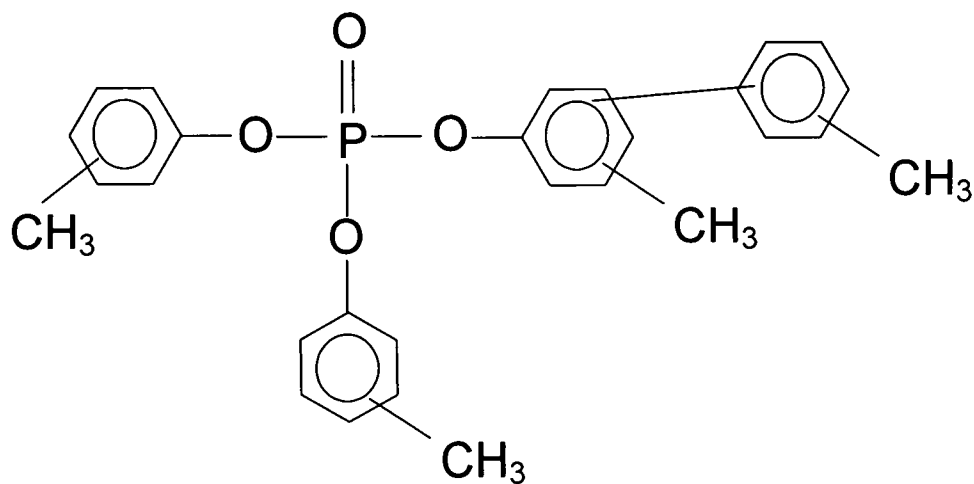
conditions using tri (*p*-*t*-butyl phenyl) phosphate at 425° C yielded vaporous byproducts of *t*-butyl phenol once again implying P-O bond cleavage. The molecular structures of these byproducts can be seen in Figure 3. At temperatures above 450° C, none of the volatile byproducts contained phosphorous implying that all of the phosphorous was contained in the solid product that formed on the surface. This result is similar to past work on the thermal decomposition of TCP and other phosphate esters as studied by Paciorek et al. [74, 75]. In this work a simple glass bulb containing liquid phosphate ester was heated to 370° C in the presence of air. For TCP, the main volatile decomposition products were found to be water, carbon dioxide, toluene, and various cresols. None of the volatile products were phosphorous containing compounds implying that the residue product film remaining on the glass surface was phosphorous based. Other surface elements such as carbon apparently also influence the surface reaction mechanism. Sung and Gellman [76, 77] found that all three isomers of TCP initially experience P-O bond cleavage on clean iron surfaces which have a significant carbon concentration.

Potential Role of Diffusion in VPL Reactions

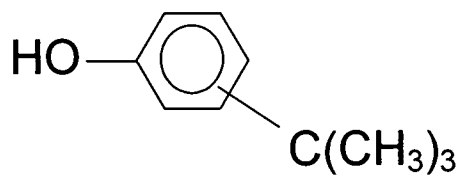
The form of the rate laws describing the kinetics of the reactions between phosphate ester vapors and various substrates has also been found to depend on the substrate composition. In the work by Klaus et al. [18] the rate of reaction between TCP and quartz or nickel at 700° C was found to follow a linear kinetic rate law, i.e. the reaction rate was found to be a linear function of time.



(A)



(B)



(C)

Figure 3. Molecular structure of TCP (A), tolyl-TCP (B), and *t*-butyl phenol (C).

On surfaces of iron, copper, stainless steel, and tungsten, the kinetic rate law was found to be nonlinear. Moreover, the reaction involving iron displayed a form in which the rate of reaction was found to be inversely proportional to the amount of product formed. This type of rate law is a characteristic of the shrinking core model described earlier. Other work by Klaus et al. [78] verified this linear rate law for the reaction of TCP on quartz and demonstrated that a temperature higher than 500° C is required to obtain any discernable product on quartz under the particular experimental conditions used in their work. The nonlinearity in the rate law involving TCP and iron was also observed by Hanyaloglu and Graham [13] at lower temperatures. Moreover, the product growth rate on the ceramic surfaces of sialon were strictly linear in nature. The nonlinear kinetic rate law which characterizes the product growth on pure iron is the same form of rate law observed in the oxidation of many metals where the oxide film is continuous and adherent. In these cases, the film formation is controlled by the diffusion of one or more reactants through the film. The continuously decreasing rate of the oxide film growth is due to the increased thickness of the oxide film through which the metal or other materials must diffuse. By analogy, the nonlinear rate of product film formation by TCP reacting on ferrous surfaces adds credence to the initial proposition by Klaus that certain metal surfaces act as catalysts for the reaction with the TCP and that the observed decrease in growth rate is due to the decreased transport rate of TCP, surface reaction products of TCP, or other materials through the surface product [79]. Klaus et al. investigated the composition of the product formed on iron by reaction with vaporous TCP at 700° C. The product was particulate in nature and consisted of iron carbides and phosphides nearest to the iron substrate followed by carbides and phosphides with lower

concentrations of iron further away from the iron substrate. This was followed by an amorphous zone containing iron phosphate with the lowest level of iron appearing furthest from the iron substrate. The decreasing concentration of iron away from the iron substrate in effect constitutes a concentration gradient of iron throughout the product. This suggested that the product formation process may involve the diffusion of iron across the concentration gradient through the surface product where it acts as a catalyst at the surface for further reaction with the vapor.

Forster [79, 80] investigated the interaction of TBPP vapor with both metallic and ceramic materials under dynamic conditions using a ball-on-rod test apparatus within a temperature range of 370° to 400° C. In this work the distribution of the chemical constituents in the film formed on T15 tool steel was elucidated via surface sputtering combined with AES. This concentration-depth profiling revealed a surface product consisting principally of carbon and iron with much lower amounts of phosphorous and oxygen. The carbon and iron concentrations were arranged spatially as opposing gradients in the shape of asymmetric logistic or Gompertz curves [81] with the exterior of the surface product possessing high carbon and low iron concentrations. The forms of the concentration gradients were that which would result from an inter-diffusion process taking place between two different semi-infinite masses sharing a common interface. Under the assumptions made in the application of a Boltzman-Matano analysis of these concentration profiles, Forster determined that the diffusivity of the iron was on the order of 10^{-14} cm²/sec which is several orders of magnitude greater than iron's self diffusivity at the same temperature. Several suggested potential causes for this high rate of iron diffusion were the generation of gradients in stress, electrical charge, and temperature

during the dynamic process of wear with the stress gradients likely being the predominant driving force. Although the absolute changes in the position of each concentration gradient could not be explicitly determined, comparisons of the concentration profiles of surface products formed during widely varying exposure times indicated that the rate of surface material loss due to mechanical wear was identical to the rate of travel of the Matano interface during diffusion. This diffusion was postulated to be the migration of iron cations through an ionic lattice of mixed polyphosphate and phosphide.

Yin et al. have shown that films formed from a certain type of liquid phase zinc O,O-dialkyl dithio phosphate on steel under dynamic conditions at 100° C have resulted in similar iron concentration profiles [82]. After a 30 minute exposure to the phosphate, the iron concentration profile had a slight sigmoidal shape but became nearly linear after 12 hours of exposure time. This is the type of change in concentration profile that would be expected when a diffusive process approaches and eventually reaches a steady state.

In work with iron existing in a variety of oxidation states, Saba and Forster [73] found that the rate of reaction between TCP and a variety of iron oxides tended to vary with the oxidation state of the iron. Thus the ferric iron was shown to be the most active while neutral iron was the least. This is the trend that would be expected for a reacting system in which the controlling step involved the diffusion of iron since the ferric ion is smaller in size than the neutral iron atom.

Summary

In summary, past work has shown that phosphate esters form an adherent product on many metallic surfaces but not on ceramic surfaces. The initial steps in reacting with a

clean iron surface appear to be the adsorption via surface interaction with the oxygen atoms of the phosphoryl and ester linkages. This leads to chemical reactions with the iron and the formation of a phosphate product including some form of polymerized phosphate. Polymer formation seems to be influenced by mechanical action and the presence of oxygen. Surface oxygen and carbon appear to play an important role in determining the reaction path taken by the phosphate ester. The formation of a surface product may involve the movement of one or more of the product or substrate constituents whose mobility may depend on other factors including oxidation state. Moreover, the form of the reaction kinetic rate laws suggest that the diffusive movement of reactants may be involved in controlling the rate of the overall product formation process. However, it is not clear which if any of these product constituents move and if so, to what extent they move and which if any of these constituents may be rate controlling.

This work is an attempt to provide a more explicit characterization of any movement of elements during the overall process of reaction between iron and vaporized TBPP after an initial reaction product has formed. This is accomplished by measuring the rate of the reaction between vaporized TBPP at different temperatures with various substrate materials using a specially modified thermogravimetric analyzer. This analyzer provides a nearly continuous report of product weight as a function of time while maintaining a constant temperature. One of the substrates used in this work was a specially constructed laminated material consisting of a platinum foil on to which a thin layer of iron was deposited. The interface between the layer of iron and the platinum substrate was used as a reference datum against which the movement of any mobile elements could be referenced. Scanning Electron Microscopy (SEM) combined with energy dispersive

spectroscopy (EDS), and Fourier-transform infrared spectroscopy (FTIR) were used to characterize the reaction products beneath the surface. The movement of elements and their concentrations throughout the bulk of the product were determined by multiple cycles of surface sputtering followed by an AES examination of the surface created by the sputtering process.

CHAPTER II

EXPERIMENTAL

TBPP

Commercially available TBPP is composed of a mixture of the various mono-tertiary-butyl, di-tertiary-butyl, and tri-tertiary-butyl substitutionary derivatives of triphenyl phosphate. The structure of the asymmetric di-*p*-tertiary-butyl form is shown in Figure 4. The conventional commercial production of triaryl phosphates utilizes temperatures on the order of 200° C and a metallic chloride catalyst [27, 83]. The precursors utilized in this synthesis are phosphorous oxychloride, phenol, and various alkane substituted phenols. The use of phenols and varying derivatives of phenols in this synthesis results in a product consisting of molecules with varying structures such as the asymmetric structure of the di-substituted form shown in the figure. The incorporation of asymmetric molecules in the mixture serves to hinder the formation of solid crystalline phases at lower temperatures. The bulk physical properties of the mixture depend on the type and proportion of each symmetric and asymmetric molecule contained within the mixture. The particular mixture of *t*-butyl phenyl phosphate esters used in this work was a commercial product distributed under the label, "DURAD® 620B." The term "DURAD" is the registered trade name of the FMC Corporation's product line of triaryl phosphate

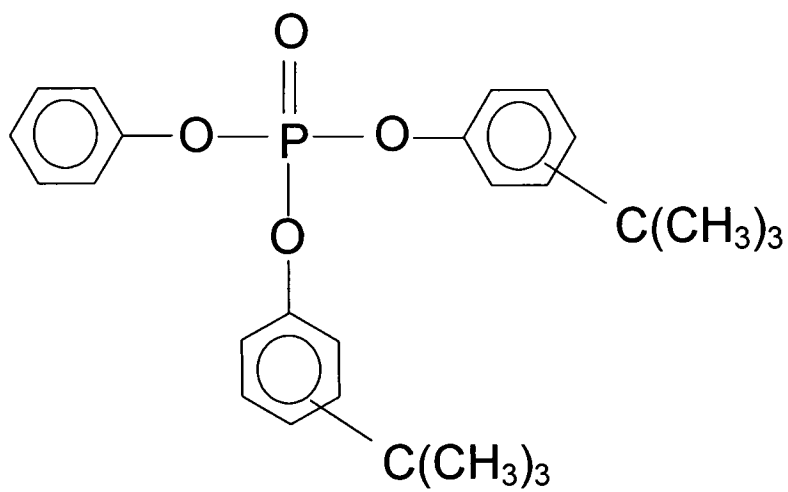


Figure 4. Molecular structure of di(*t*-butyl phenyl) phenyl phosphate

ester lubricant additives. The DURAD[®] 620B material was used as received from the FMC Corporation. The density of the liquid TBPP was measured and this value was in turn used in the calculation of the syringe pump flow rate. Three measurements of density were made at 22° C using three different glass pycnometer flasks each possessing a 2 cm³ volume. The mean of the three density measurements was calculated to be 1.107g/cm³ with a standard deviation of 0.003g/cm³. This is comparable to the 1.120 ± 0.002 g/cm³ value reported by Wright [84] for the density of this same material at 20° C. For reference purposes, the FTIR transmission spectra of the liquid DURAD 620B was generated using a KBr window in a Perkin Elmer System 2000 FT-IR Spectrometer. A FTIR diffuse reflectance spectra of the liquid DURAD 620B was also generated on the surfaces of gold, aluminum, and iron using a Perkin Elmer *i*-Series FT-IR Microscope. The IR spectra of the sample on the iron surface is shown in Figure 5. A gas chromatography/mass spectroscopy analysis of this same material was reported earlier by Wright [85]. The analysis by Wright identified the following three principal constituents: diphenyl-*t*-butyl phenyl phosphate, phenyl-di-*t*-butyl phenyl phosphate, and tri-*t*-butyl phenyl phosphate.

Carrier Gases

Helium and nitrogen were used as the carrier gases in this work. The source of nitrogen was the vent gas from the laboratory's liquid nitrogen storage Dewar. This gas was dried by passing through a Drierite desiccating trap followed by an indicating oxygen trap (P.N. 4004) from Alltech Associates, Inc. The helium was supplied by a standard

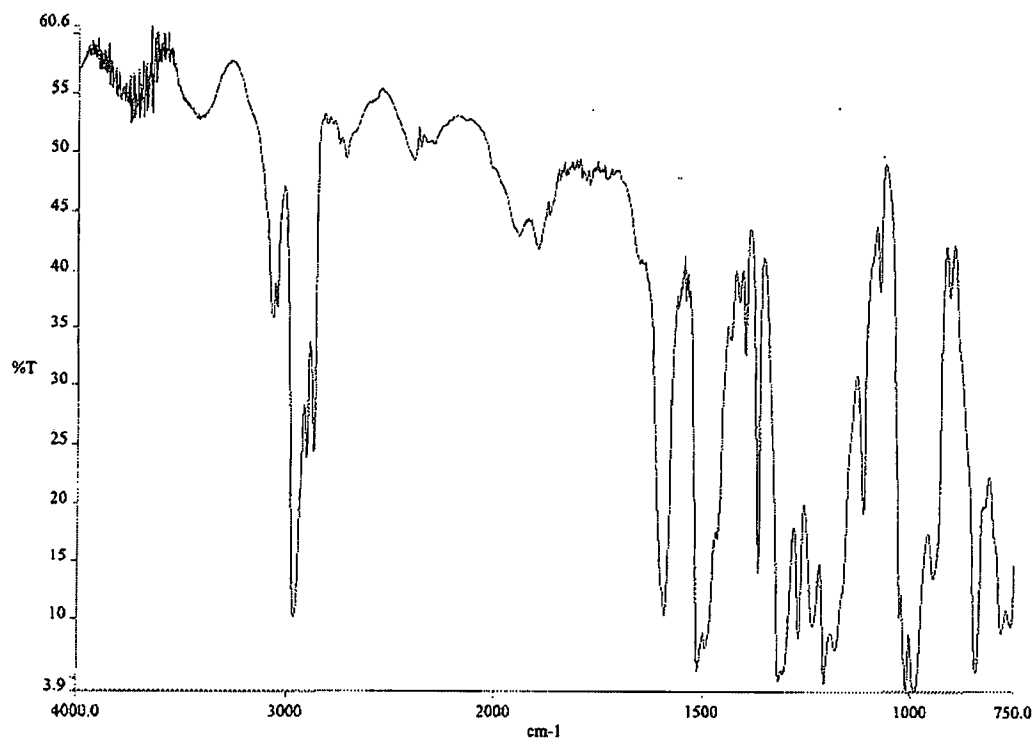


Figure 5. FTIR diffuse reflectance spectra of TBPP on iron.

compressed gas cylinder (Weiler Welding Co.) and was of high purity grade. This gas was also dried with a Drierite desiccating trap followed by the same type of oxygen trap used with the nitrogen gas.

Iron Foil

This material consisted of thin (0.1mm nominal thickness) sheets of iron with a purity of 99.99 percent (metals basis) as supplied by Alfa[®] Aesar[®]. The foil was cleaned in acetone, dried, and stored in an atmosphere of dry nitrogen prior to use. Figure 6 shows an SEM image of the surface of a typical sample of this foil. Figure 7 shows the spectra resulting from an EDS (Energy-Dispersive Spectroscopy) examination of this foil's surface. The sensitivity of the spectrometer is approximately 0.5 atomic percent with a depth of penetration of about 1 μ m. Even though all peaks in the spectrum are associated with iron, it can be reasonably assumed that oxygen and adventitious carbon are also present on the exterior surface of each sample. The low concentrations of this oxygen and carbon combined with the small depth to which these elements extend into the surface would result in concentrations that are well below the sensitivity of the spectrometer. The apparent surface area of each sample of this material was calculated by dividing the weight of the sample by a surface density factor. This factor is defined as

$$\frac{\rho_{Fe}\theta_{Fe}}{2}$$

where ρ_{Fe} is the density of pure iron and θ_{Fe} is the thickness of the foil. For the sample sizes used, the contribution to the total apparent surface area of each sample by the top and bottom surfaces is on the order of 400 times that which would be contributed by the

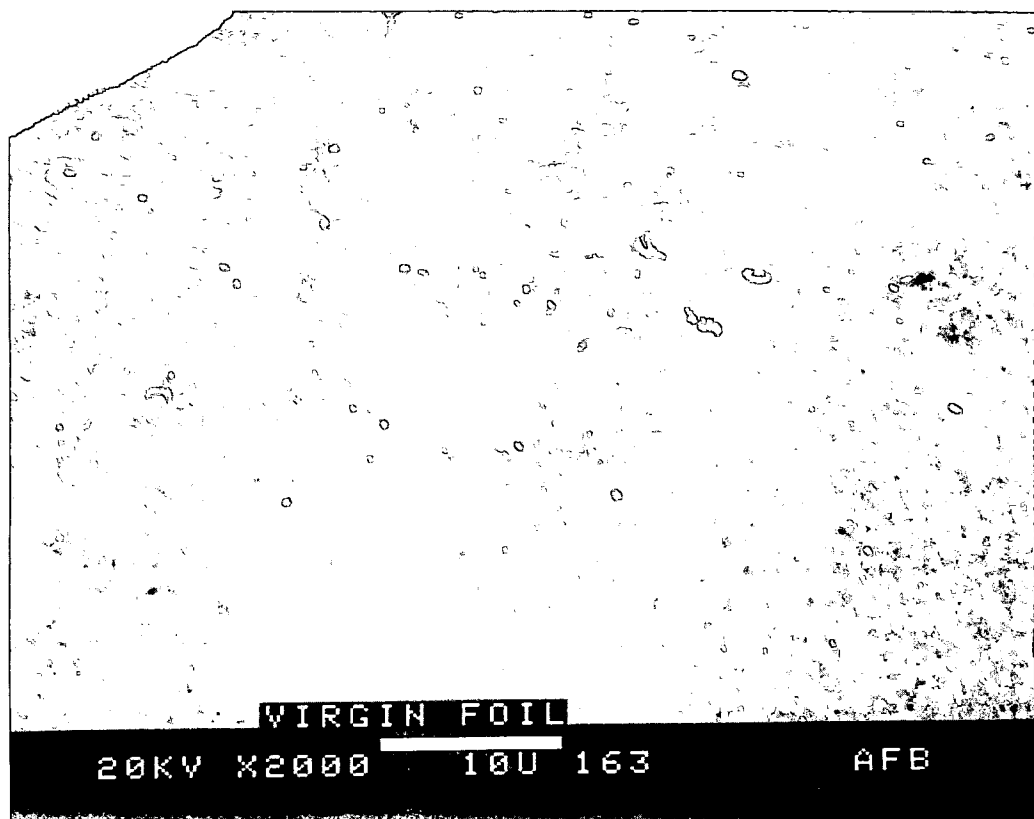


Figure 6. SEM image of iron foil surface.

Spectrum: Spectrum1

Range: 20 keV

Total Counts=829925. Linear Auto-VS=1042

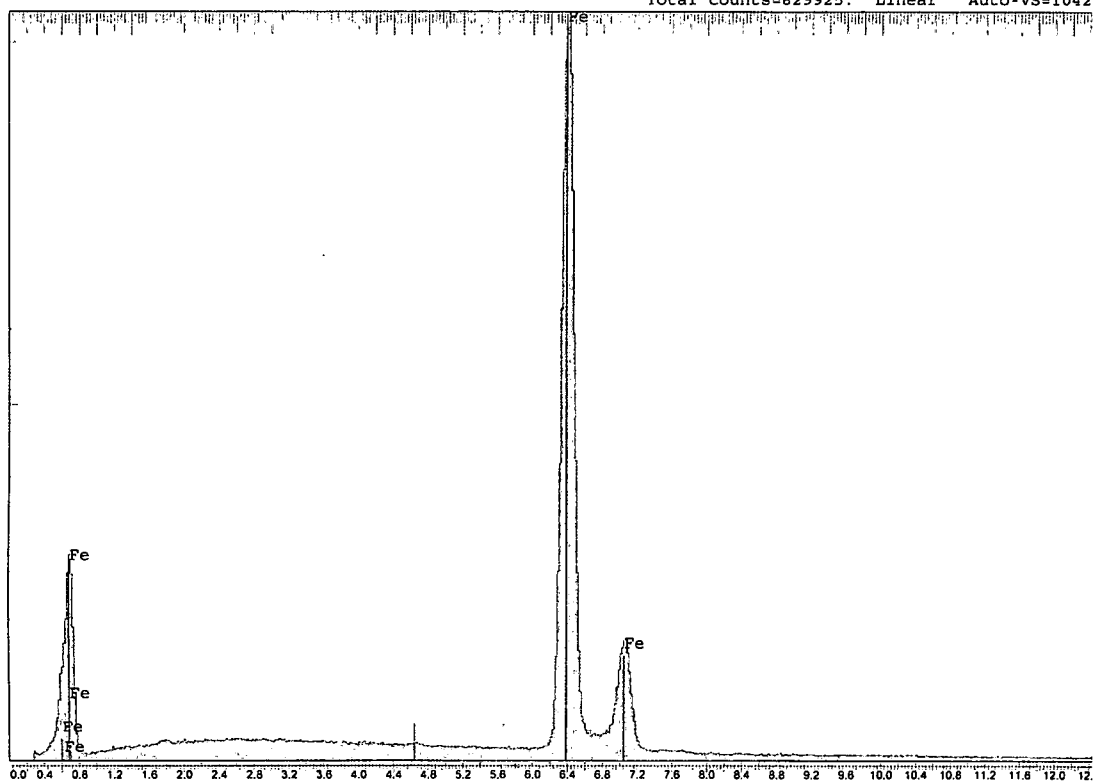


Figure 7. EDS of iron foil surface.

edges of the foil samples. For this reason, this edge contribution to the total area is considered inconsequential and is not taken into account by this factor. Using the manufacturer's stated value for the foil thickness, i.e. 100 μm , the surface density factor for the iron foil is calculated to be 39.35 mg/cm^2 .

1010 Steel Foil

This material consisted of AISI 1010 steel in sheet form as supplied by Precision Brand Products Inc. The nominal thickness of this steel sheet was listed by the manufacturer as 0.004 inches. The density was assumed to be the same as pure iron with the same surface density factor as the iron foil.

Iron/Platinum Laminated Foil

This material consisted of a thin, 250 μm nominal thickness, platinum sheet (supplied by Engelhard Industries) on which one side was coated with a 1,000 \AA thick layer of iron by sputter vapor deposition at room temperature. This laminated foil was stored in an atmosphere of dry nitrogen prior to use. The apparent surface area of each sample of this foil was calculated using a surface density factor similar to that used for the iron foil described above. In this case the factor is defined as:

$$\frac{W_{\text{PtFe}} \rho_{\text{Pt}} \theta_{\text{Pt}}}{W_{\text{Pt}}}$$

where W_{Pt} is the weight of the platinum foil prior to being coated by iron, W_{PtFe} is the weight of the coated platinum foil, ρ_{Pt} is the density of pure platinum, and θ_{Pt} is the thickness of the platinum foil prior to coating. As with the iron foil, the contributions of

the foil edges to the total apparent surface area is considered inconsequential and is not taken into account by this factor. For the laminated foil this surface density factor was calculated to be 53.68 mg/cm^2 .

Figure 8 displays the distribution of elements within the iron layer as determined by AES depth profiling. As can be seen in the diagram, the foil consists of a platinum substrate onto which has been deposited a layer of iron. The oxygen present within the iron appears to have come from small amounts of diatomic oxygen and/or moisture that were present in the deposition chamber and subsequently incorporated into the iron layer during the coating process.

Silicon Nitride

The powdered form of this material was supplied by H. C. Starck GmbH & Co. This powder consisted of particles with diameters less than $100 \text{ }\mu\text{m}$. The bulk solid form of this material was in the form of a 3.17 mm diameter sphere with an apparent surface area calculated to be 0.32 cm^2 . These materials were used as received.

Iron (III) Phosphate

This material was supplied by the Alfa[®] Aesar[®] Company and consisted of a hydrated powder of the phosphate with particle sizes on the order of $1 \text{ }\mu\text{m}$. This material was used as received.

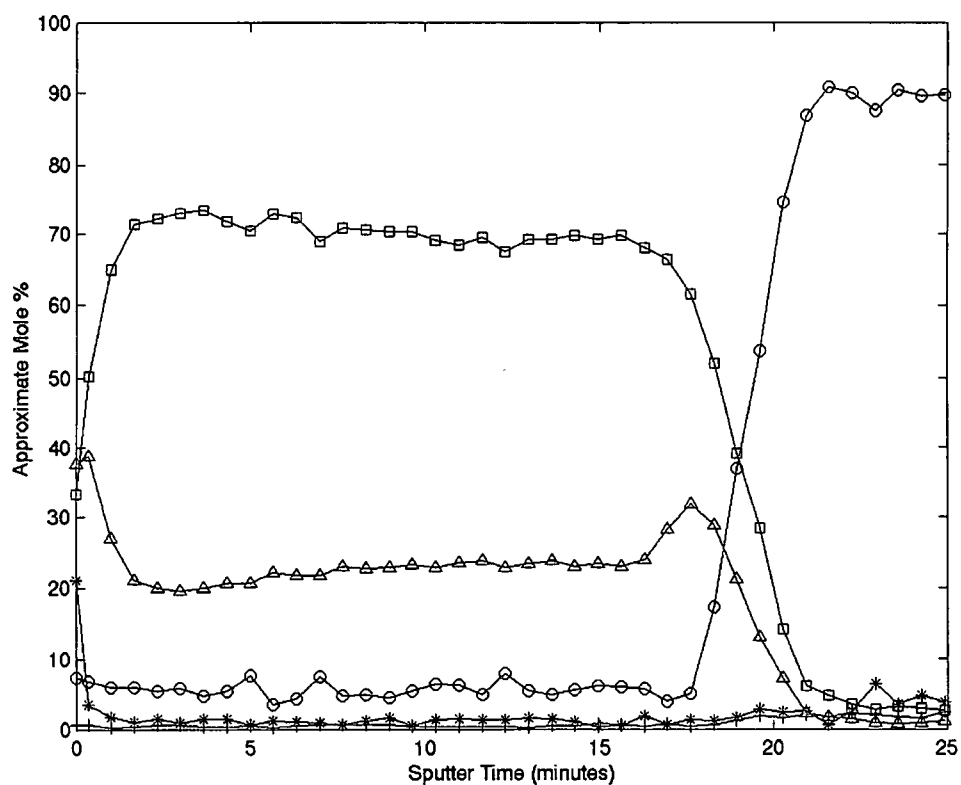


Figure 8. Concentration-depth profile of iron/platinum laminated foil; ○-platinum, □-iron, △-oxygen, *-carbon.

Experimental Equipment and Procedures

All reactions were carried out in a TGA-2050 thermogravimetric analyzer (TGA) manufactured by TA Instruments and modified by the author. This modified analyzer provides a nearly continuous recording of a sample's weight within a controlled atmosphere. This facilitates the determination of how the product weight changes with reaction time permitting an accurate determination of specific rate law constants. However, this equipment does not provide useful information on this weight change function before reaching steady state operating conditions.

The furnace assembly of the TGA-2050 was modified to accept a continuous flow of TBPP laden carrier gas. This particular TGA model utilizes a moveable furnace which when elevated completely envelopes the sample to ensure even heating and to isolate the sample from the surrounding environment. The stainless steel fitting on the TGA furnace purge gas exhaust port was used as the point of attachment for the vapor generating assembly. The weight of this assembly was supported by a bracket which was clamped to the exterior wall of the furnace. This arrangement allowed the heated assembly of the vapor generator to move along with the furnace. This modification is shown diagrammatically in Figure 9. The furnace assembly consists of a quartz tube surrounded by heating elements and a water cooled jacket. The power to the heating elements is controlled through feedback from a thermocouple positioned close to the sample pan.

The flow of pressure regulated carrier gas was split into two separate flow paths. One portion of the flow was directed to the balance chamber of the TGA as a purge gas to maintain a contamination free environment around the balance components. The remainder of the flow was used to vaporize and carry the TBPP to the furnace.

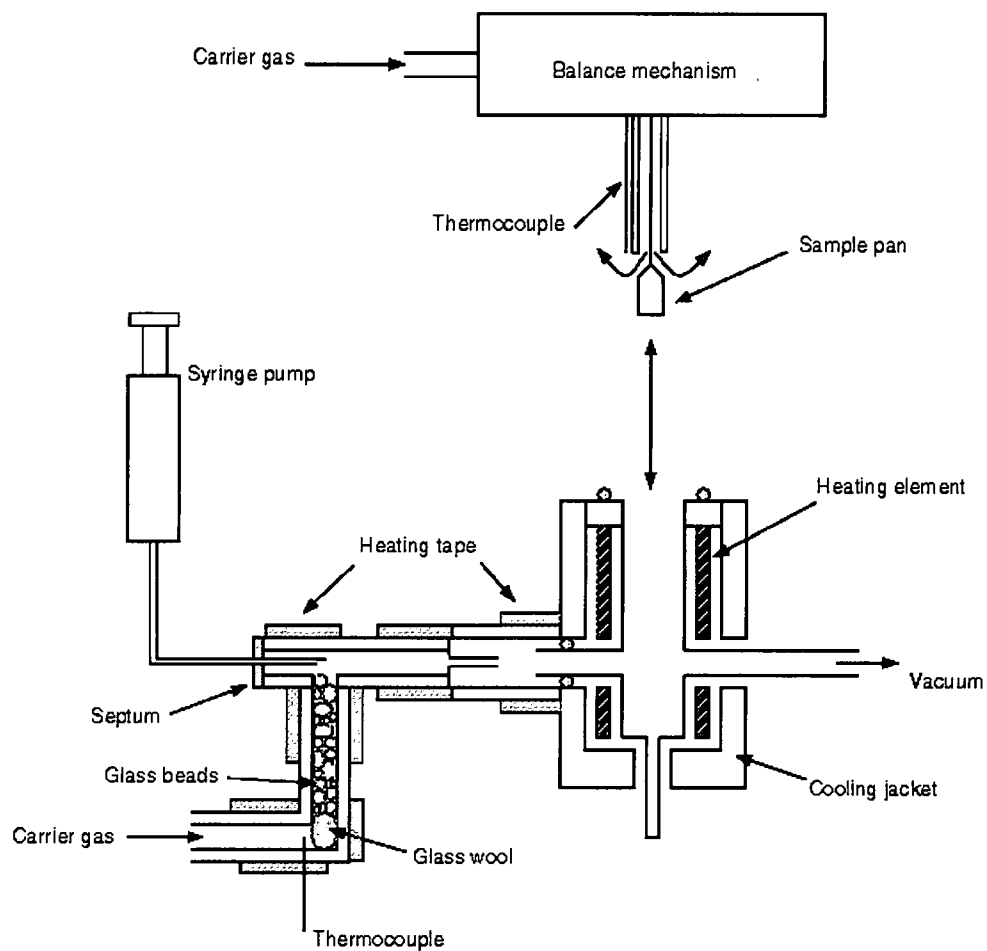


Figure 9. Diagram of the modified TGA and vapor generator assembly.

Each separate flow was controlled by a rotameter supplied and calibrated by the TA Instruments Corporation for each of the gases used. The ratio of the furnace flow to the balance chamber flow was maintained at 9:1 as recommended by the manufacturer. The upper limit to the flow rate of carrier gas through the assembly was a function of the sensitivity of the balance hardware. It was found by trial and error that flow rates above 115 cm³/min generated significant irregular aerodynamic forces on this hardware which were then interpreted by the balance mechanism as changes in sample weight. Above 115 cm³/min, these anomalous variations in perceived sample weight were on the order of several micrograms. A flow rate of 108 cm³/min was selected for use in this work since this value was less than the 115 cm³/min limit described above and happened to be demarcated at a convenient-to-read location on the rotameter.

The gas flow within the vapor generator tubing was characterized on the basis of the flow Reynolds number (N_{Re}) defined as [86]:

$$\frac{d u \rho}{\mu}$$

where d is the diameter of the tubing, u is the superficial velocity of the gas, ρ is the gas density, and μ is the absolute viscosity of the gas. The contribution of the TBPP vapor to the viscosities and densities of the combined gas was deemed inconsequential due to the concentration of the TBPP being very low. Values for gas viscosities were taken from standard handbook nomographs [87]. Gas densities were calculated under the assumed validity of the ideal gas law at atmospheric pressure. Table 1 displays these parameter values and the resulting calculated N_{Re} values at the 115 cm³/min flow rate and at the

Table 1. Fluid flow data and calculated Reynolds numbers (N_{Re}) for helium and nitrogen gases within the TBPP vapor generator.

Gas	Property	Temperature (°C)	
		270	600
He	ρ (g/cm ³)	9.0×10^{-5}	5.6×10^{-5}
	μ (Poise)	2.9×10^{-4}	4.0×10^{-4}
	N_{Re}	2	1
N ₂	ρ (g/cm ³)	6.3×10^{-4}	3.9×10^{-4}
	μ (Poise)	2.7×10^{-4}	3.6×10^{-4}
	N_{Re}	12	6

highest and lowest temperatures used in this work. As can be seen in the table the flow at both temperature extremes falls well within the laminar flow regime, i.e., $N_{Re} < 2,000$.

With the flow being characterized as laminar, an estimation can easily be made of the propensity for TBPP vapor to be transported against the flow by gas phase diffusion which would result in the contamination of the up-stream hardware. At the flow rate used in this work, the possibility of contamination due to up-stream gas phase diffusion can be discounted. This is demonstrated by the following.

The relationship between superficial velocity, upstream distance and TBPP vapor concentration at the upstream distance was estimated by comparing the mass flux due to convection in the direction of the flow to the mass flux due to diffusion in the opposite direction as follows:

$$Cu > D \frac{dC}{dx}$$

where C is the concentration expressed as mass per unit volume, D is the diffusivity of the TBPP vapor in the carrier gas, and u is the superficial velocity of the carrier gas. This assumes a diffusivity that is independent of concentration which is considered reasonable under the experimental conditions used. This inequality expresses the requirement that the flux due to down-stream convection must be greater than the flux due to up-stream diffusion. The solution to this relation is:

$$u > D \frac{\Delta \ln C}{\Delta x}$$

where $\Delta \ln C$ is the change in the logarithm of the concentration that spans the distance Δx . This relation expresses the superficial velocity that must be maintained to ensure that an up-stream flux of TBPP vapor does not occur. Wang et al. [88] have reported a pre-

exponential factor and activation energy for the diffusion of TCP vapor in nitrogen gas to be 1.2 cm²/sec and 2,560 cal/mole respectively without reference to temperature range limitations. Using these values, the diffusivity of TCP vapor in nitrogen at a temperature of 270° C is calculated to be 0.11 cm²/sec. Since the molecular size and weight of TCP and TBPP are comparable, this value of diffusivity should be adequate for the estimation of the diffusivity of TBPP in nitrogen. This value can then be used with the Fuller, Schettler, and Giddings relation to estimate the diffusivity of TBPP in helium under the same conditions. Here,

$$D_{TBPP,N} = \frac{(10^{-3}) T^{1.75} \left[\frac{M_{TBPP} + M_N}{M_{TBPP} M_N} \right]^{\frac{1}{2}}}{P \left[(\Sigma V_{TBPP})^{\frac{1}{3}} + (\Sigma V_N)^{\frac{1}{3}} \right]^2}$$

where T represents temperature, P represents pressure, M represents molecular weight, and ΣV represents values for the atomic diffusion volumes which are functions of the molecular structure. Since in this case, $D_{TBPP,N}$ is known, $(\Sigma V_{TBPP})^{1/3}$ can be defined in terms of $D_{TBPP,N}$ and the other constants. This value can then be used in the application of this same expression for the diffusivity of TBPP in helium, $D_{TBPP,He}$ which results in:

$$D_{TBPP,He} = D_{TBPP,N} \left[\frac{\left(\frac{M_{TBPP}}{M_{He}} \right) + 1}{\left(\frac{M_{TBPP}}{M_N} \right) + 1} \right]^{\frac{1}{2}}$$

The numerical value of 438 g/mole has been used in the past as a representative number for M_{TBPP} [14]. Using this value, $D_{TBPP,He}$ is estimated to be 0.28 cm²/sec. With the use of these values, and for a 10,000 fold decrease in concentration across a distance of 1 cm, the superficial velocity must be greater than 2.6 cm/sec. The flow rate of 108 cm³/min provides a superficial flow velocity that is more than four times the 2.6 cm/sec. Since the diffusion in helium is faster than the diffusion in nitrogen, the value for the superficial velocity required for nitrogen would be even smaller. Thus at this flow rate, contamination by the diffusion of TBPP in the opposite direction of the flow can be discounted.

The TBPP vapor generating assembly (see Figure 9) was fashioned after similar devices used successfully in past VPL related work. This assembly was constructed from type 304 stainless steel tubing and stainless steel compression fittings. As shown in the figure, heat was supplied by two separate heating tapes wrapped around the assembly. The exterior surface of each heating tape/tube assembly was insulated with fiberglass. The up-stream heating tape was one meter in length and was manufactured by Electrothermal Eng Ltd. The power to this tape was controlled by a stepless input control unit (model CN-A8005M) manufactured by the Thermolyne Corporation. The down-stream heating tape was one half meter in length and was also manufactured by Electrothermal Eng Ltd. This tape was controlled by an AC variable transformer manufactured by the General Radio Company. The control unit for the up-stream tape was continuously readjusted so that a constant temperature of 225° C was maintained at the thermocouple. Prior to each experiment and before the syringe pump needle was inserted through the septum, the appropriate voltage for the down-stream tape was

determined by trial and error. A small Becton-Dickson syringe needle was inserted through the septum and a sub-miniature, type J thermocouple (Omega Engineering Inc.) was threaded through the shaft of this needle such that the end of the thermocouple was positioned above the tee section of the vapor generator assembly. The voltage across the down-stream heating tape was then adjusted to maintain the desired temperature as measured by this thermocouple. Once the voltage which maintained a temperature of 270° C was determined and the temperatures at both thermocouples were constant, the syringe/thermocouple was withdrawn from the septum. This voltage was then maintained throughout the experiment by manually readjusting the variable transformer as necessary.

Previous work by Forster and Trivedi [70] showed that a TBPP vapor concentration of around 0.09 mole percent provided good lubrication to rolling contacts and for this reason 0.09 mole percent was selected as the target concentration of TBPP vapor used in this work. The temperature of 270° C was selected for the evaporation of the liquid TBPP based on a number of related factors. This temperature of 270° C is approximately 150° C less than the boiling point of many formulations of TBPP [88] and has been shown by Wright [89] to be high enough to evaporate the TBPP used in this work at a reasonable rate while being low enough to prevent significant thermal decomposition while in the gas phase. At 270° C the vapor pressure of TBPP was shown by Wright [85] to be approximately 15 mm Hg. The concentration associated with this pressure is more than an order of magnitude higher than the 0.09 mole percent used in this work. This temperature is also at least 30° C lower than the temperature of the furnace in all experiments. Thus, using a 270° C vaporization temperature ensures that no vapor will

condense into an aerosol form while in the carrier gas nor will it condense on the surface of the test samples used in each experiment.

An initial set of thermogravimetric analyses were performed on the TBPP using several different carrier gases to provide some guidance in designing the vapor generator assembly for the generation of the 0.09 mole percent concentration. This was accomplished using the unmodified TGA in which the TBPP was held in open gold sample pans. Figure 10 displays the results of these analyses. Here the vaporization is reported in units of milligrams per square centimeter of vaporization surface area per hour. Although the particular mixture of aryl phosphate esters used in this work is not known to be azeotropic, any concentration gradients generated between the bulk liquid and the surface of the liquid at the point of evaporation will be low when considering the low diffusivity of the components of the TBPP in the liquid phase. This provides a sufficient basis for the working assumption that the concentrations of components in the vapor phase do not change with time due to the process of evaporation. With a carrier gas flow rate of $108 \text{ cm}^3/\text{min}$, the syringe pump is required to provide a flow of liquid TBPP to the vapor generation assembly of about $0.1 \text{ cm}^3/\text{hr}$. This also requires that the liquid have a surface area of 0.4 cm^2 for vaporization at the rate desired in the TGA using nitrogen as a carrier gas.

In order to ensure that a sufficient surface area was available for evaporation at the desired flow rate and to provide a higher surface area in the event of a need to use higher vapor concentrations, the vapor generator was constructed with a packed bed consisting of small glass beads positioned just up-stream of the point at which the TBPP is expelled from the tip of the syringe needle. The syringe needle was made of stainless steel and

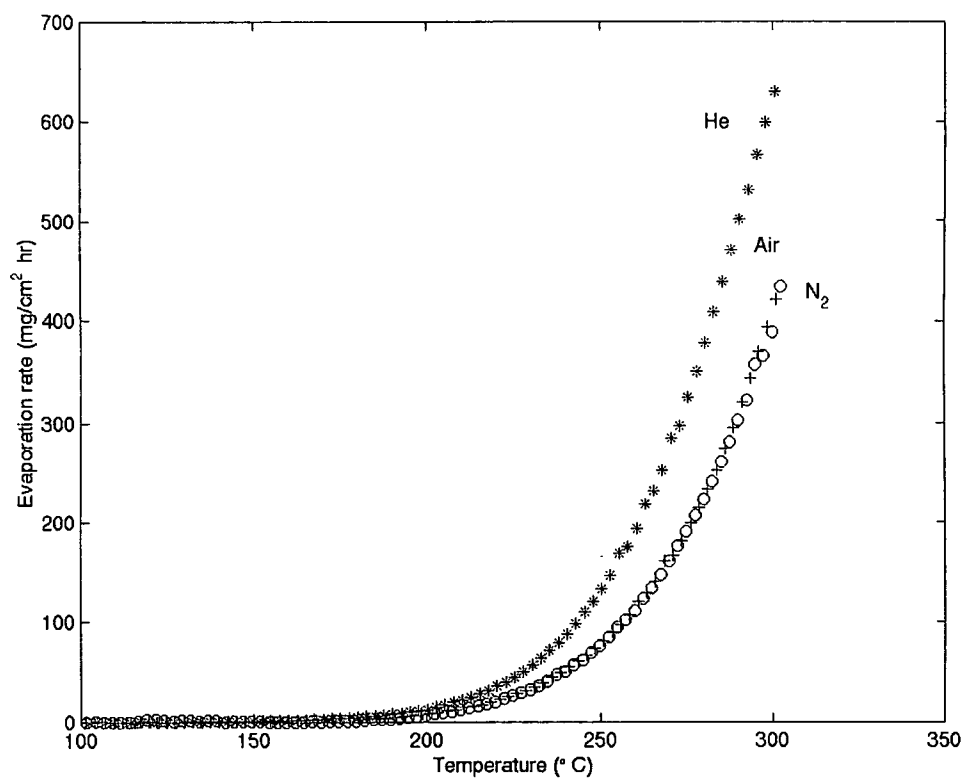


Figure 10. Evaporation rate of TBPP in several gases.

was attached to a 2-cm³ Becton-Dickson syringe. The flow of the liquid TBPP from the syringe was controlled by a Sage Instruments syringe pump, model 355. The pump controls were set to a "flow" setting of 20 percent and a "range" setting of 1/1000 which configured the pump to deliver liquid TBPP at a rate of 0.1 cm³/hour. The settings for this flow rate and the consistency of the flow were verified by measuring the actual pump output. This involved calculating the mean and variance of a series of samples taken from the pump over a two hour time period. Sampling was done by accurately measuring the weight of each drop of liquid TBPP emerging from the syringe needle along with the incremental periods of time between each drop. This resulted in a total of 17 measurements all of which were performed with a Mettler AT261 balance. Prior to these measurements, the pump motor was operated for a one hour warm-up period and the syringe was filled such that the syringe plunger was positioned at the 1.5 cm³ mark on the syringe barrel.

The mean flow rate based on these flow measurements was found to be 2.01 mg/min with a standard deviation of 0.09 mg/min. A plot of the volume of TBPP liquid output expressed in cm³ as a function of time is shown in Figure 11. This data was fit with a linear function by a least-squares procedure. The resulting line extending from the origin through the data points has a correlation coefficient (r^2) value greater than 0.9999. The consistency of the flow over the 2 hour time period was also determined by dividing each measurement of droplet weight by the amount of time taken for the droplet to emerge from the syringe needle resulting in 17 separate values of flow rate as a function of time. This data was then modeled with a linear function by a least-squares fit procedure. Here the independent variable represents the individual flow rates and the dependent variable

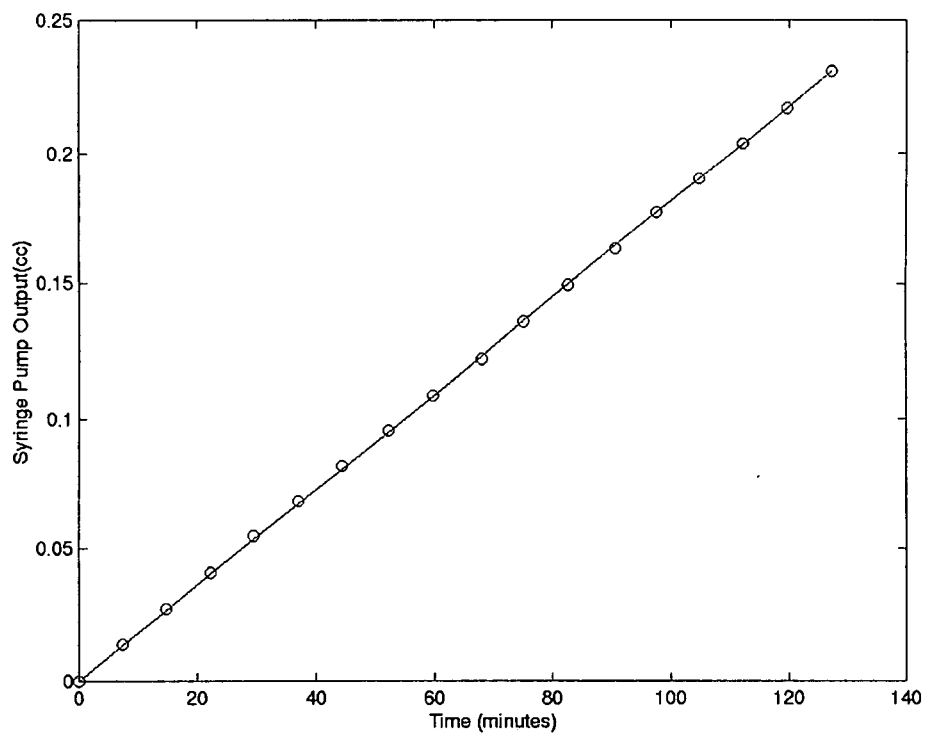


Figure 11. Syringe pump output.

represents time. This data was then tested using the null hypothesis that the intercept of the line resulting from this least squares fit is zero as opposed to being something other than zero. The results show that at the 99.9 percent confidence level, the null hypothesis for the intercept could not be rejected. Thus the slight variations in flow rate that take place as the pump operates are considered to be random and not a function of time or of the position of the plunger in the syringe barrel.

The needle through which the liquid TBPP was fed to the vapor generator was inserted through a high- temperature/low-bleed septum manufactured by Hewlett Packard. This septum maintained a leak-free seal between the needle and the stainless steel fitting. An initial set of experiments was performed to determine the potential for any spurious weight changes during start-up at the selected flow rate when neither vapor nor sample was present.

It was found that during the initial temperature ramp-up, the energizing of the furnace heating elements led to an anomalous weight variation. The extent of this variation was proportional to the temperature ramp-up rate, i.e., a higher ramp-up rate resulted in a larger weight variation. Figure 12 displays an example of this anomaly. As can be seen from the figure, as the power drawn by the heating elements decreased and the heating rate declined, this weight change anomaly dissipated. This type of anomalous weight change did not occur when the power levels of the furnace elements cycled through slight changes during steady state operation but rather only occurred during the initial heating to steady state temperature.

Two different carrier gases were used in these experiments. Nitrogen was used in part of this work to provide data that could be compared to the data from earlier work by other

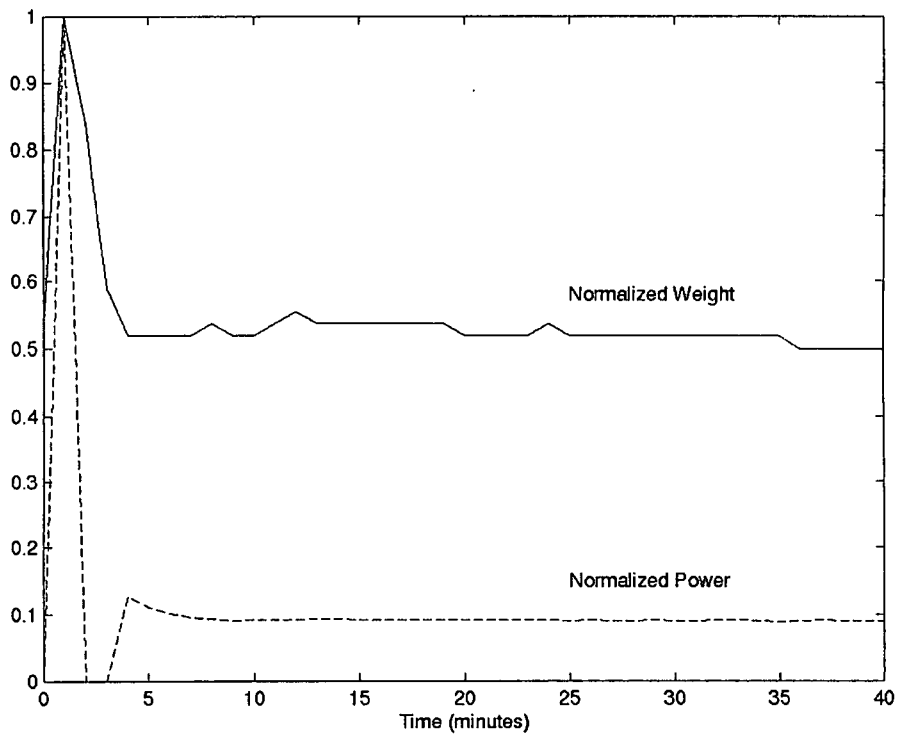


Figure 12. TGA weight change anomaly at start-up.

authors investigating the interaction of TCP and TBPP with various ferrous surfaces. Helium was selected as a carrier gas after it was discovered that the nitrogen, unlike helium, appears to have a direct effect on the interaction of the TBPP with the iron. As a consequence of this interaction with nitrogen, the highest possible temperature ramp-up rate of 200° C/min was used to minimize the time that the iron was exposed to the nitrogen at high temperatures. This rate of 200° C/min is also the maximum rate accommodated by the TGA. Figure 13 shows how the actual furnace temperature changed as a function of time with the use of this ramp-up rate using nitrogen as a carrier gas. As can be seen in the figure, the furnace temperature increases in the form of a damped oscillator. It was found by trial-and-error that by inserting the syringe needle at a point in time approximately three minutes after start-up this temperature oscillation could be further dampened. By inserting the needle at the 3.3 minute point in time, the time taken to reach a steady state temperature with less than a 1° C variation was reduced by several minutes. For this reason a needle insertion time of 3.3 minutes was used in all experiments.

The experiments involving the metal foil samples employed a single consistent procedure. The sample foil was first weighed, loaded, and then the movable furnace was elevated to its closed position. The carrier gas flows and temperatures were then allowed to come to steady state after which the thermocouple/needle assembly was removed and the vapor generator assembly was allowed to purge with the carrier gas for one hour. The furnace was then switched on and after 3.3 minutes the syringe pump needle was inserted. The TGA balance mechanism monitored the weight of the sample foil with an accuracy of ± 2 micrograms and was programmed to record the sample weight every 2 seconds.

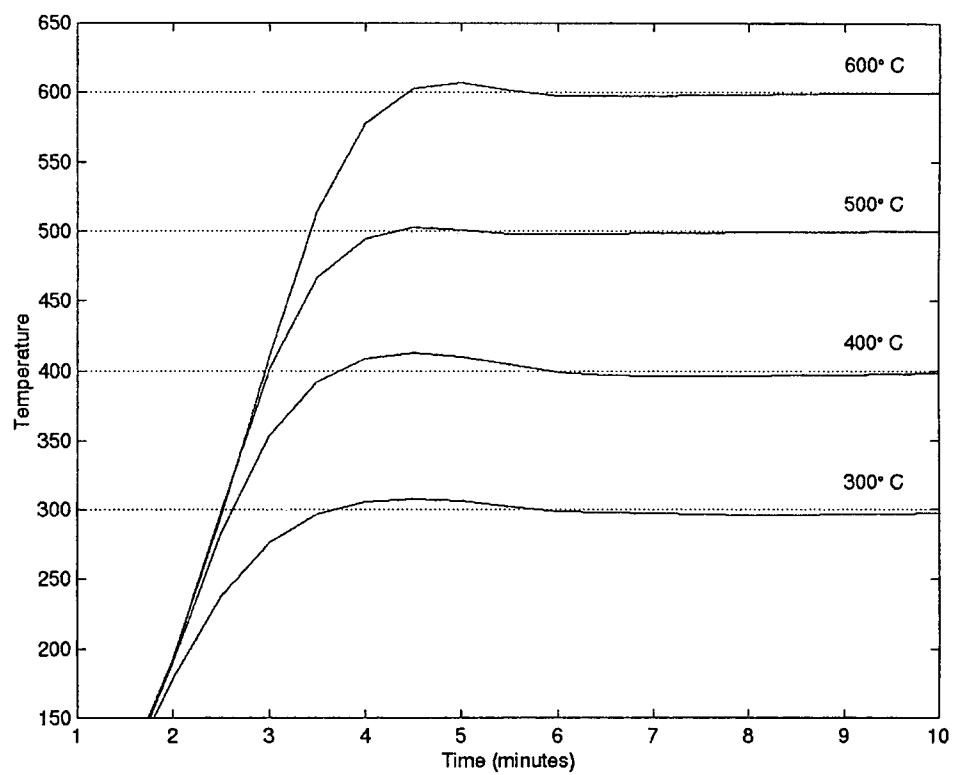


Figure 13. TGA furnace temperature change on start-up.

At the end of two hours, the syringe pump needle was withdrawn and the furnace was switched off. The furnace was allowed to cool until a temperature of 40° C was reached. At this time the furnace was lowered to its open position and the sample was removed. All samples were reweighed and then stored. In the case of the platinum/iron laminated samples, the furnace was lowered immediately after the syringe needle was withdrawn in order to minimize the amount of TBPP that might condense on the surface of the reaction product while cooling. These samples were reweighed and then stored in a desiccator prior to AES analysis. After each sample was removed, the TGA furnace was once again closed and brought to a temperature of 800° C. The system was then purged with dry air while maintaining the 800° C furnace temperature for 12 hours.

CHAPTER III

RESULTS

Carrier Gas Effects

Both helium and nitrogen were used as carrier gases in this work. Helium does not exhibit a solubility in metals to any great extent below the melting point of the metal. Unlike helium, nitrogen and oxygen are both known to dissociate on the surface of many metals and to absorb and chemically react on the surfaces of ferrous metals even at very low temperatures. Although steps were taken to remove potential contaminants from both carrier gases, a trace of oxygen contamination appeared in both. Consequently, a portion of the weight gained by the metal substrates during high temperature exposures to TBPP vapor may be due to the absorption and or reaction with these gases. For this reason, an initial set of experiments was performed to investigate the potential for these types of interactions between the carrier gases and samples of the metals used in this work. Neither carrier gas was found to have any effect on the platinum sample pan or any of the associated balance hardware that extends into the sample chamber of the TGA. This was found to be consistent at all temperatures over a two hour time period.

Similar experiments were conducted using samples of iron and 1010 steel. Samples of steel were used as a low cost alternative to iron for the experiments involved in the initial set up. In contrast to the platinum hardware associated with the balance, both iron and steel were found to gain weight in the presence of both the nitrogen and helium carrier

gases. Figures 14 and 15 display the weight gain of steel and iron foil samples on exposure to the nitrogen carrier gas as a function of temperature and time. These figures also show the anomalous weight changes that occur during the initial 10 minutes of exposure. This includes weight changes due to the start-up process of the equipment (as previously discussed in Chapter II).

After 70 minutes of exposure to the nitrogen carrier gas at 300° C, and upon removal from the furnace, the 1010 steel samples were found to display a yellow-blue tint, at 400° and 500° C a blue-gray color, and at 600° C a solid flat gray color. Similarly, the iron samples displayed a slight green-blue tint at 300° C, a violet-gray color at 400° C and a solid flat gray color at 500° and 600° C.

Figure 16 shows the weight gains by iron as a function of temperature and time due to its exposure to the helium carrier gas. Upon removal of these samples from the furnace after exposure to this carrier gas for 70 minutes the iron samples took on a slight green/blue tint at 300° and 400° C and a slight blue tint at 500° and 600° C. The weight gained on exposure to these carrier gases was calculated by subtracting the initial weight of the sample from the final sample weight and dividing this difference by the apparent surface area of each sample. All of the measurements involving only the metals and carrier gases were made prior to attaching the vapor generating hardware to the TGA.

The weight gain of iron by exposure to the helium carrier gas was observed to cease after the surface of the sample had been sufficiently covered by product formed by reaction with the TBPP vapor. A case in point is the exposure of an iron sample to TBPP vapor in the helium carrier gas at a temperature of 300° C. After an exposure of 30

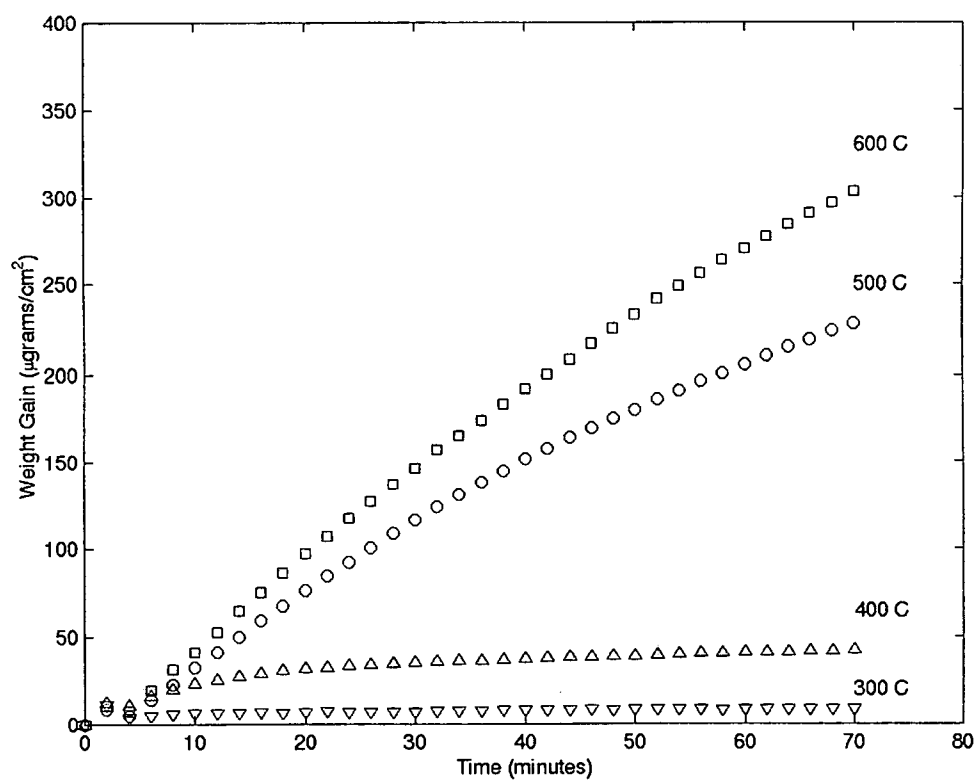


Figure 14. Weight gain by 1010 steel in nitrogen carrier gas.

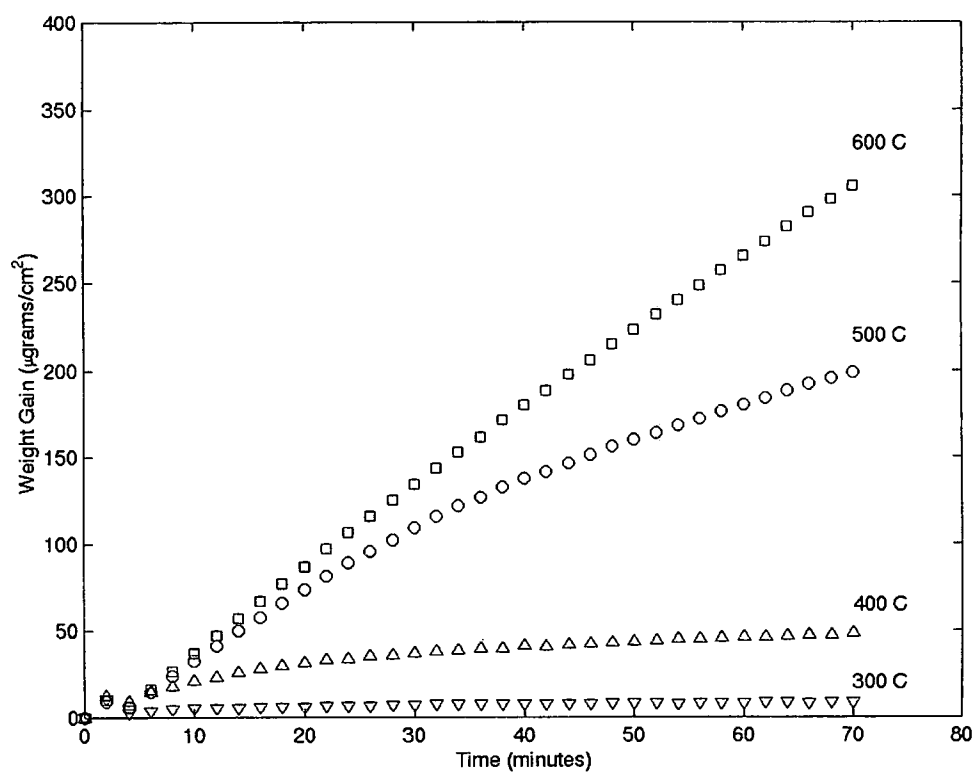


Figure 15. Weight gain by iron in nitrogen carrier gas.

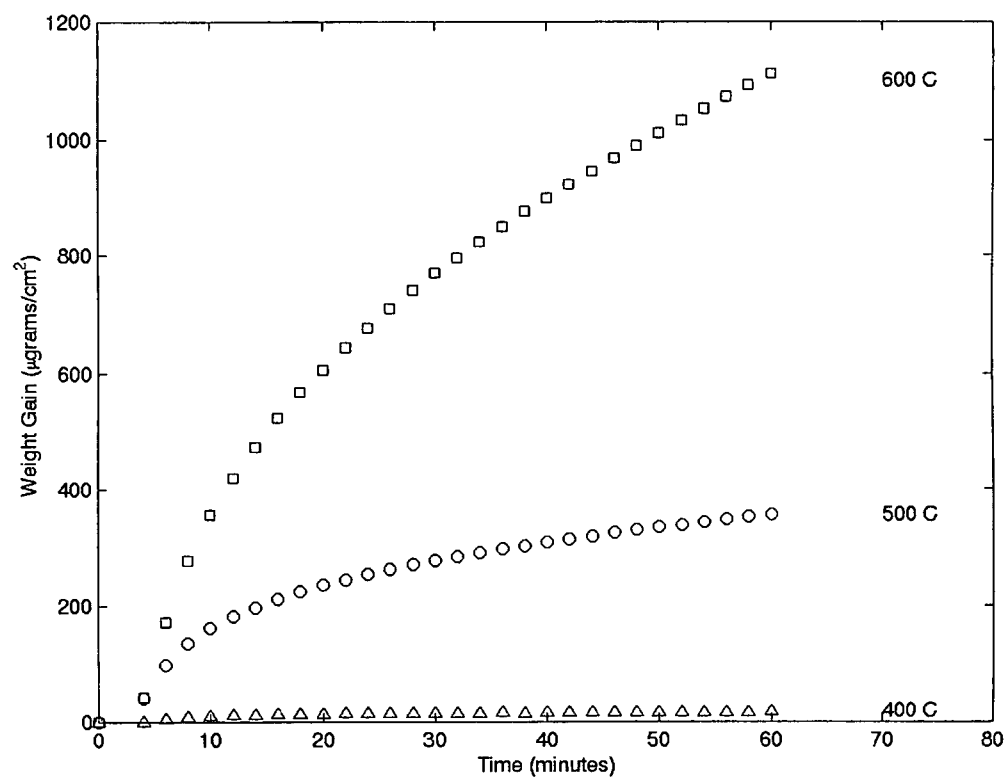


Figure 16. Weight gain by iron in helium carrier gas.

minutes the sample was removed from the TGA, allowed to cool to room temperature, and was then re-exposed to the helium carrier gas exclusively at 500° C for 60 minutes. This sample displayed no additional weight gain during this 60 minute time period. During the initial 30 minutes of exposure to TBPP vapor at 300° C the sample increased in weight by approximately 8 $\mu\text{g}/\text{cm}^2$. This suggests that a very small amount of reaction product on the surface impedes any further gas absorption or diffusion of gas to the surface. Consequently, any significant weight gained by a sample can be attributed to the growth of the reaction product and not to the absorption of carrier gas.

Product Formation

Since platinum is known to be capable of catalyzing the decomposition of phosphate esters [90, 91], a series of experiments were conducted to determine if the vaporous TBPP would react with the surface of the platinum hardware leaving behind any measurable amount of adherent product. This involved monitoring the weight of the hardware while exposing the hardware to TBPP vapor in the carrier gas at each of the temperatures used. These experiments demonstrated that no measurable amount of TBPP or TBPP decomposition byproduct formed and/or remained attached to the platinum at any of the temperatures used in this work over a 2 hour period of time. This same apparent lack of reactivity was also found when silicon nitride substrates in both bulk solid and powdered forms were exposed to the TBPP vapor at all temperatures used in this work.

The extents of the reactions between TBPP vapor and samples of 1010 steel, iron, and iron/platinum laminated foils were measured in terms of a gain in sample weight per unit

apparent surface area. Figures 17 and 18 show how this weight gain varies as a function of time using an iron substrate and a nitrogen carrier gas. These figures show the anomalous weight changes that occur during the initial 10 minutes of exposure. This includes weight changes due to start-up of the equipment, and any initial carrier gas absorption or oxidation by oxygen contamination in the carrier gas. These anomalous weight changes are negligible in comparison to the weight gain due to the reaction product and are therefore considered to be inconsequential. Figure 19 shows similar data for an iron substrate and TBPP vapor in the helium carrier gas. Figure 20 shows this same type of data for an iron/platinum laminated substrate with the helium carrier gas and at a temperature of 500° C. Here, as before, the weight gains are calculated by subtracting the initial weight from the final weight and dividing the difference by the sample's apparent surface area. Figure 20 also shows that the anomalous weight changes due to start-up are clearly restricted to the initial 10 minutes. This reaction rate form shown in Figure 20 was also observed in a duplicate sample of the iron/platinum laminated foil.

A careful comparison of the rate changes depicted in Figures 17 through 20 clearly shows that the product growth rates exhibited by samples in the nitrogen carrier gas are different from the rates exhibited by the same type of samples in the helium carrier gas. Since helium is known to be quite inert on metal surfaces where nitrogen is known to adsorb, dissociate, and react, this is a clear indication that the nitrogen has an effect on the process by which product growth takes place on ferrous surfaces.

Since iron phosphate and poly-phosphates are known to be the major constituents of the product formed on ferrous surfaces, the extent of the reaction between TBPP vapor and

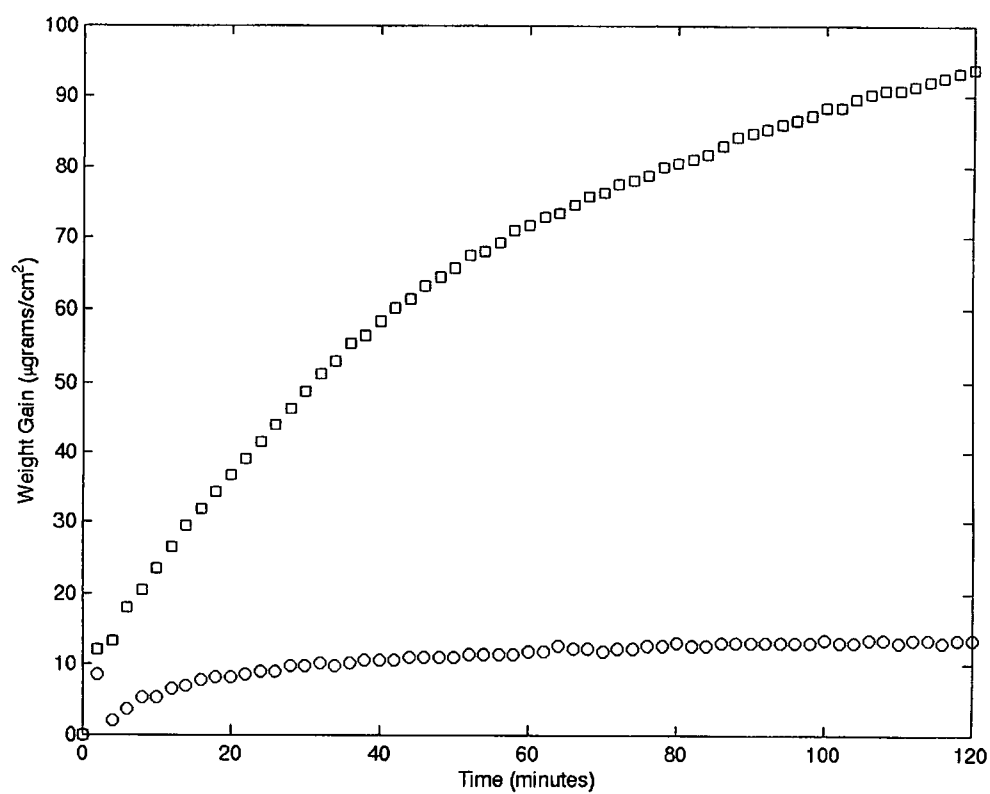


Figure 17. Iron weight gain on exposure to TBPP vapor in nitrogen carrier gas; ○-300°C, □-400°C.

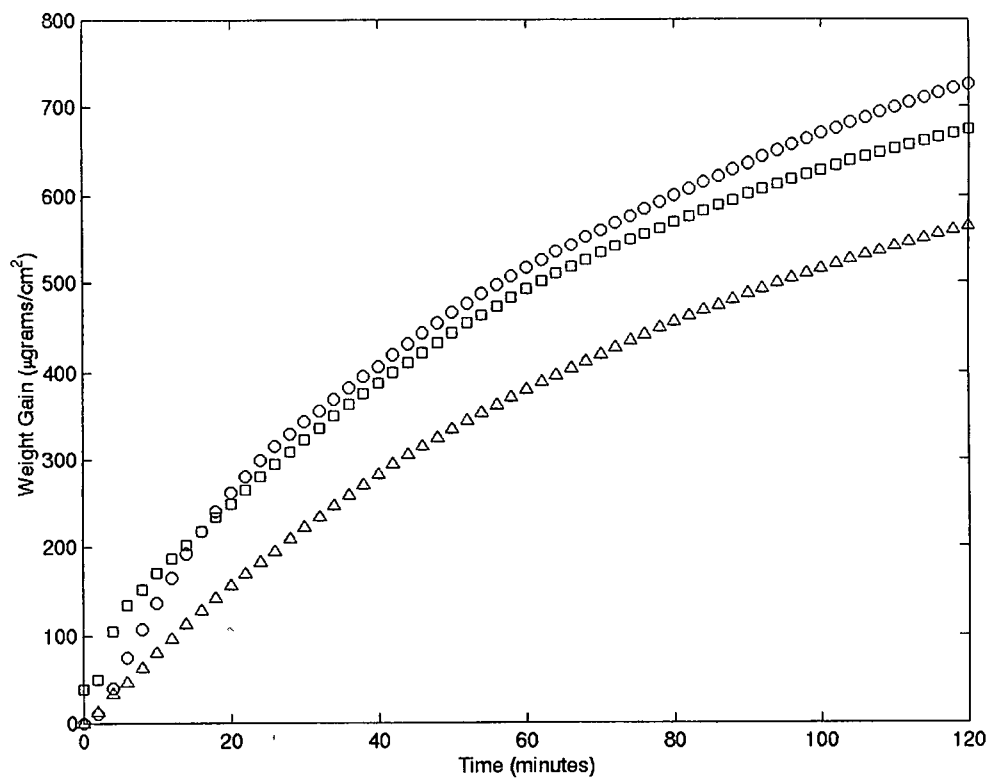


Figure 18. Iron weight gain on exposure to TBPP vapor in nitrogen carrier gas; Δ -450° C, \circ -500° C, \square -600° C.

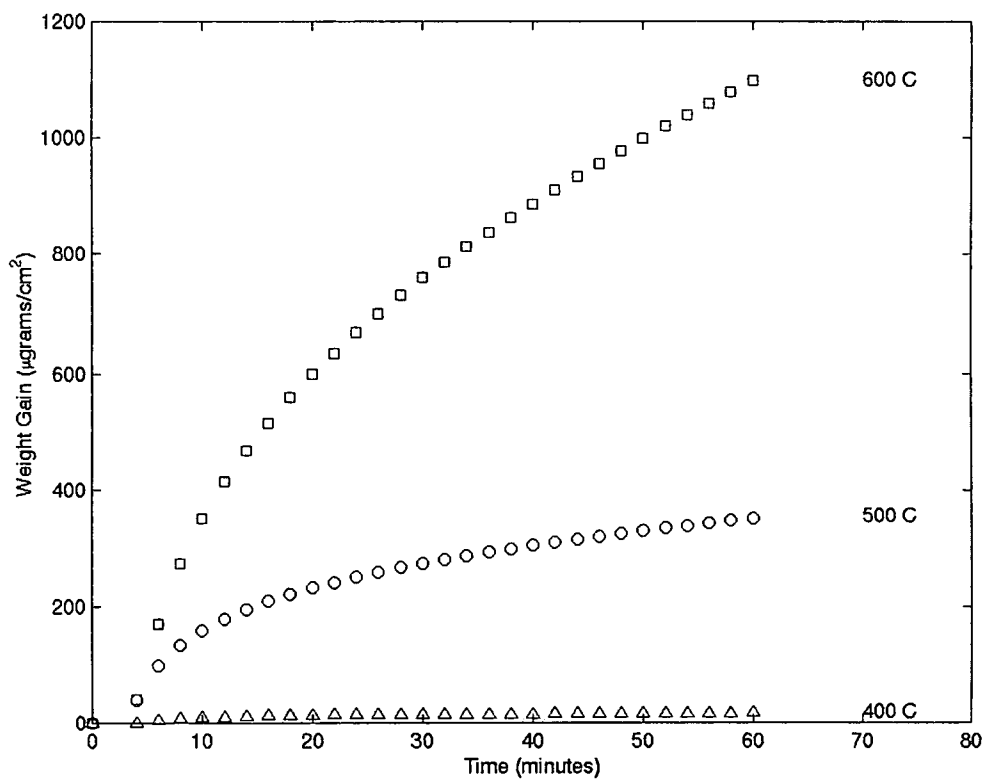


Figure 19. Weight gain by iron on exposure to TBPP vapor in the helium carrier gas; Δ -400° C, \circ -500° C, \square -600° C.

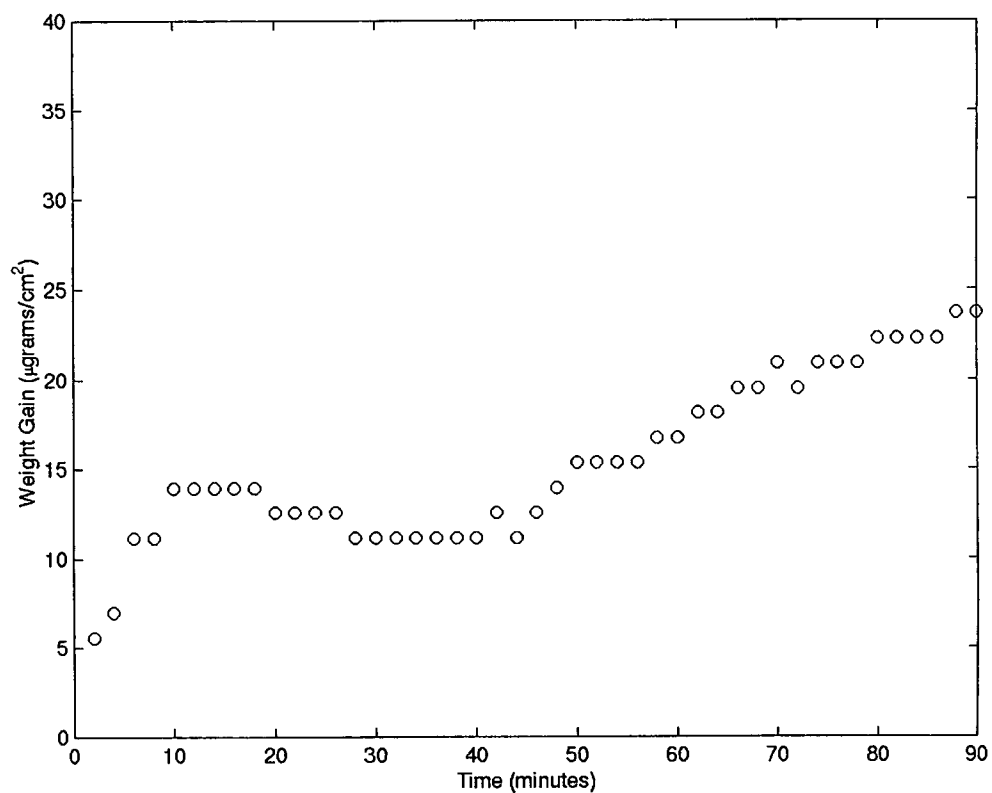


Figure 20. Weight gain by iron/platinum laminated foil on exposure to TBPP vapor in helium carrier gas at 500° C.

iron (III) phosphate was also measured. The results of these experiments are displayed in Figures 21 and 22. The iron (III) phosphate was in the form of a hydrated powder and began dehydrating immediately on exposure to the heated carrier gas. Two samples of this phosphate were exposed to TBPP vapor. One sample was first allowed to dehydrate prior to the exposure while the second was not. The values for weight lost by dehydration and weight gained by product formation on exposure to the TBPP vapor were normalized by dividing the sample weight by the original weight. These are the values that are displayed in Figures 21 and 22.

For the sake of clarity an expanded scale has been used and the initial weights prior to dehydration are not shown, i.e. only the portions of the data that display a weight gain are shown. In these two figures a line with a very large negative slope is found on the far left side of each figure. This line displays a portion of the decrease in weight due to the initial dehydration of each sample. This also includes any of the anomalous weight changes that occur due to start-up. This is followed in time by the injection of the TBPP where a line of positive slope displays the change in weight due to product formation. In Figure 21, the depression in the curve following dehydration is due to the insertion of the needle that dispenses the TBPP into the flow of carrier gas.

This depression is missing from the curve shown in Figure 22 since the insertion of the needle was commensurate with the dehydration process. Since each sample was used in the form of a powder, the actual weight gain per surface area is minuscule. The actual total weight gain by the 22.27 mg sample exposed to TBPP vapor at 400° C was 52 micrograms while the weight gained by the 41.64 mg sample at 500° C was only 8 micrograms.

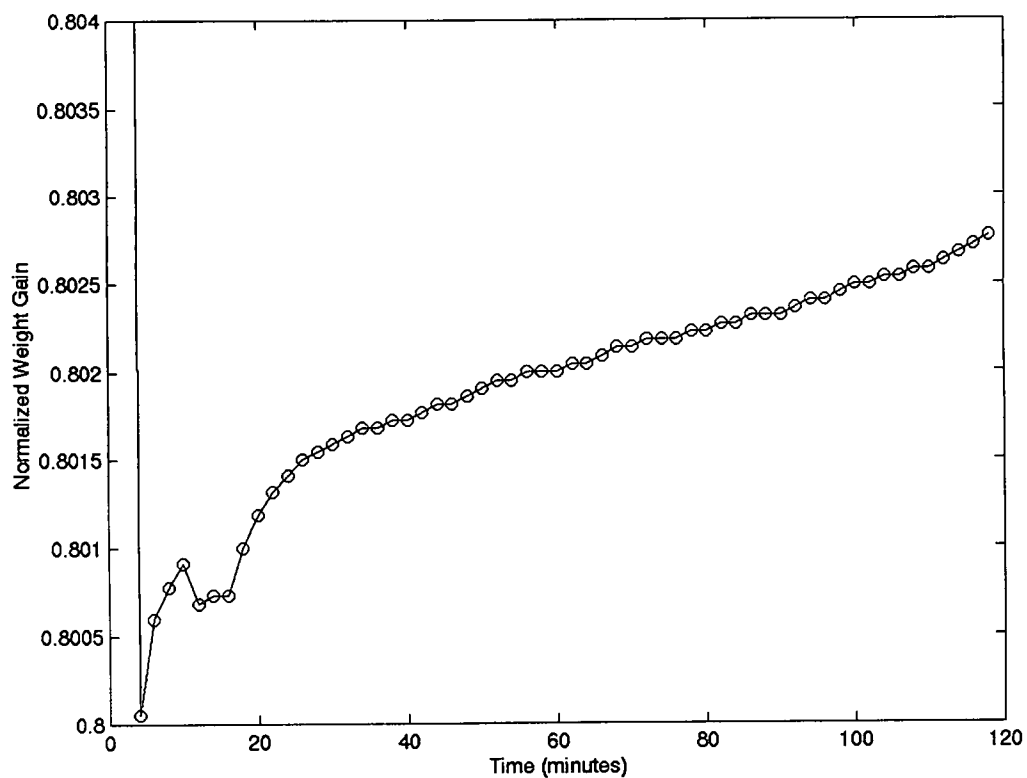


Figure 21. Normalized weight gain by iron (III) phosphate on exposure to TBPP vapor in the nitrogen carrier gas at 400° C.

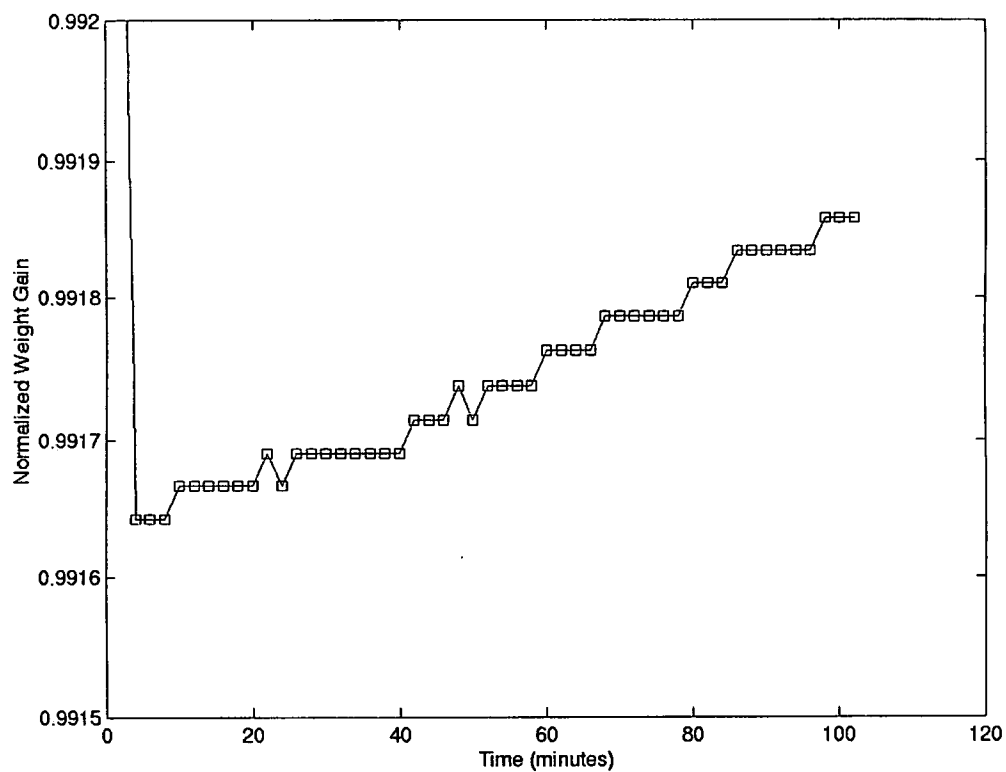


Figure 22. Normalized weight gain by iron (III) phosphate on exposure to TBPP vapor in the nitrogen carrier gas at 500° C.

Each of these samples took on a dark brown to black color after the exposures to TBPP vapor. In a separate set of experiments, samples of the iron (III) phosphate were exposed to the carrier gas alone at these same temperatures to ensure that no sublimation of this phosphate takes place after dehydration. These particular samples displayed no change in color after these exposures.

Each of the samples of iron and steel took on a flat black color after exposure to TBPP vapor at all temperatures. Portions of the black colored product which formed at temperatures ranging from 400° to 600° C detached from their ferrous substrates to varying degrees when the samples were cooled and/or flexed. Micrographs of this detached product lying on the surface of the substrate are shown in Figures 23 through 26. Self adhesive tape was used to remove a portion of this product from the surface. The surface of the substrate from which the product was removed and the surface of the product which was in direct contact with the substrate were scanned using FTIR diffuse reflectance spectroscopy. The samples exposed at 300° C in helium carrier gas took on a dark blue color and showed no evidence of product detachment when flexed. Figures 27 and 28 show the FTIR scans of the product and substrate surface of a sample exposed under these conditions. Since the product in this case is very thin, a great deal of the infrared absorption shown in Figure 27 is likely due to the presence of condensed TBPP and the chemical constituents of the adhesive tape itself. Figures 29 through 34 show the same type of FTIR scans resulting from similar exposures to TBPP vapor in the helium carrier gas at the temperatures shown in the figures.

To one degree or another, three particular features are common to all of the FTIR scans. The first is a series of multiple narrow spikes in the regions of 3,200 to 4,000 cm^{-1}

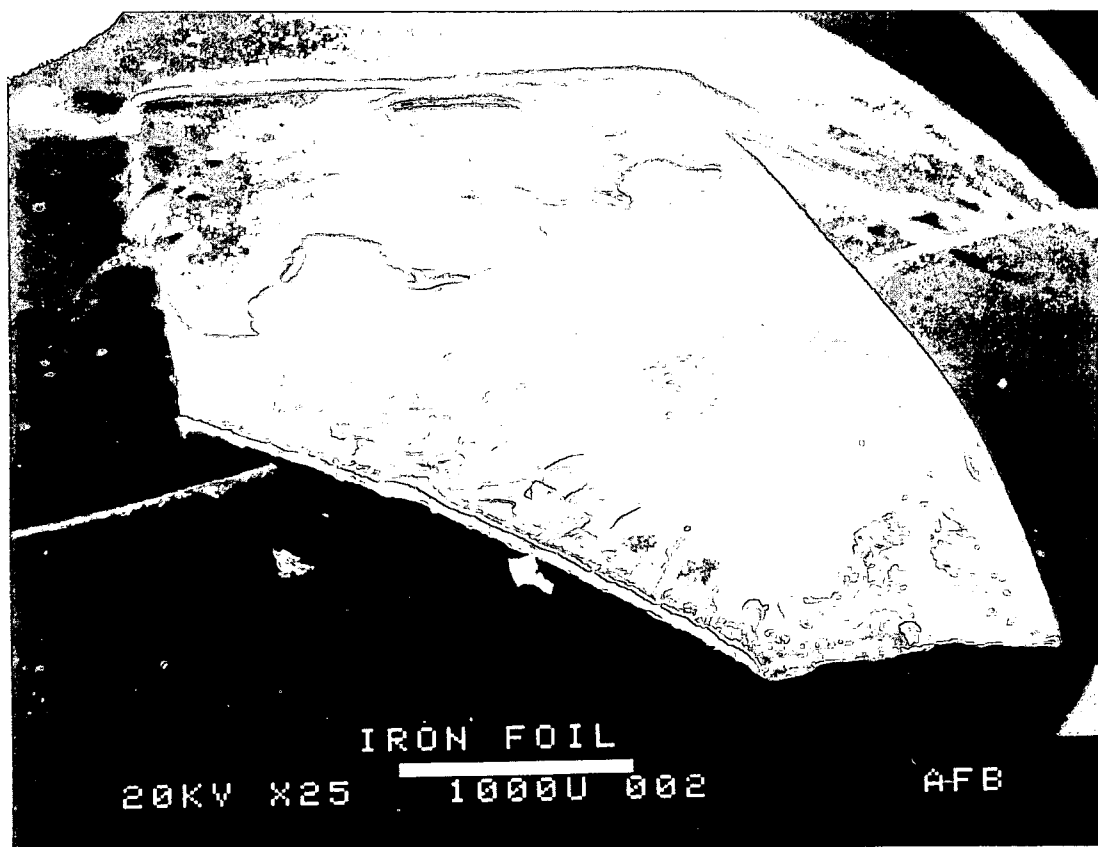


Figure 23. SEM micrograph of iron sample after exposure to TBPP vapor in nitrogen carrier gas at 400° C.

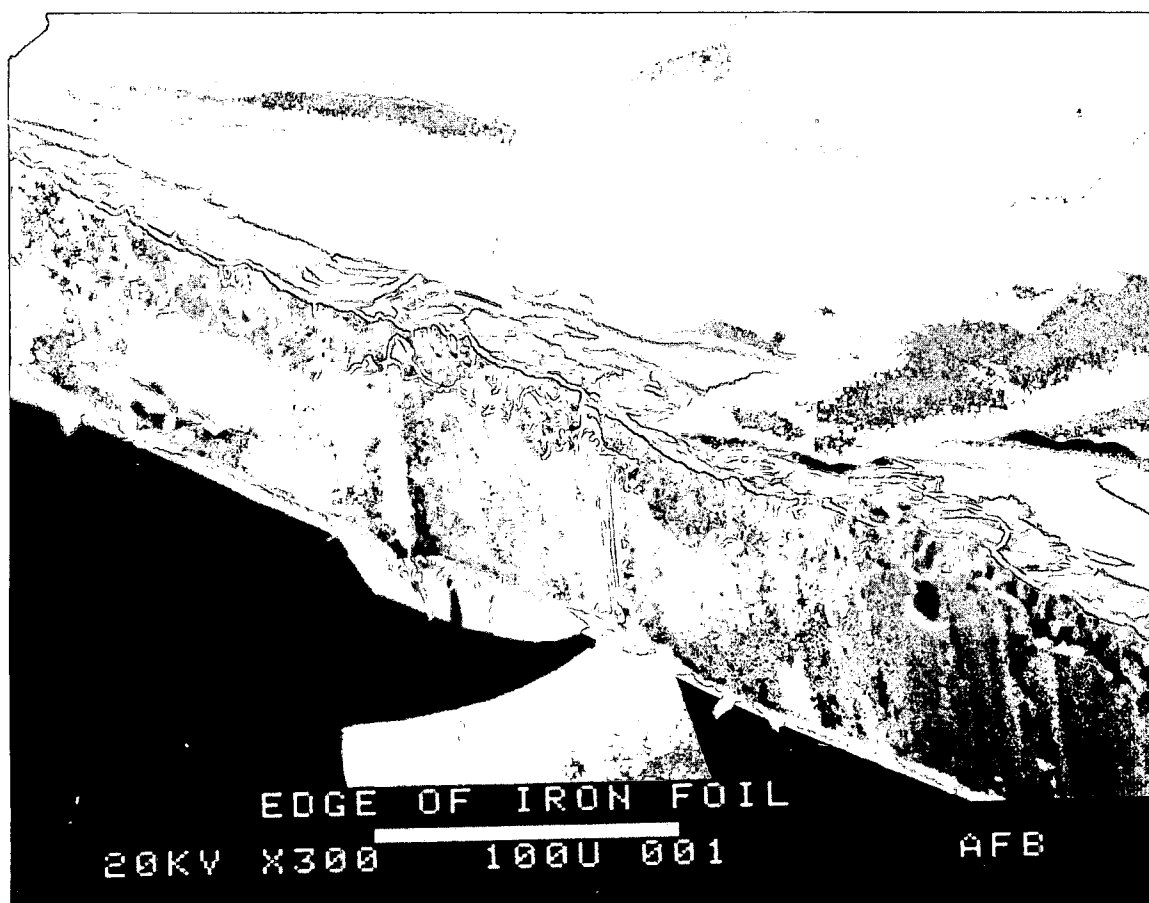


Figure 24. SEM micrograph of the edge of an iron sample after exposure to TBPP vapor in nitrogen carrier gas at 400° C.

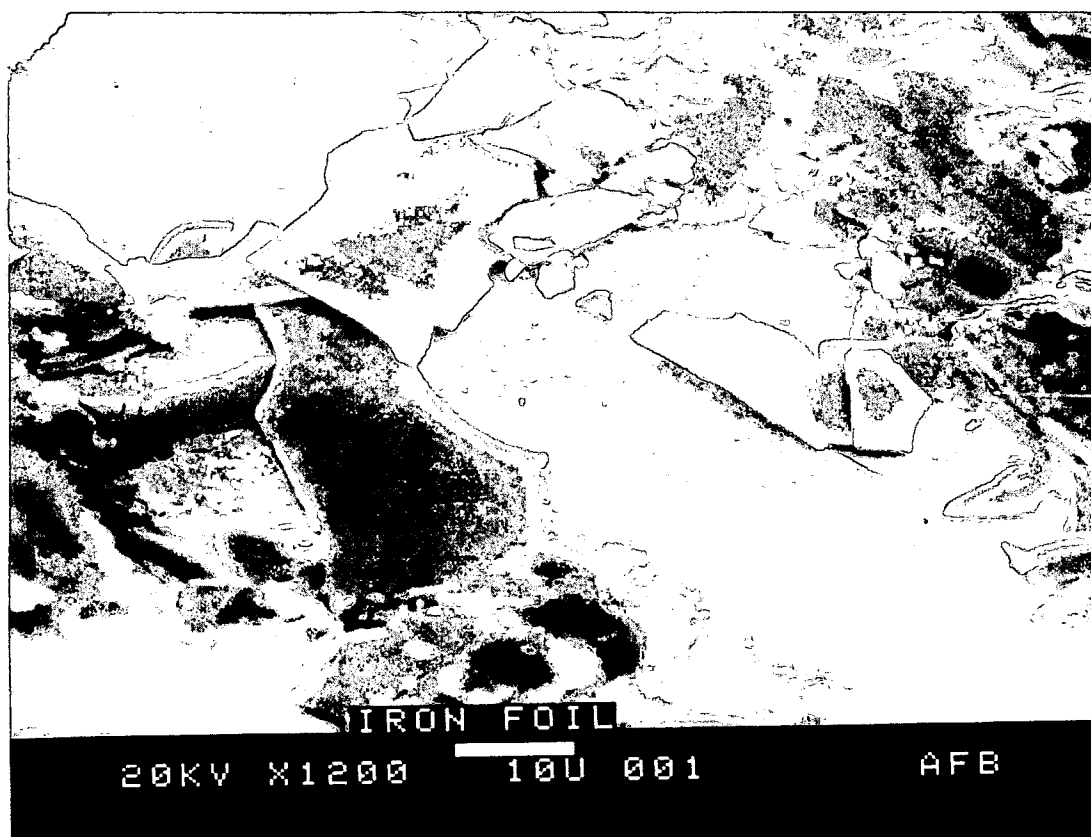


Figure 25. SEM micrograph of detached product on iron sample surface after exposure to TBPP vapor in nitrogen carrier gas at 400° C.

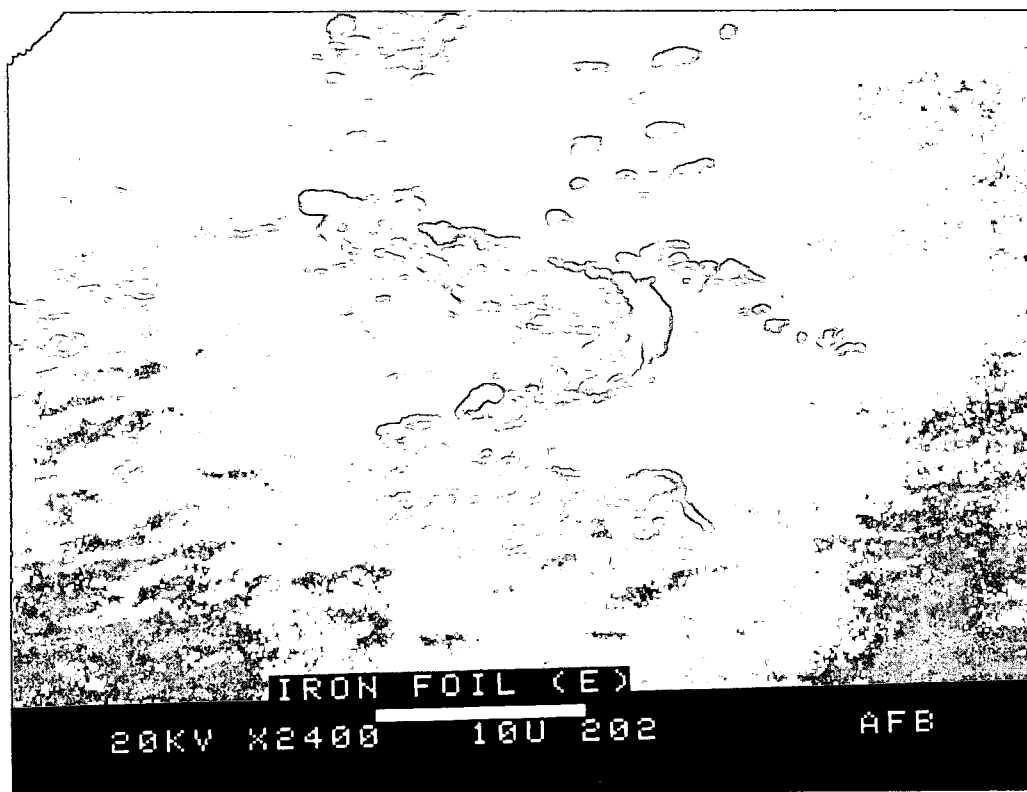


Figure 26. SEM micrograph of the product attached to an iron sample after exposure to TBPP vapor in nitrogen carrier gas at 400° C.

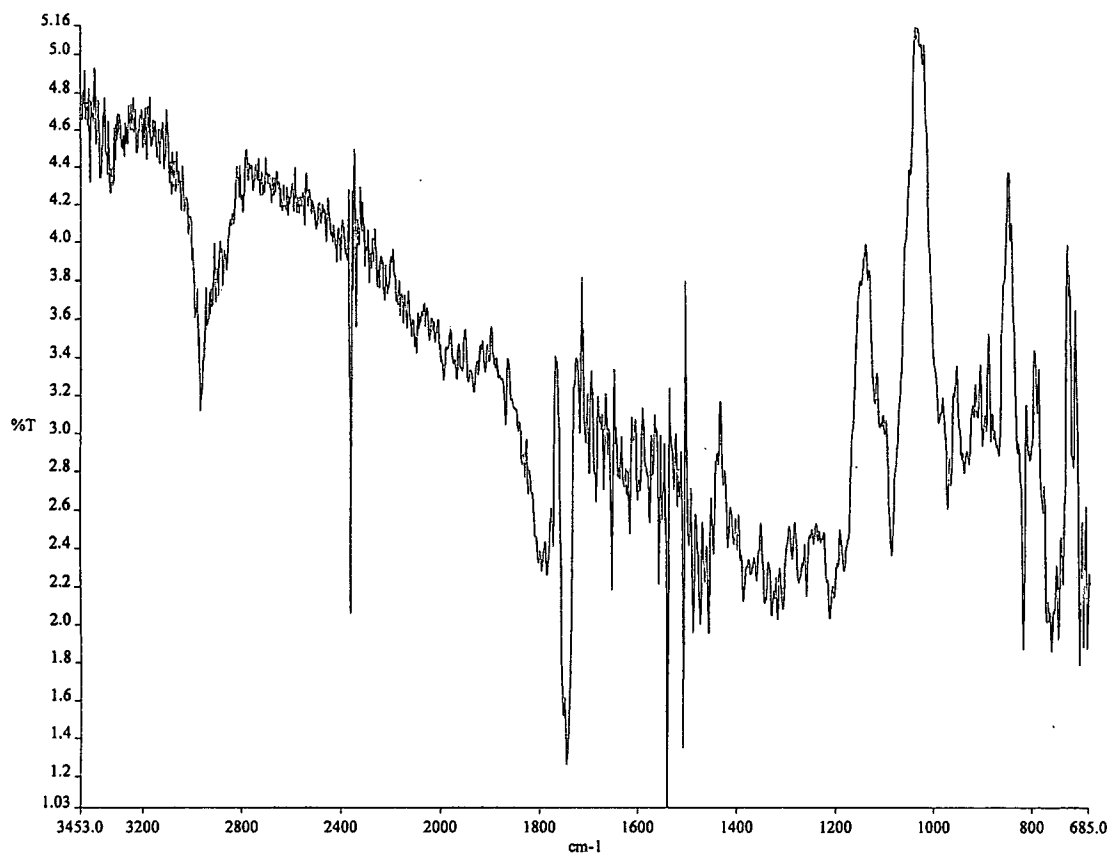


Figure 27. FTIR scan of product formed on iron by exposure to TBPP vapor at 300°C in helium.

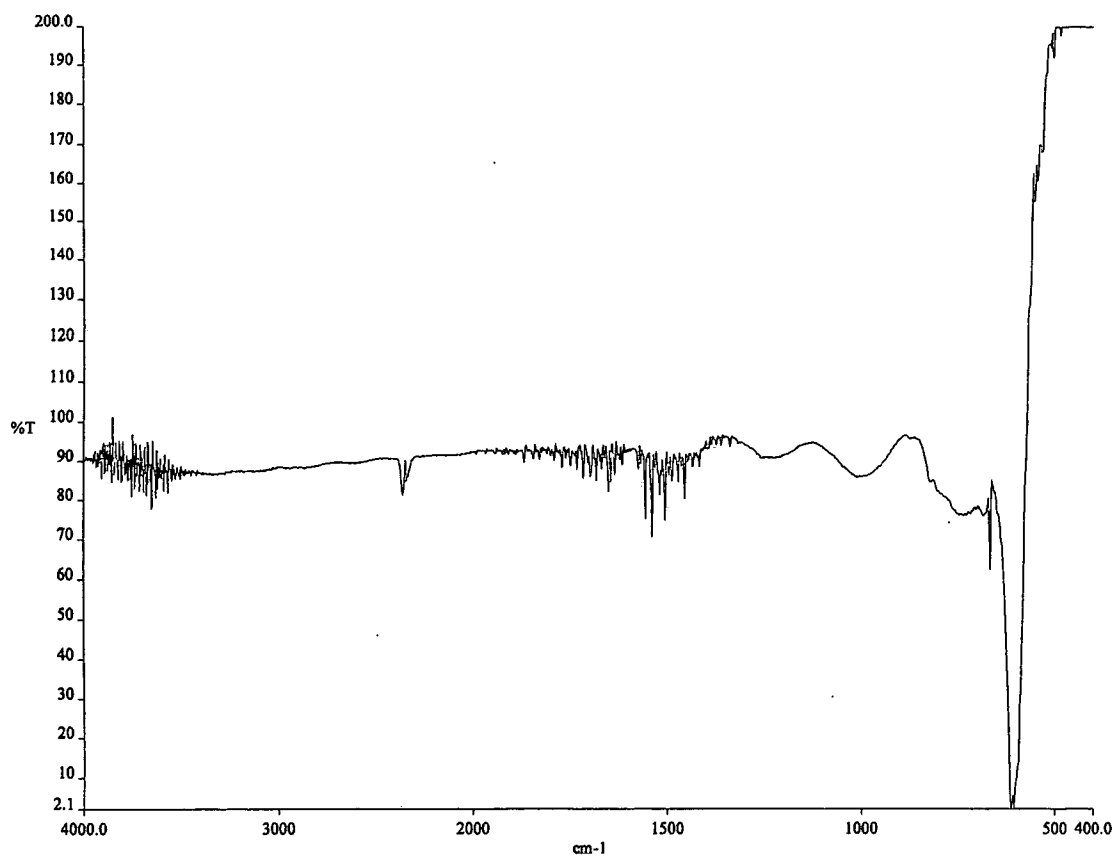


Figure 28. FTIR scan of substrate beneath product formed on iron by exposure to TBPP vapor at 300°C in helium.

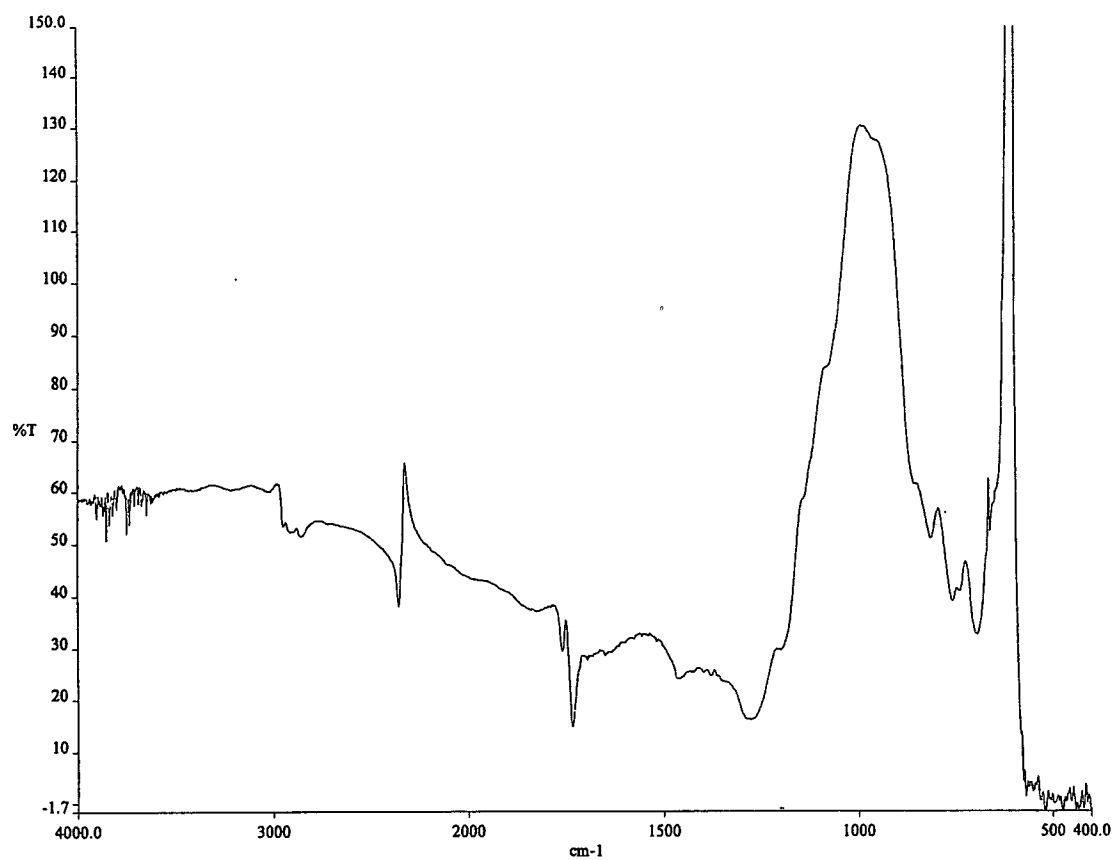


Figure 29. FTIR scan of product formed on iron by exposure to TBPP vapor at 400°C in helium.

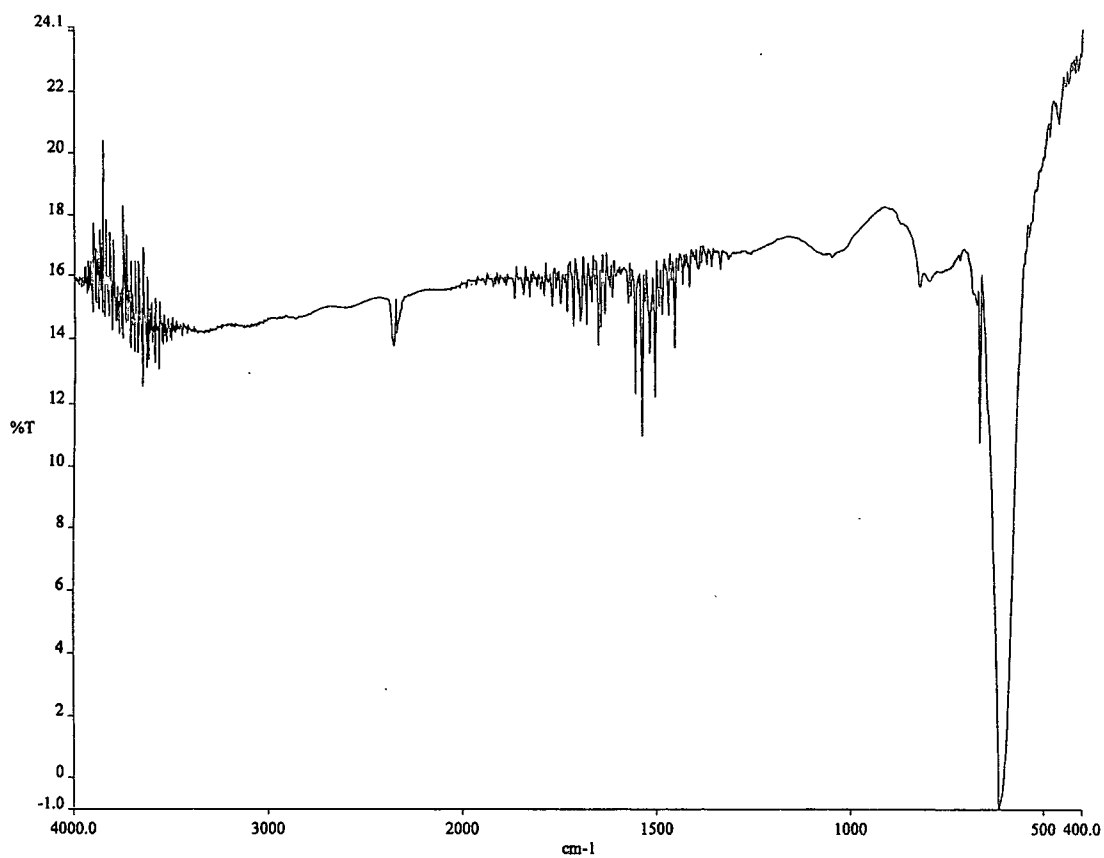


Figure 30. FTIR scan of substrate beneath product formed on iron by exposure to TBPP vapor at 400°C in helium.

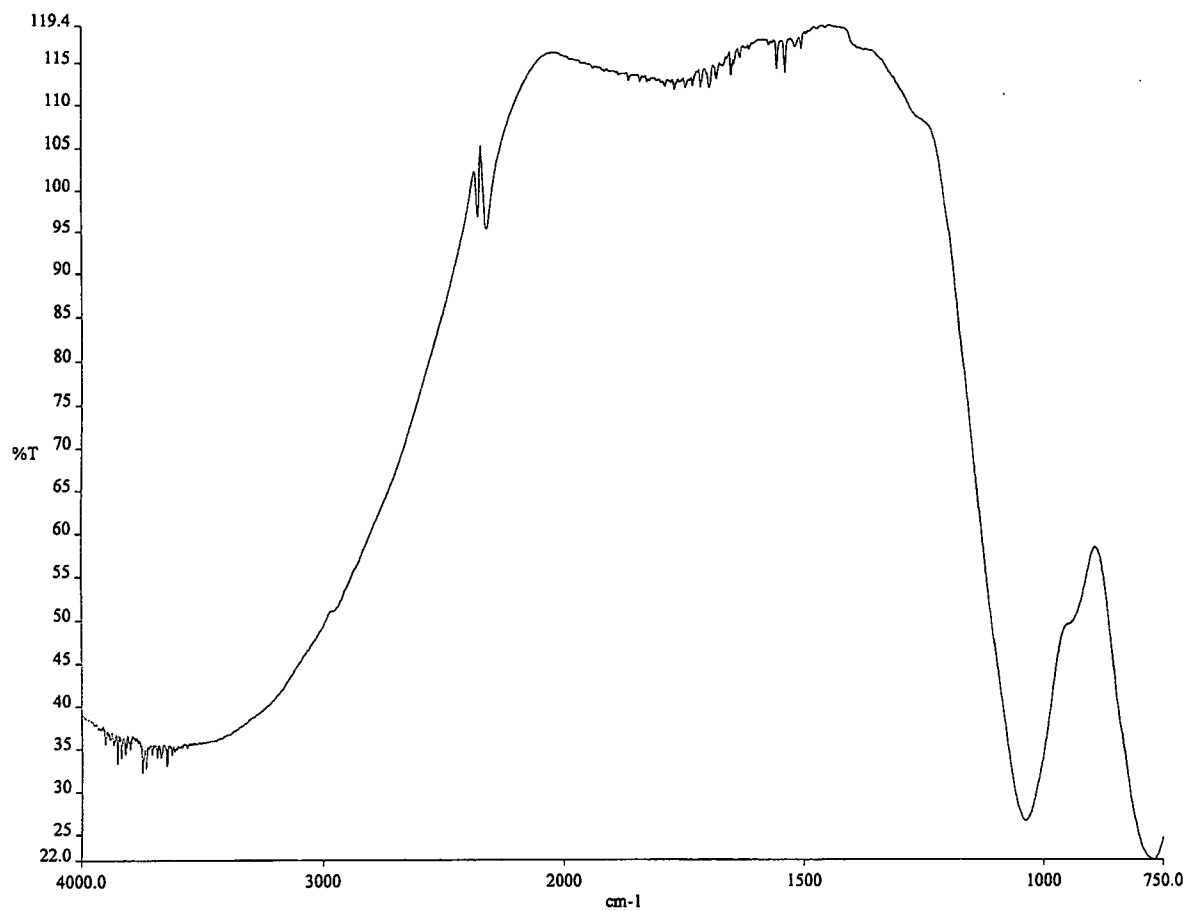


Figure 31. FTIR scan of product formed on iron by exposure to TBPP vapor at 500° C in helium

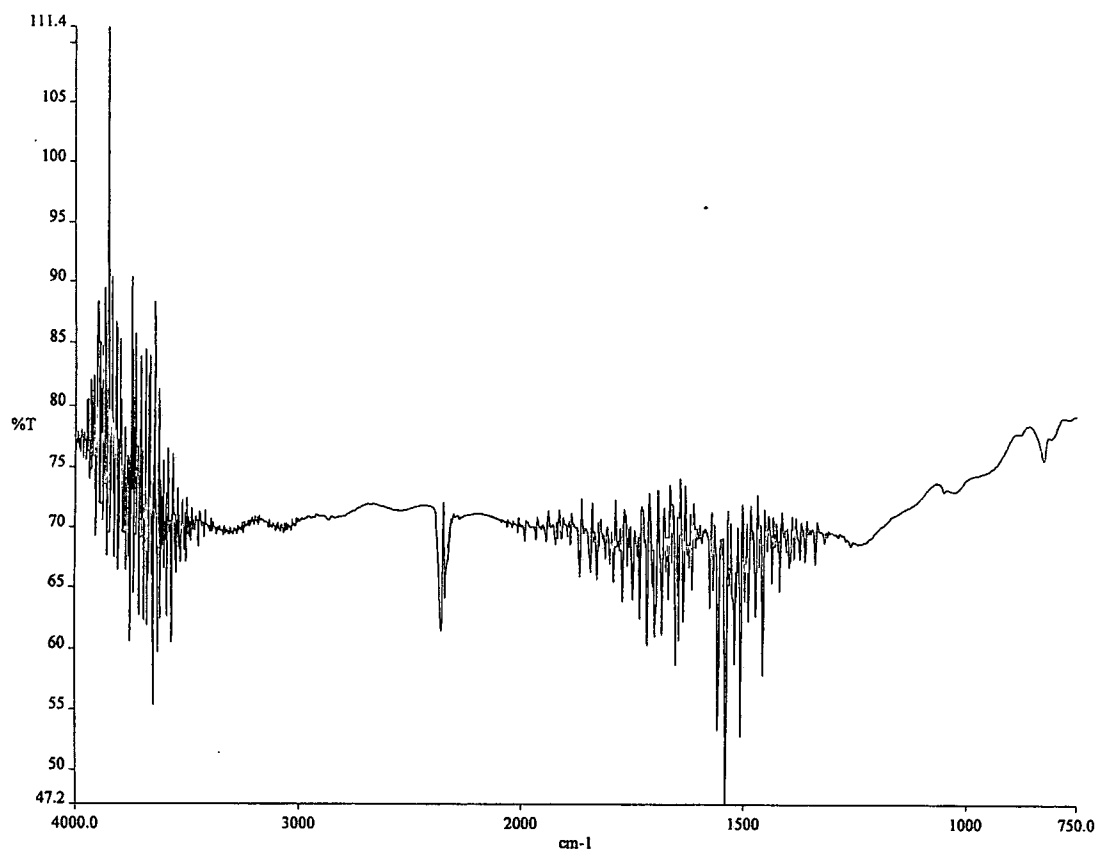


Figure 32. FTIR scan of substrate beneath product formed on iron by exposure to TBPP vapor at 500°C in helium.

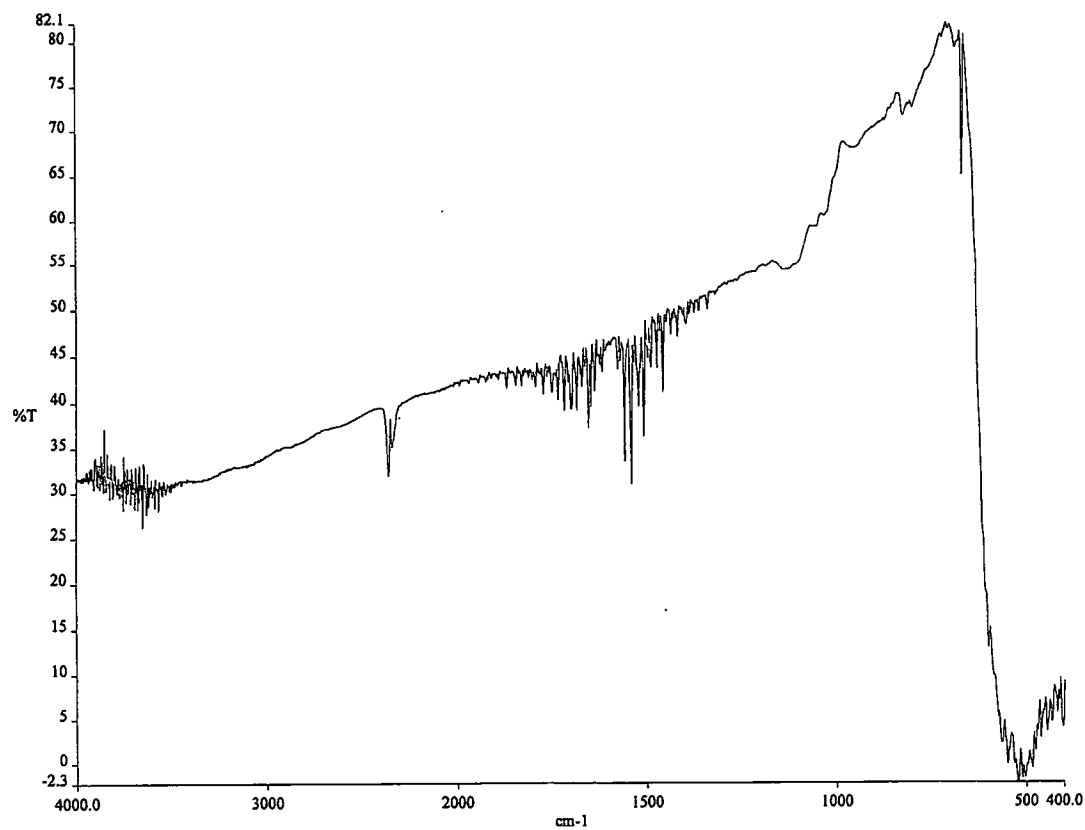


Figure 33. FTIR scan of product formed on iron by exposure to TBPP vapor at 600° C in helium.

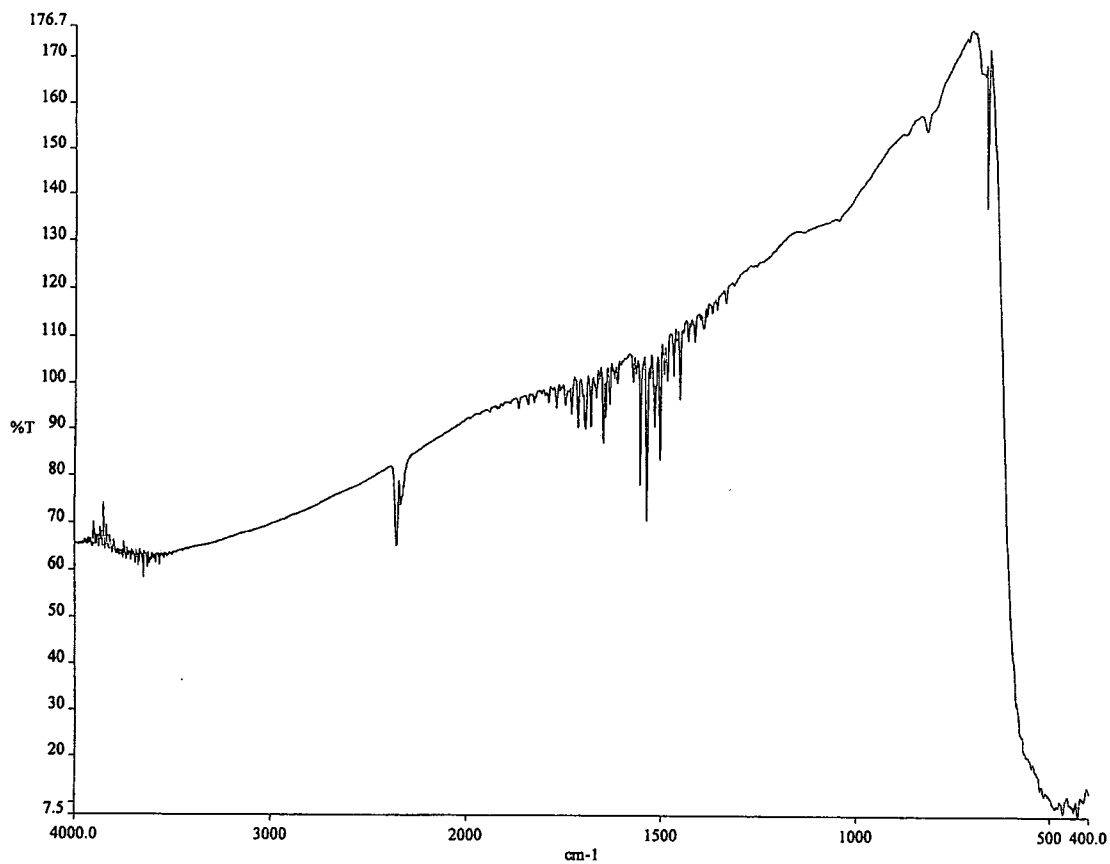


Figure 34. FTIR scan of substrate beneath product formed on iron by exposure to TBPP vapor at 600°C in helium

and 1,400 to 2,000 cm^{-1} . These are due to the presence of moisture likely adsorbed from the surrounding air. The second is the small pair of peaks appearing around 2,349 cm^{-1} . This is the typical doublet due to the presence of carbon dioxide. The third is a sharp peak, appearing between 665 and 667 cm^{-1} which is also attributed to carbon dioxide. As in the case of the water, this carbon dioxide was also likely adsorbed from the surrounding air and/or possibly generated as a byproduct during the cooling of the sample. This type of carbon oxidation was reported by Paciorek and coworkers [74, 75] to take place on exposure to air at high temperatures. In the adsorbed state on AgO and NiO, carbon dioxide is reported to exhibit IR absorption around 2350 cm^{-1} [92, 93]. Wang and Tung [65] identified similar FTIR peaks between 2340 and 2360 cm^{-1} as indicating the presence of carbon dioxide in a solution of dilauryl hydrogen phosphate in mineral oil which had experienced electrolysis in the presence of cast iron electrodes. Additionally, they assigned peaks at 2,850 to 3,000 cm^{-1} to C-H bonding. This is similarly most likely the source of the small peaks at 2960 cm^{-1} shown in Figures 27 through 34. The most significant features of these spectra are the broad absorption bands appearing at 900 to 1,180 cm^{-1} and at 760 to 850 cm^{-1} . These are consistent with the major absorption bands seen in the spectra of both iron (II) ortho-phosphate and iron (III) ortho-phosphate [94] and the P-O-P bridge found in poly-phosphates [101, 102]. These bands, as shown in Figures 27 and 28, are nearly identical in both shape and position to the band reported by Forster for a product formed from the reaction between TBPP vapor and the surface of a T15 steel ball bearing at 370° C under dynamic load conditions [95]. Forster attributed this to a mixture of PO_4^{-3} , PO_3^{-2} , and the possible presence of P-O-P bridge bonding. The prominent absorption peak at 600 cm^{-1} is attributed to PO_4^{-3}

phosphate ion as reported by Balamurugan et al. [103]. Fang et al. also assign the absorption bands at approximately 760 cm^{-1} to the P-O-P bridge bonding in phosphate glasses [100]. Johnson et al. [72] assign the series of bands between 900 and 1100 cm^{-1} to P-O bonding in a product formed on a metal surface exposed to the same TBPP material used in this work. This band is attributed to the phosphate ion by others as well. However, the existence of the two broad absorption bands seen in the figures may be together characteristic of P-O-C stretching in which the carbon is aliphatic [96, 97]. In conjunction with this, the spectra show an absence of the aromatic ring C=C stretching at $1400\text{-}1600\text{ cm}^{-1}$ [98]. Additionally, the absorption that would be associated with an aromatic C-H stretching is absent with only the very small absorption peaks characteristic of aliphatic C-H stretching appearing at 2890 cm^{-1} . The broad absorption band extending from $2,500\text{ cm}^{-1}$ through $4,000\text{ cm}^{-1}$ is ascribed to water which likely adsorbed onto the product surface. Muneyama et al. have reported similar absorption on iron phosphate and pyro-phosphate [99]. This feature is also found in various reference spectra for different hydrated forms of iron phosphate [94].

The EDS (Energy Dispersive Spectroscopy) analysis of the product formed on an iron surface exposed to TBPP vapor at 400°C in a nitrogen carrier gas is shown in Figure 35. As can be seen in the figure, the major constituent elements are iron, phosphorous, and oxygen.

Samples of the iron/platinum laminated material were exposed to TBPP vapor at the single temperature of 500°C for varying amounts of time. These samples displayed colors of blue and violet following their exposure. The top portion of samples exposed for 70 minutes showed a surface detachment similar to the detachment of product that had

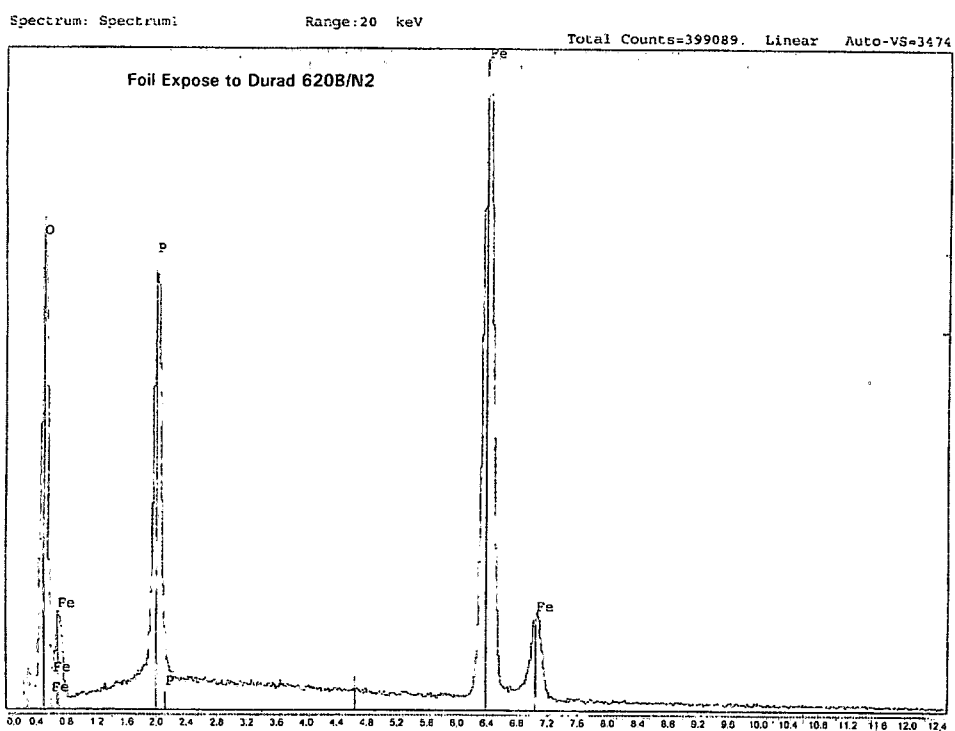


Figure 35. EDS of iron foil exposed to TBPP vapor in nitrogen at 400° C.

formed on pure iron. An SEM micrograph of a sample of the laminated material with surface detachment after exposure is shown in Figure 36. The chemical composition of the product layer formed on the surface of this laminated metal was then determined via AES (Auger Electron Spectroscopy). This was followed by sputtering the surface with argon ions for a pre-determined period of time. The remaining surface was then reanalyzed using AES analysis. This process of sputtering followed by AES analysis was repeated until the interface between the iron and the platinum was reached. The process of repeated sputtering followed by AES analysis provides the approximate concentrations of the elements as a function of depth into the product layer. From the known thickness of the original iron layer, the sputtering rate for this layer was estimated to be 6 nm/minute.

Figure 37 is a re-scaled version of Figure 8, the concentration-depth profile for a sample of the laminated material prior to any exposure to the TBPP vapor. This rescaling facilitates the comparison of this figure to the concentration-depth profiles that follow.

Figures 38 and 39 show the concentration-depth profiles for samples which were exposed to TBPP vapor for 30 minutes and 70 minutes respectively. Figure 40 shows the resulting concentration-depth profile for a sample of the iron/platinum laminated material that was exposed to carrier gas containing a trace amount of TBPP for a 70 minute time period. In each of these concentration-depth profiles, the interface between the iron and the platinum is shown on the far right side while the interface with the TBPP vapor and carrier gas is shown on the far left. Tables 2, 3 and 4 list the Auger electron energies for the various constituent elements at various locations throughout each sample.

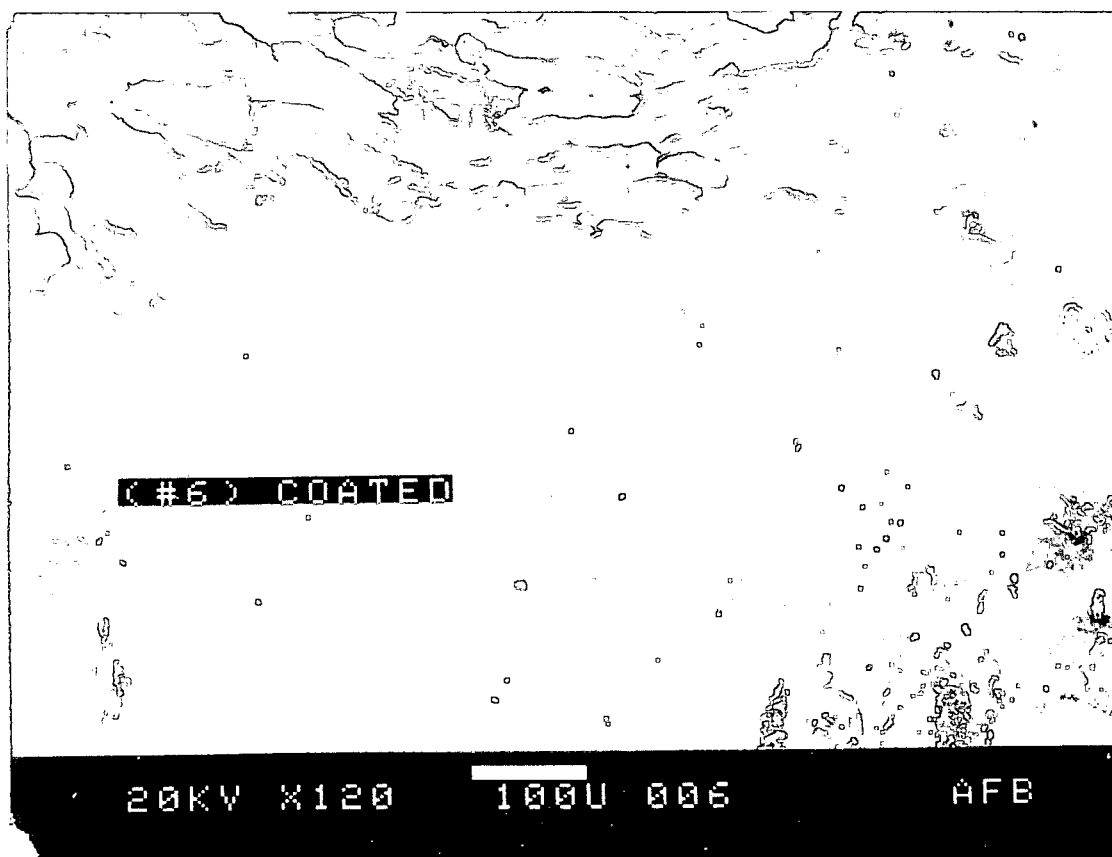


Figure 36. Iron/platinum laminated foil sample after exposure to TBPP vapor at 500° C.

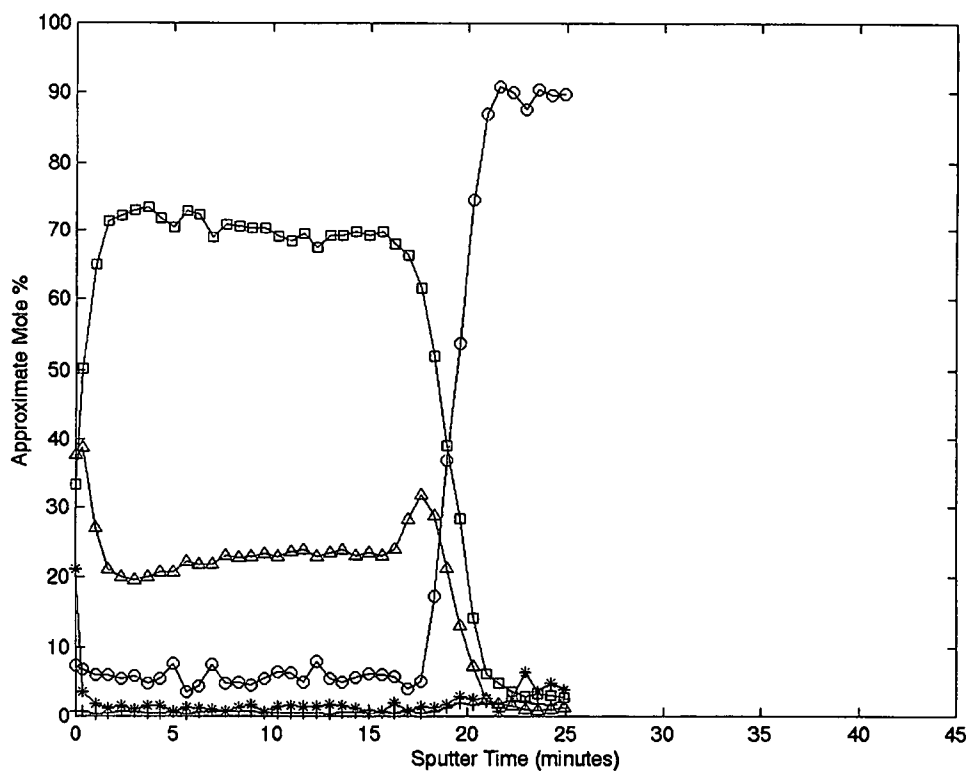


Figure 37. Concentration-depth profile for a laminated iron/platinum foil. ○ -Platinum, □-Iron, △-Oxygen, + -Phosphorous, *-Carbon.

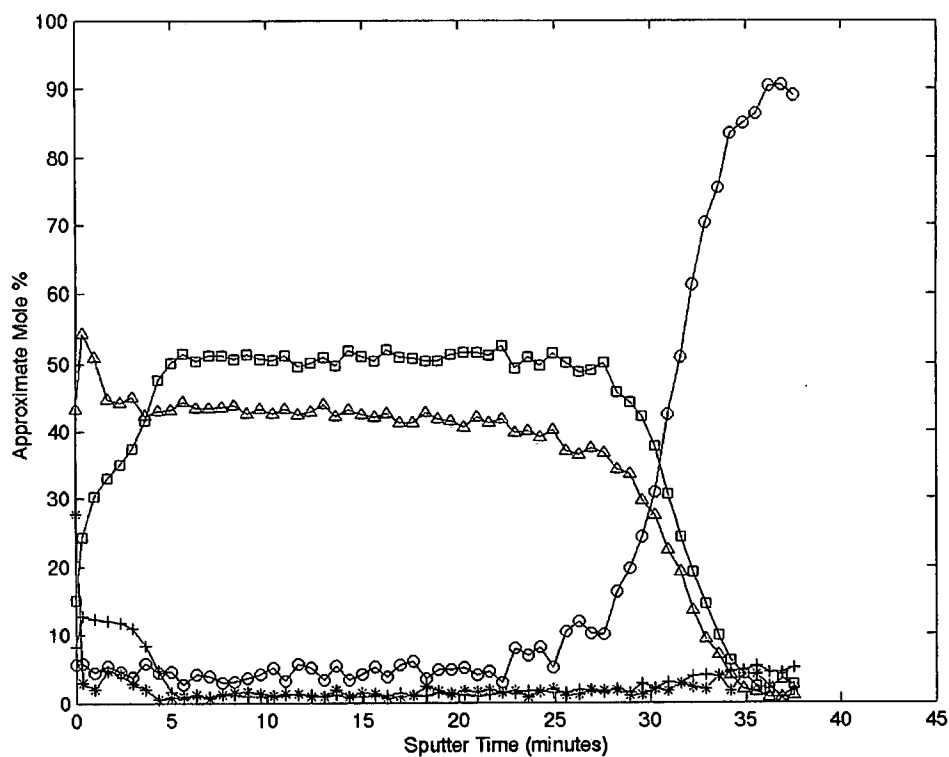


Figure 38. Concentration-depth profile for a laminated iron/platinum foil after a 30 minute exposure to a helium/TBPP mixture: ○ -Platinum, □ -Iron, △-Oxygen, +-Phosphorous, *-Carbon

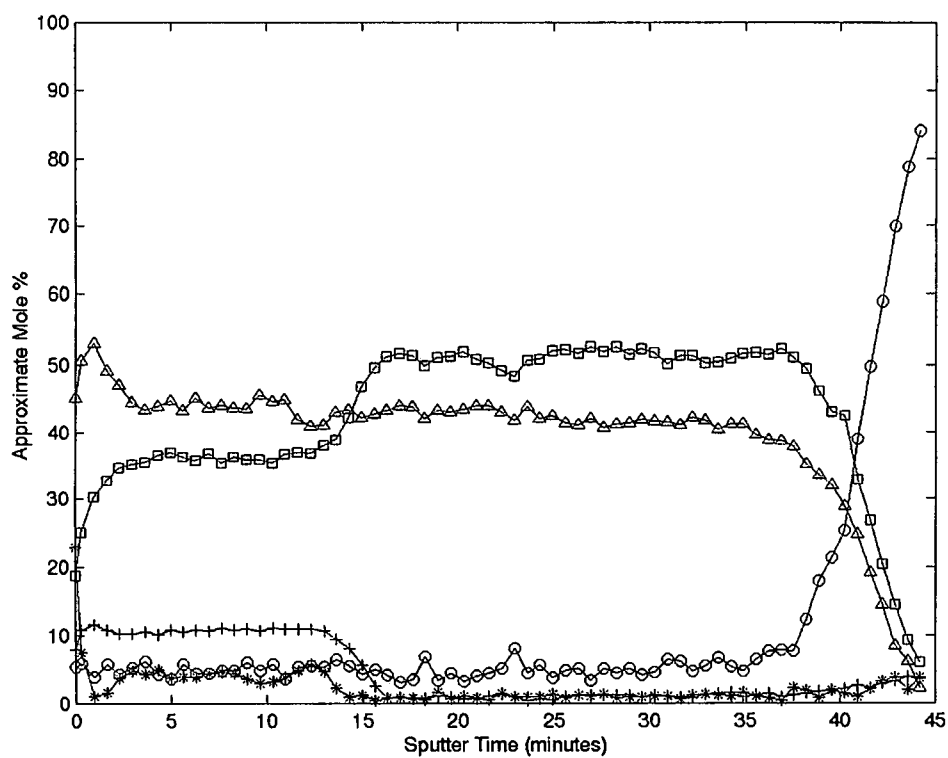


Figure 39. Concentration-depth profile for a laminated iron/platinum foil after a 70 minute exposure. ○ -Platinum, □ -Iron, △ -Oxygen, + -Phosphorous, * -Carbon

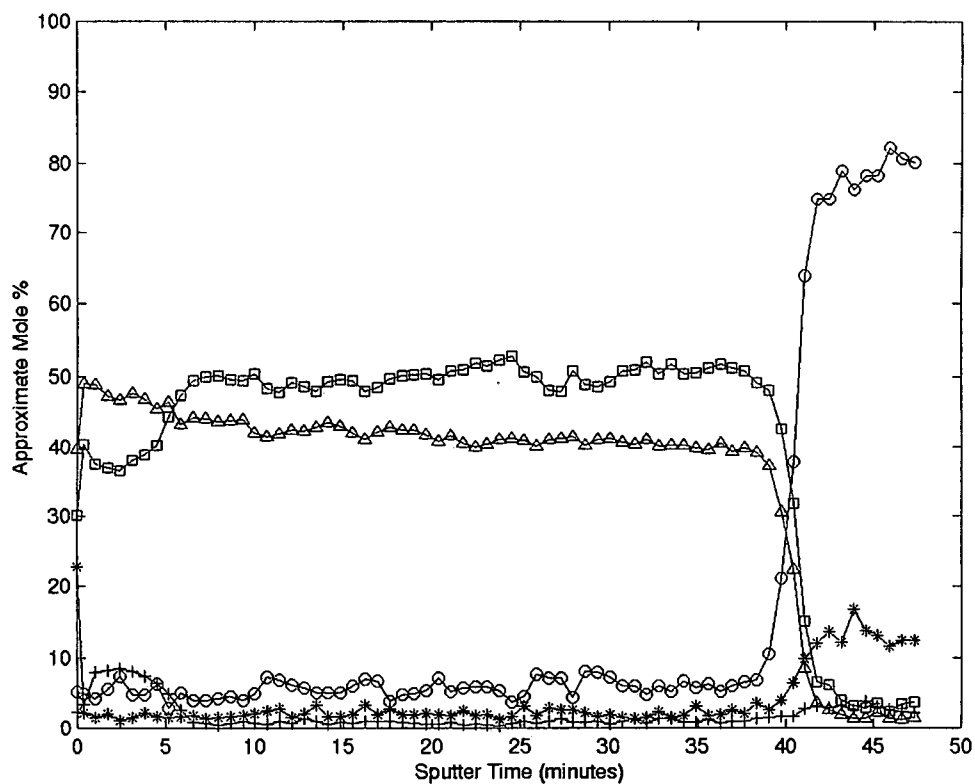


Figure 40. Concentration-depth profile for a laminated iron/platinum foil after a 70 minute exposure to trace TBPP vapor in helium, ○ -Platinum, * -Iron, △-Oxygen, +-Phosphorous, * -Carbon.

Table 2. Auger electron energies of the elements within the iron layer of an unexposed sample of the laminated foil.

Sputter Depth (min)	Auger electron energy (eV)			
	Fe _{LMM}	O _{KLL}	P _{LMM}	C _{KLL}
0	652.50	515.00	-	-
2.3	655.00	515.00	-	-
9.6	655.00	515.00	-	-
17.6	655.00	515.00	-	-

Table 3. Auger electron energies of the elements within the iron layer of a sample of the laminated foil exposed for 30 minutes to TBPP vapor in helium at 500° C.

Sputter Depth (min)	Auger electron energy (eV)			
	Fe _{LMM}	O _{KLL}	P _{LMM}	C _{KLL}
0	650.00	511.25	111.25	270.00
1.7	651.25	512.50	116.25	271.25
9.6	652.50	513.75	-	-

Table 4. Auger electron energies of the elements within the iron layer of a sample of the laminated foil exposed for 70 minutes to TBPP vapor in helium at 500° C.

Sputter Depth (min)	Auger electron energy (eV)			
	Fe _{LMM}	O _{KLL}	P _{LMM}	C _{KLL}
0	648.75	510.00	110.00	270.00
1.0	650.00	511.25	112.50	266.25
7.0	650.00	511.25	115.00	272.50
12.3	-	-	116.25	-
15.0	-	-	116.25	-
25.6	652.50	513.75	-	-

Figure 41 displays the spectra for the phosphorus Auger electrons at the depths reached by sputtering for 0, 1, 7 and 12.3 minutes (see Table 4).

All of these concentration-depth profiles are displayed in terms of mole percent concentration and the amount of time taken to sputter to the depth at which the concentration was measured. The depth axes of these profiles can be expressed in terms of an actual distance by multiplying the sputter depth (in terms of time) by the applicable sputter rate which is a function of sputter yield. Since no independent measure of sputter rate or sputter yield was available, the applicable sputter rates were determined as follows by taking advantage of the knowledge that all of the iron existent in the product originated in the substrate.

The value for the sputter time at the interface between the iron and the platinum as shown in Figure 38 is designated as τ_0 and the corresponding total number of moles as N_0 . Similarly, the value for the iron/platinum sputter time in Figures 40 is designated as τ_{70} and the corresponding total number of moles as N_{70} . The total number of moles of iron in the original unexposed sample is given by,

$$\frac{N_0 \int_0^{\tau_0} f_0 d\tau}{\tau_0}$$

where f_0 represents the mole fraction of iron in the original unexposed sample.

The total number of moles of iron in the sample shown in Figure 40 is given by,

$$\frac{N_{70} \int_0^{\tau_{70}} f_{70} d\tau}{\tau_{70}}$$

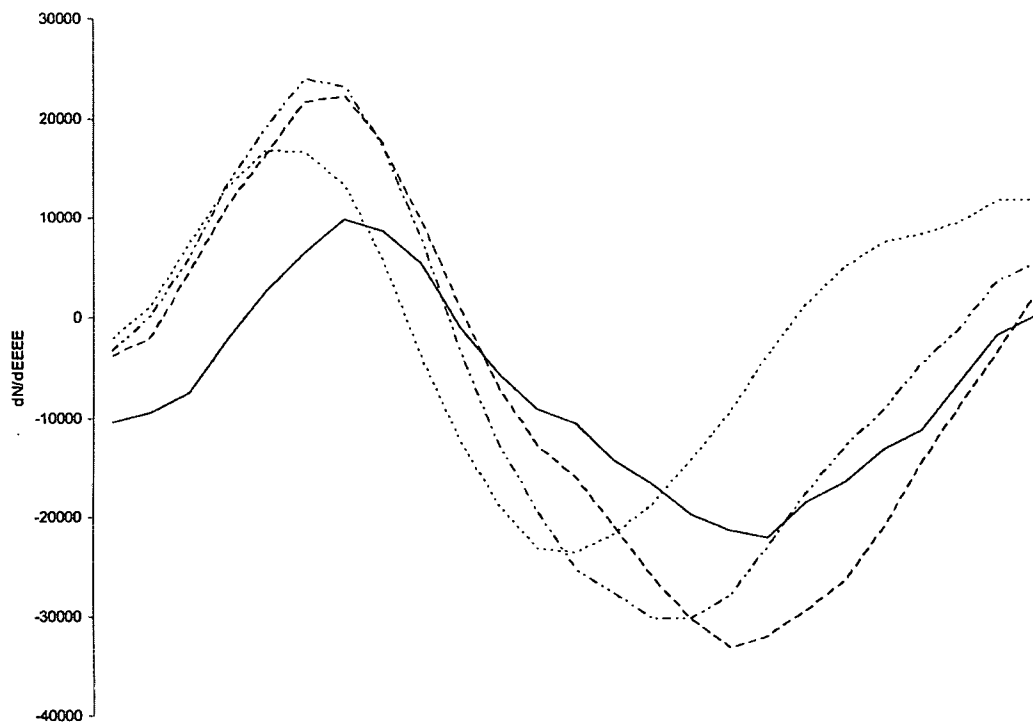


Figure 41. Peak Auger electron energies for phosphorous, 110.00 eV,
 - · - · 112.50 eV, ----- 115.00 eV, ——— 116.25 eV.

where f_{70} represents the mole fraction of iron within the profiles shown in this figure. Since the total number of moles of iron in these two samples are the same, these two expressions can be equated as shown in equation 1 below:

$$\frac{N_0 \int_0^{\tau_0} f_0 d\tau}{\tau_0} = \frac{N_{70} \int_0^{\tau_{70}} f_{70} d\tau}{\tau_{70}} \quad (1)$$

The sputter times τ_0 and τ_{70} can be expressed in terms of sputter rates R_0 and R_{70} and actual distances (depths) θ_0 and θ_{70} respectively as

$$\tau_0 = \frac{\theta_0}{R_0} \quad \text{and} \quad \tau_{70} = \frac{\theta_{70}}{R_{70}}$$

These expressions for τ can be substituted into Equation 1 to give

$$\frac{R_0 N_0 \int_0^{\tau_0} f_0 d\tau}{\theta_0} = \frac{R_{70} N_{70} \int_0^{\tau_{70}} f_{70} d\tau}{\theta_{70}}$$

The ratio of the sputter rates can then be expressed by rearranging this equation to

$$\frac{R_0}{R_{70}} = \frac{N_{70} \theta_0 \int_0^{\tau_{70}} f_{70} d\tau}{N_0 \theta_{70} \int_0^{\tau_0} f_0 d\tau}$$

This ratio of sputter rates can then be calculated by integrating f_{70} and f_0 and evaluating the ratio of total molar volumes. Since the original unexposed sample is essentially iron, a good estimate of N_0/θ_0 is the total number of moles of iron per unit volume in pure iron. Similarly, a good estimate of N_{70}/θ_{70} is the total number of moles of iron and oxygen in magnetite per unit volume. Thus, these ratios can be estimated by:

$$\frac{N_0}{\theta_0} = \frac{\rho_{Fe} N_A}{M_{Fe}} \quad \text{and} \quad \frac{N_{70}}{\theta_{70}} = \frac{7 \rho_{Mag} N_A}{M_{Mag}}$$

where ρ_{Fe} is the density of pure iron, ρ_{Mag} is the density of pure magnetite, M_{Fe} is the molecular weight of iron, M_{Mag} is the molecular weight of magnetite, and N_A is Avogadro's number.

Inserting these numerical values into the previous expressions results in,

$$\frac{N_{70}\theta_0}{N_0\theta_{70}} = 0.9$$

The integrations of f_{70} and f_0 were estimated by a simple mid-point quadrature numerical technique. This resulted in,

$$\int_0^{\tau_0} f_0 d\tau = 1302 \text{ min} \quad \text{and} \quad \int_0^{\tau_{70}} f_{70} d\tau = 1943 \text{ min.}$$

Using these values and the knowledge that the sputter rate for the original unexposed sample is 6 nm/min results in a value of 3.6 nm/min for R_{70} . Following a similar process for the evaluation of R_{30} results in a value of 4.7 nm/min. Using these values for sputter rate, the thicknesses of each sample can be estimated. Concentration-depth profiles using these sputter rates are shown in Figures 42, 43, and 44.

Product Formation Model

The modified TGA provided data on the variation of product mass as a function of time during the product growth process. This data in combination with the concentration-depth profiles of the laminated foil samples can be used to provide insight into the nature of this process. In order to facilitate the comparison of the concentration-depth profiles shown in Figures 42 and 43, the profiles will be defined in terms of four distinct zones. The innermost section (closest to the platinum) is the base iron/iron oxide material which serves as a substrate on which the product forms. This will hereafter be referred to as zone I. The next innermost section, zone II, is the layer of material that constitutes the interface between zone I and the bulk of the product. For the most part, this zone is a product of the sputtering process used in constructing the concentration-depth profile. Zone III which follows this interfacial zone is the relatively thick layer of product. It is within this layer that the only changes in concentration gradients over the 40 minutes of reaction time are found to take place. The final section, zone IV, is the outermost or exterior layer. These zones are depicted graphically in Figure 45.

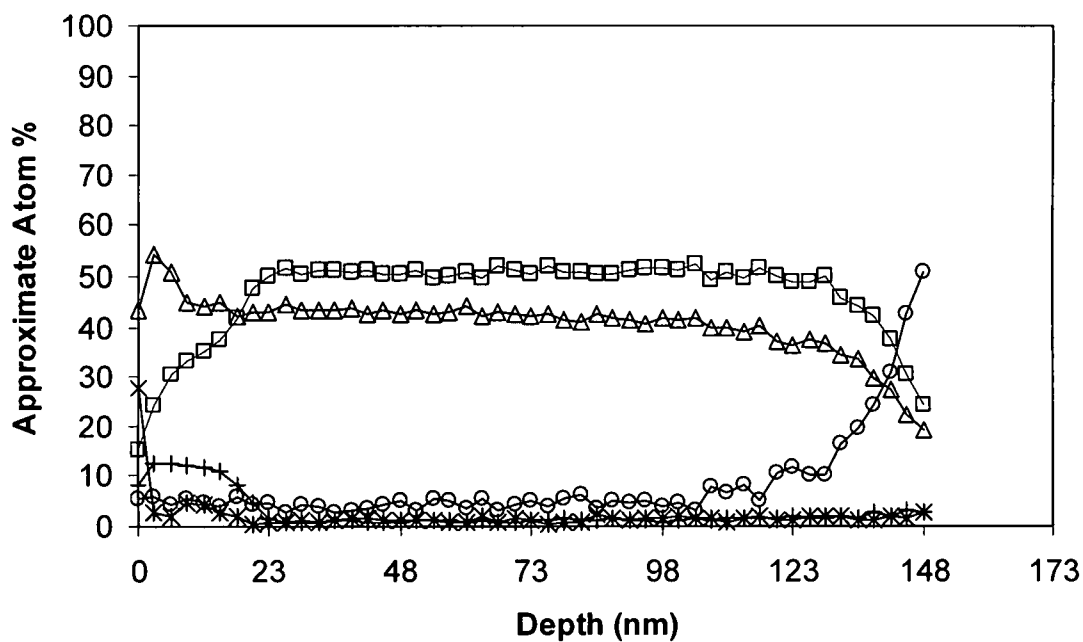


Figure 42. Adjusted concentration-depth profile for a laminated iron/platinum foil after a 30 minute exposure to TBPP vapor in helium, ○ -Platinum, □ -Iron, △-Oxygen, +-Phosphorous, *-Carbon.

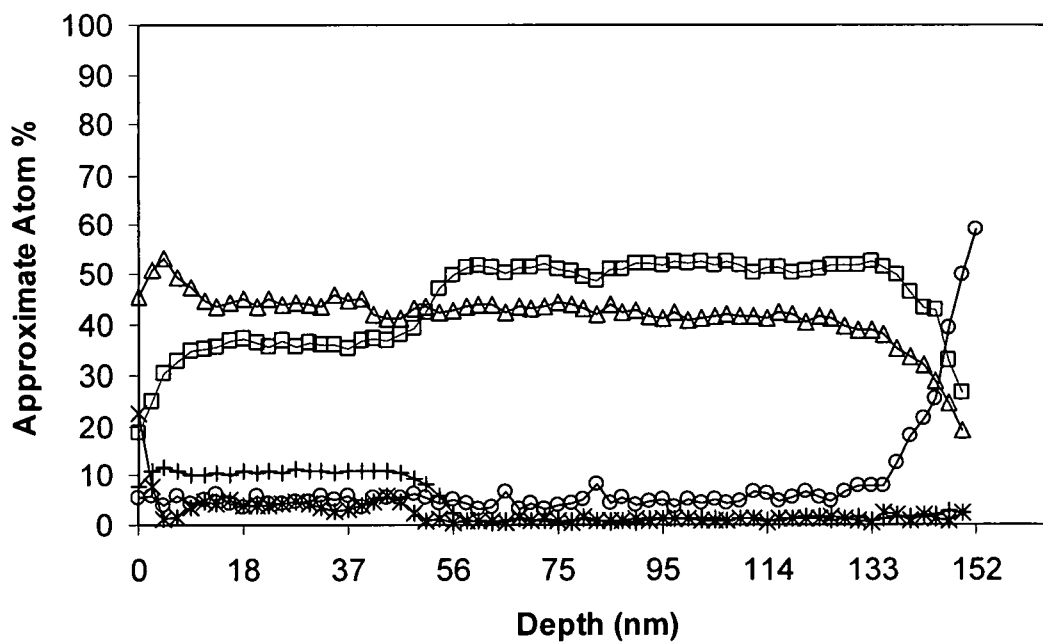


Figure 43. Adjusted concentration-depth profile for a laminated iron/platinum foil after a 70 minute exposure to TBPP vapor in helium, ○ -Platinum, □ -Iron, △ -Oxygen, + -Phosphorous, * -Carbon.

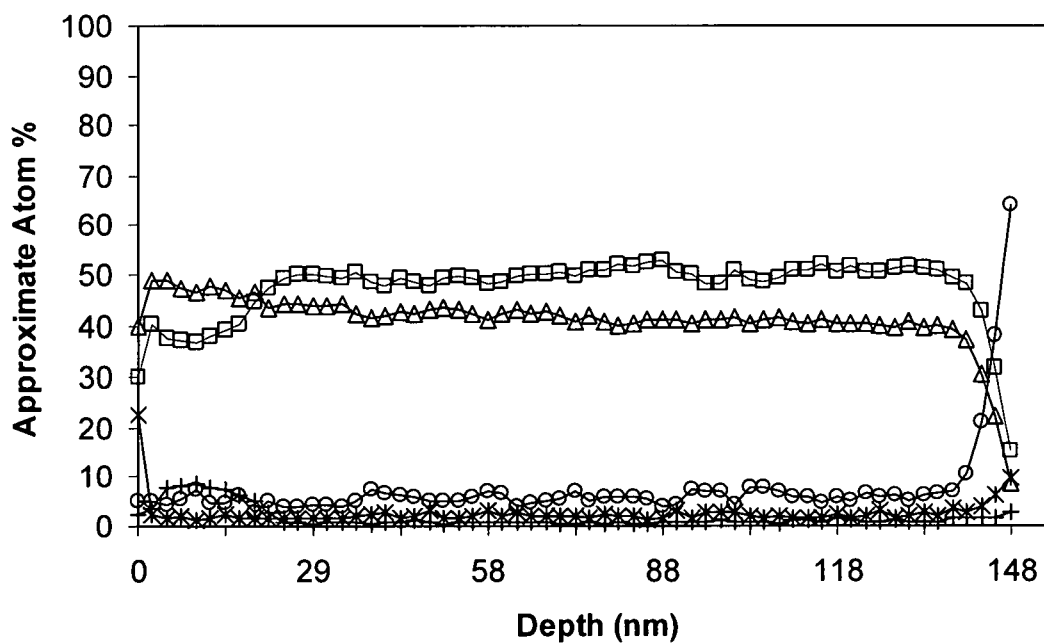


Figure 44. Adjusted concentration-depth profile for a laminated iron/platinum foil after a 70 minute exposure to trace TBPP vapor in helium, ○ -Platinum, □ -Iron, △-Oxygen, +-Phosphorous, * -Carbon.

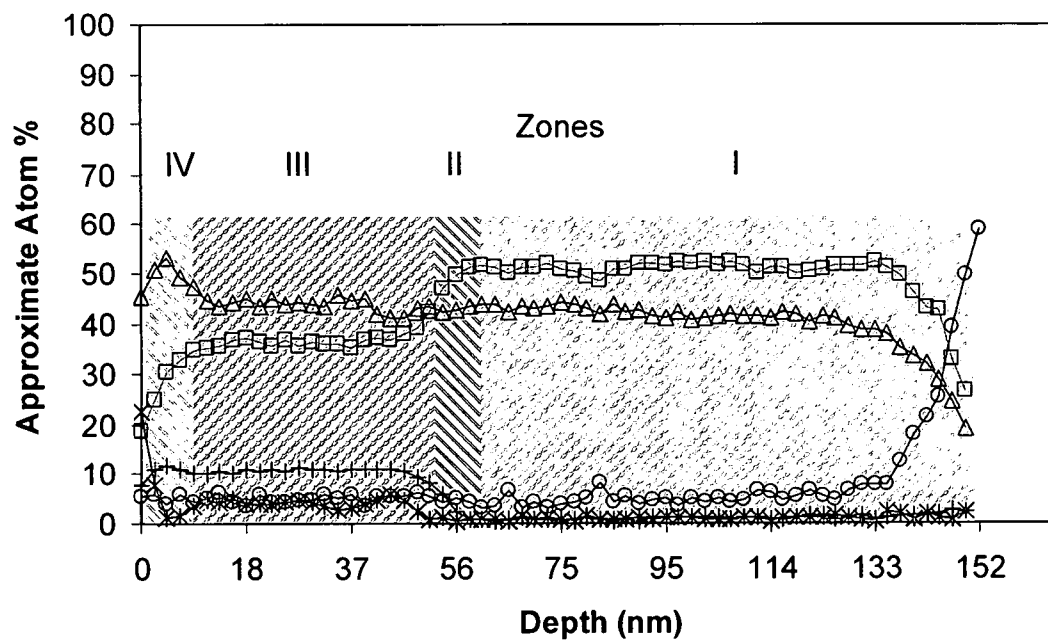
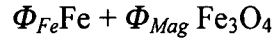


Figure 45. Identification of zones in concentration-depth profile.

At the given concentrations of iron and oxygen shown in Figures 42 and 43, the equilibrium phase mixture is known to be a combination of iron and magnetite. The mole fraction of each can be estimated by using the concentration of iron. If Φ_{Fe} represents the mole fraction of iron and Φ_{Mag} represents the mole fraction of magnetite, then the mixture can be expressed as



then

$$f_{70} = \frac{\phi_{Fe} + 3\phi_{Mag}}{\phi_{Fe} + 7\phi_{Mag}}$$

Since f_{70} is approximately 52 atom %, the mole fraction of iron is calculated to be approximately 60% and subsequently the mole fraction of magnetite is calculated to be approximately 40%. These values translate to volume percents of 20% for the iron and 80% for the magnetite.

A comparison between Figures 42 and 43 shows that the only zone that exhibits any changes during the 40 minutes of product growth is zone III. This zone shows changes in both depth and the gradient of the iron concentration. Moreover, the concentrations of iron on both ends of this zone appear to remain unchanged. This is illustrated in Figure 46. Here the iron concentration-depth profiles for all but zone I of both the 30 and 70 minute samples are shown. In this figure the concentration gradients for the 30 and 70 minute samples are:

$$\frac{C'_{Fe} - C_{Fe}}{L' - L}$$

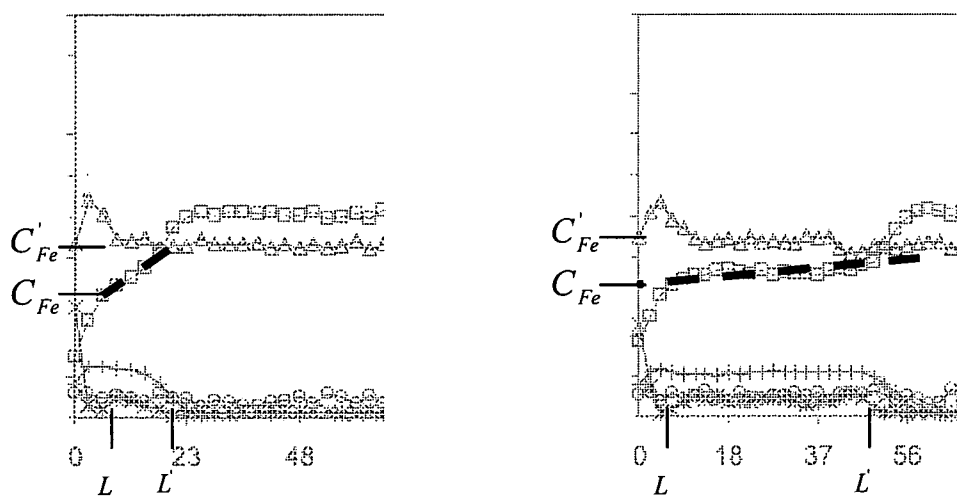


Figure 46. Change in product concentration-depth profiles for 30 (left) and 70 (right) minute samples.

A dashed line is superimposed to highlight the gradient. It is clear from these profiles that the decrease in concentration gradient is due to the increase in the depth of the product ($L'-L$). This type of change in the iron concentration gradient has also been observed in other experiments by Saba and Forester [104]. In these experiments, iron/iron oxide samples were exposed to vaporous tricresyl phosphate at the same 500° C. These samples developed a similar concentration gradient of iron throughout the product which decreased in slope as the iron diffused.

Figure 47 shows a schematic representation of the concentration gradients shown in Figure 46 before and after an amount of time has passed. This representation assumes that these gradients are sufficiently modeled in the linear form shown. As can be seen on the schematic, these two gradient lines in combination with the horizontal line fixed in the position of C_{Fe} and extending from L'_P to L_P form a triangular geometric shape. Here the integrated area of this triangle is one half of the product of the triangle's height ($C'_{Fe} - C_{Fe}$) and width ($L'_P - L_P$). This geometric area is related to the mass of iron that has been added to the product as the iron diffuses through the existent product.

In terms of differential quantities, as the product thickness increases from L to $L+dL$ the increase in the amount of iron can be expressed as

$$dm_{Fe} = \frac{1}{2}(C'_{Fe} - C_{Fe})AM_{Fe}dL$$

m_{Fe} represents the mass of iron, A represents area and M_{Fe} represents the molecular weight of iron.

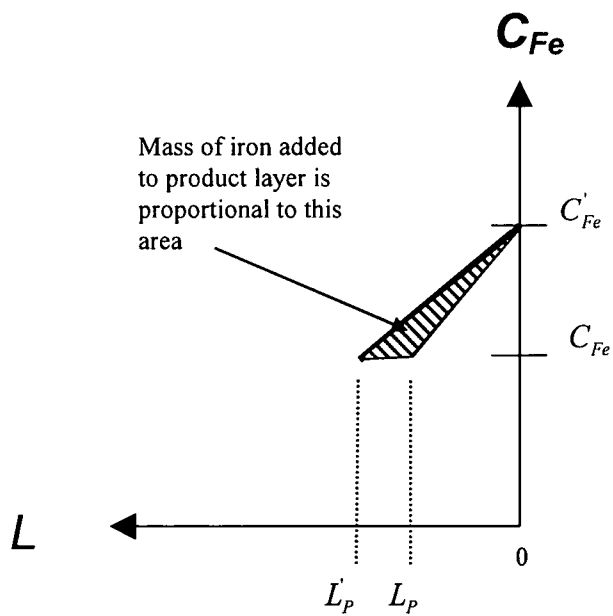


Figure 47. Model of changing concentration-depth profile.

The rate at which this mass of iron in the product increases with respect to time can be expressed as

$$\frac{dm_{Fe}}{dt} = \frac{1}{2}(C'_{Fe} - C_{Fe})AM_{Fe} \frac{dL}{dt}$$

Dividing both sides of this equation by the area, A , results in the following expression for the mass flux of iron through the product layer.

$$\frac{1}{A} \frac{dm_{Fe}}{dt} = \frac{1}{2}(C'_{Fe} - C_{Fe})M_{Fe} \frac{dL}{dt}$$

From Fick's first law and the apparently linear iron concentration profile, the flux of iron can also be expressed as

$$D_{Fe} \frac{(C'_{Fe} - C_{Fe})M_{Fe}}{L}$$

where D_{Fe} represent the diffusivity of the iron. These two expressions for the rate of diffusive transport of iron through the product layer can then be equated as

$$\frac{1}{2}(C'_{Fe} - C_{Fe})M_{Fe} \frac{dL}{dt} = D_{Fe} \frac{(C'_{Fe} - C_{Fe})M_{Fe}}{L} \quad (2)$$

After simplifying and separating variables,

$$\int_{L_p}^{L'_p} L \, dL = 2D_{Fe} \int_{t_0}^t dt$$

Here the integrations are carried out between the two points of interest, from time t_0 when the product layer thickness is L_p and time t when the product layer thickness has increased to L'_p . Performing these integrations results in

$$(L'_p)^2 - (L_p)^2 = 4D_{Fe}(t - t_0)$$

This relation can then be used to estimate the iron diffusivity through zone III. The values for L'_p and L_p from the concentration-depth profiles are found to be 6 and 49 nm respectively. Using these values combined with a value of 40 minutes for the $(t-t_0)$ term results in an iron diffusivity value of $3 \times 10^{-15} \text{ cm}^2/\text{sec}$. This value is greater than iron's self diffusivity ($5.9 \times 10^{-17} \text{ cm}^2/\text{sec}$) and is within the range of values for iron diffusivity found by Forster in dynamic wear experiments at 430° C .

As shown in Equation 2 above with initial values of zero for L and t ,

$$\frac{dL}{dt} \propto \frac{1}{L} \propto \frac{1}{\sqrt{t}}$$

Since the area of each sample and the density of the product do not change significantly with time, the weight of the product W is proportional to L and

$$\frac{dW}{dt} = k_{-1} W^{-1}$$

where k_{-1} is a constant. This is an example of a power-law type of kinetics expression which has the general form,

$$\frac{dW}{dt} = k_n W^n$$

where k is the reaction rate constant and n is a constant which represents the order of the overall product formation process. Here, zero order ($n=0$) indicates that the rate of product formation is independent of the mass of the product formed. Inverse order ($n<0$) indicates that the rate decreases as the product mass increases and a positive order ($n>0$) means that the rate increases as the product mass increases. Other related kinetics expressions outside the realm of power-law forms are exponential functions such as:

$$\frac{dW}{dt} = k_e e^{-\frac{W}{k_e}}$$

here the rate of product formation decreases exponentially as the mass of the product increases. Along with this exponential model, power-law models of zero and inverse orders have been particularly useful in the description of corrosion and oxidation behavior involving solid-gas reactions which generate a solid surface product. In contrast to zero order kinetics the exponential and inverse order type lead to a decrease in the further formation of product by interfering with the reactants being able to contact each other. Product formation only continues as the reactants contact each other by one or more of the reactants migrating through the existing product layer. As the product continues to grow in thickness, the rate at which the product grows continues to decrease.

Separating the variables and integrating the inverse first order kinetic expression of product weight ($n = -1$) with the initial condition that the product layer thickness is zero results in:

$$W = (2k_{-1}t)^{\frac{1}{2}}$$

It is clear from this expression that if the model for product growth described above is legitimate, the product weight will be proportional to the square root of time with an inverse rate constant of k_{-1} . This predicted behavior can be verified by comparing this function with the actual data collected from the modified TGA. However, the weight gain recorded by the modified TGA does not include the weight of the iron that has diffused into the product. Since the concentration-depth profiles have shown that the concentrations of iron at the product layer boundaries do not change, an additional

constant must be included in the above expression for product weight as a function of time. Thus,

$$W = k' (2k_{-1}t)^{\frac{1}{2}}$$

There are also several unique aspects of the initial conditions that must be considered prior to making such a comparison with the collected data. As described earlier, the initial product formation on the iron and steel substrates could not be determined using the modified TGA equipment. Although the product begins to form at the moment the TBPP vapor contacts the solid surface, the equipment did not reach steady state operation until after an initial 10 minute start-up period. In this case the actual initial product formation rate can only be estimated by extrapolation. This is quite different from the situation involving the iron/platinum laminated foil. Since the initial measurable product formation on the iron/platinum foil substrates did not occur until after the first 30 minutes of operation, the initial product prior to this point can be assumed to be zero.

With these considerations in mind, standard linear regression was used in comparing the TGA data with the kinetic description shown above. The weight data taken from the experiments with the iron/platinum laminated foil was found to be proportional to $t^{1/2}$ with a correlation coefficient of 0.9392. Similarly high correlation coefficients were found for the data taken from the experiments using pure iron in nitrogen and helium carrier gases at the same temperature. In this case, the correlation coefficient for the fit is 0.9967 and 0.9963 respectively. Tables 5 and 6 show the correlation coefficients that result from this same type of least squares fit applied to the other data. In these tables, the

Table 5. Model correlation coefficients for TBPP vapor/helium reaction on iron.

	Linear (n=0) Model	Parabolic (n=-1) Model	Logarithmic (n=1) Model
300° C	0.6046	0.7173	0.8292
400° C	0.9890	0.9959	0.9554
500° C	0.9644	0.9963	0.9889
600° C	0.9451	0.9945	0.9778

Table 6. Model correlation coefficients for TBPP vapor/nitrogen reaction on iron.

	Linear (n=0) Model	Parabolic (n=-1) Model	Logarithmic (n=1) Model
300° C	0.8569	0.9336	0.9819
400° C	0.9379	0.9865	0.9957
500° C	0.9644	0.9963	0.9889
600° C	0.9451	0.9945	0.9778

term “linear” refers to the zero-order kinetic model while the terms “parabolic” and “logarithmic” refer to the non-linear models described earlier.

The function used in this curve fitting process was of the form,

$$W = B\sqrt{t}$$

where B is a fit constant. This constant is then found to be proportional to the square root of the rate constant. This relationship and the temperature dependence of this rate constant can then be expressed as

$$k_{-1} = \frac{1}{2} \left(\frac{B}{k'} \right)^2 = \alpha e^{-\frac{Q}{RT}}.$$

This can be rearranged as

$$B^2 = (k')^2 2\alpha e^{-\frac{Q}{RT}}.$$

Taking the logarithm of each side of this equation results in

$$\ln B = \ln k'' - \frac{Q}{2RT}$$

where

$$k'' = k' \sqrt{2\alpha}$$

The slope of the line resulting from a least squares fit of the logarithm of B as a function of inverse absolute temperature (T) provides the activation energy Q . The fit factor B was determined for all iron samples in both nitrogen and helium carrier gases for temperatures from 300° to 600° C. This plot is displayed in Figure 48. The correlation coefficient for this regression was found to be 0.8534. From this the activation energy for the product growth process was calculated to be 34 Kcal/mole.

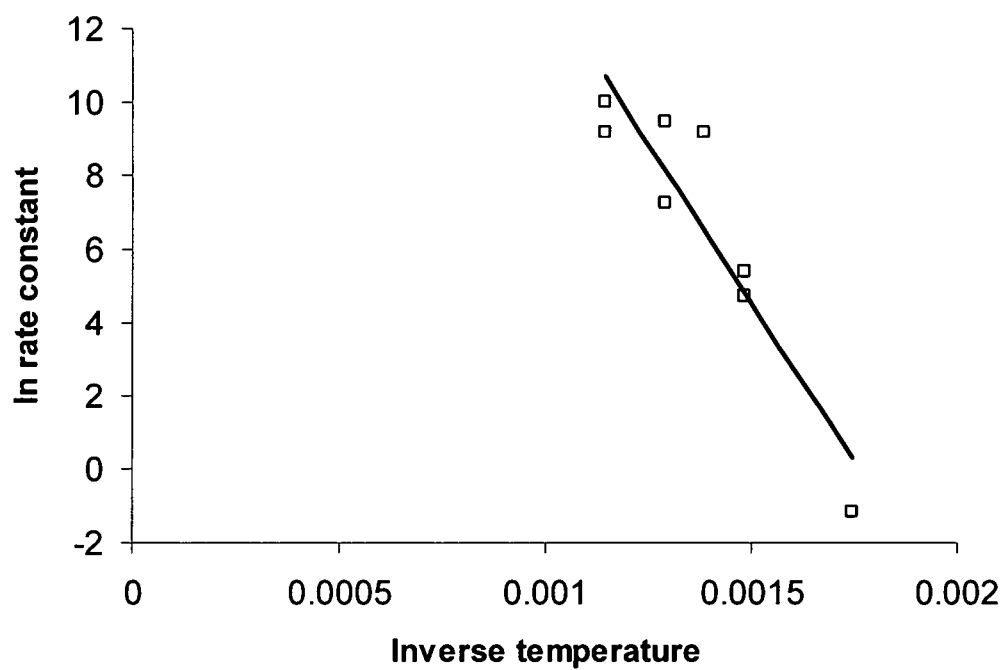


Figure 48. Arrhenius plot of product growth rate constant.

Since the diffusion of the iron appears to be the rate controlling step, this activation energy is interpreted as being that of the diffusion process. Maki and Graham [68] reported a chemical reaction activation energy for the reaction between ferrous surfaces and tricreyl phosphate of 13.85 Kcal/mole. The activation energy involved in the reaction with TBPP is likely very close to this value which is substantially lower than that associated with diffusion. Solid state diffusion processes which display such large activation energies are characterized by vacancy diffusion as opposed to interstitial processes.

CHAPTER IV

DISCUSSION

Proper interpretation of the experimental results described in the previous section provides insight into the role that diffusion plays in the generation of surface product. This insight does not come in the form of unequivocal answers to the many questions regarding this role but rather in the form of deductions drawn from the indirect evidence provided by the experimental work. In this section, these deductions and the reasoning behind these deductions are described.

Equipment

Previous work investigating the reaction between triaryl phosphate esters and ferrous surfaces have involved the measurement of product formation by removing samples from a heated reaction chamber followed by the re-weighing of each sample after cooling to room-temperature. The use of this type of process can lead to the potential inaccuracies associated with handling the sample prior to re-weighing and in particular to the loss of sample via detachment from the substrate during cooling. The modified TGA used in this work provides a nearly continuous recording of product weight as a function of time without the need to remove the sample from the reaction environment or handle the sample in any way for weighing purposes. This facilitates the accurate determination of

how the product weight changes with reaction time which in turn facilitates the accurate determination of specific rate law constants. However, the use of this equipment cannot provide useful information on the variation of product weight with time during the first several minutes of the process prior to reaching steady state operating conditions. This includes any initial reaction with trace oxygen in the carrier gas and the formation of an initial layer of product. In this way, a high degree of fidelity in measuring reaction rates is achieved at the expense of losing information related to the initial process of product formation. This is deemed to be acceptable since the objective of this work is to gain a greater understanding of the processes in operation after an initial surface product has formed.

Carrier Gases

Each experiment exposing iron to TBPP vapor was arranged to focus exclusively on the interaction that takes place between the TBPP vapor and the reaction product that continuously forms during these exposures. For this reason, the carrier gas used in each experiment was intended to transport the TBPP vapor to the solid surface and remain inert relative to both the surface and the vapor. Much of the work previously performed by other researchers exploring the initial reaction between various solid surfaces and TCP vapor has been performed with this same intent and for this reason has employed nitrogen as the carrier gas. Nitrogen was also used in the initial experiments of this work to establish that the modified TGA equipment produced results comparable to those found by these other researchers.

In the gaseous state, nitrogen remains un-reactive with TBPP vapor at the temperatures used in this work. However, diatomic nitrogen is known to adsorb and dissociate on ferrous surfaces and then absorb into these surfaces at high temperatures leading to the formation of a solid solution where monatomic nitrogen serves as the solute. When present in adequate quantities, iron nitride compounds including Fe_2N and Fe_4N are formed [105-109]. This dissociative adsorption of nitrogen on iron is in fact the basis for the use of iron as a catalyst in the high temperature synthesis of ammonia from feed stocks of diatomic nitrogen and hydrogen gases referred to as the Haber process [110]. The temperature range typically utilized for this synthesis reaction is between 450° and 500° C. The characteristic gray color of these iron nitride compounds was observed on the surfaces of the ferrous samples exposed to nitrogen at both 500° and 600° C but was absent from the samples exposed to helium at those same temperatures.

Helium was used in place of the nitrogen as the carrier gas in some of the iron and in all of the iron/platinum laminated foil experiments in order to ensure that no reaction between iron and dissociated nitrogen would take place and subsequently interfere with the formation of the product. This interference by nitrogen is demonstrated by the observed difference in reaction rate at the higher temperatures used in this work. This is displayed in Figure 49. Here the product quantity formed on iron after 60 minutes of exposure to TBPP vapor, expressed in units of $\mu\text{g}/\text{cm}^2$, is shown plotted as a function of temperature. As can be seen in the figure, the amount of product formed in nitrogen deviates from that which was formed in helium to an increasing degree as the temperature approaches 600° C. A similar effect of nitrogen was reported in earlier work by Ma et al. [64] where iron oxide in the form of an "oxy-nitrided" surface film actually promoted the

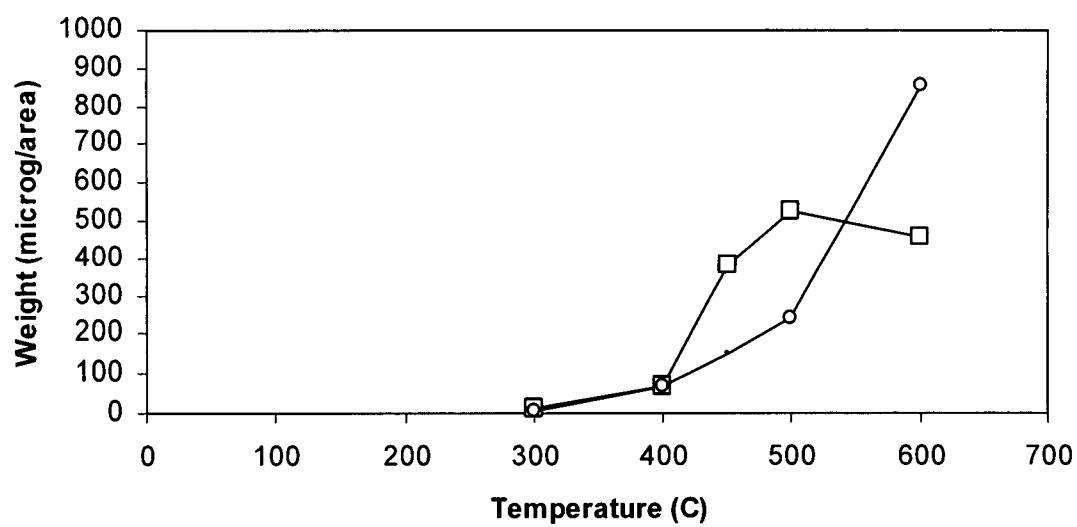


Figure 49. Extent of reaction in nitrogen (\square) and helium (\circ) carrier gases.

surface reaction with TCP in the liquid phase. Previous work by various researchers using nitrogen as a carrier gas and an iron substrate have attempted to limit the time during which the iron is exposed at high temperatures to the nitrogen carrier gas alone. However, in these efforts, it would have been impossible to avoid all possible exposure of the metal to nitrogen at high temperature. Thus, all experiments utilizing nitrogen would have been affected to some extent and this would have had some effect on the experimental results, albeit limited.

Unlike nitrogen, helium does not exhibit a solubility in metals to any great extent below the melting point of the metal and also unlike nitrogen, helium is not expected to form compounds. Although the helium was expected to remain inert, any oxygen that is present as contamination would not. Even though each carrier gas was filtered by moisture and oxygen traps, a number of potential sources for air leakage into the system, down-stream of these traps, may have contributed to the existent oxygen contamination in each carrier gas. As shown in Figures 14 through 16, the oxidation of the metal substrates can be substantial. However, it was found that iron samples exposed to TBPP vapor very quickly develop a reaction product that impedes any further interaction with the carrier gas and its oxygen contaminant. Therefore, except for the initial few minutes of operation (while the system approaches steady state), any weight gain due to oxidation by contaminant oxygen during the reaction with TBPP vapor has been considered negligible. This ability to quickly cover a ferrous surface with product is not surprising since previous work has shown that other organophosphates including TCP will react with iron at temperatures less than 200° C to form iron phosphate surface products [17, 65].

Sample Constituents

The surfaces of all metallic samples with the exception of the laminated iron/platinum foils used in these experiments possessed at least to some extent an adsorbed layer of carbon which was likely the result of being cleaned with acetone prior to use.

Adventitious sources also likely contributed to this surface carbon.

All samples used in these experiments were also exposed to oxygen to varying degrees and from a variety of sources other than the carrier gas. In each experiment, the temperatures were initially set with the furnace in the closed position without a sample in place. Following this, each sample was loaded, the furnace closed once again, and the system was allowed to purge for 60 minutes before the furnace was energized. During this purge each sample was exposed to heated carrier gas and an ever decreasing amount of outside air. Additionally, each experiment ended by removing each sample from the furnace while still hot which resulted in the exposure of each heated sample to room air for the purpose of cooling.

These exposures to oxygen are key to explaining the various colors that appeared on the ferrous surfaces during exposure to the heated carrier gases. The exposure of these heated ferrous surfaces to such sources of oxygen would have generated iron oxide at the surfaces of each of the ferrous samples. This would have been followed by the exposure to air during the sample removal process. The exposure to air could have facilitated the generation of a surface layer of oxide in the form of hematite (Fe_2O_3). While the underlying iron and any magnetite would be opaque to visible light, the hematite would not. The combination of a hematite layer on the surface of an opaque substrate would act

as a source for the iridescent reflection of light. This is characterized by the selective interference of particular wavelengths depending on the refractive index and thickness of the hematite layer. In this way, the extinction by destructive interference of the energy with wavelengths at the high end of the visible light spectrum would leave only those at the low end of the spectrum unaffected and the sample would appear blue in color. This mechanism is likely responsible for the display of the yellow, blue, and green colors as described previously. This is the same mechanism that is known to be responsible for the appearance of color during the tempering of steel between the temperatures of 200° and 350° C. Iridescent “pigments” also utilize this same mechanism for the generation of color.

The exposure of the iron/platinum laminated foil samples to air during cooling is also likely responsible for the greatly increased oxygen concentration within the first approximately 10 nm of the exterior surface (zone IV) of the iron layer. The iridescence mechanism may be responsible for a portion of the color displayed by the iron/platinum laminated foil samples that were coated with the variety of materials that were found on their surfaces. However, in this case the color is also likely influenced by the light absorption properties of any existent product. For example, the iron phosphate mineral Vivianite ($\text{Fe}_3(\text{PO}_4)_2 \cdot 8(\text{H}_2\text{O})$) exhibits a natural blue tint.

As shown in Figure 37, the laminated foil samples also contained oxygen that was distributed throughout the bulk of the iron layer as opposed to being localized near the exterior surface prior to any heating. The oxygen residing within the bulk of the unexposed samples was likely trapped or otherwise incorporated into the iron layer as the iron was deposited onto the platinum substrate by PVD (Physical Vapor Deposition) at

room temperature. The vacuum chamber used for this deposition was equipped with a turbomolecular pump backed by an oil sealed sliding vane pump with a base pressure between 0.1 and 1.0 mm Hg. Chamber pressure during the deposition was 500 mm Hg. A small leak was later found in the vacuum chamber which was determined to be responsible for this relatively high chamber base pressure which likely led to the trapping of oxygen within the deposited film.

At room temperature, oxygen (as opposed to the nitrogen) would be preferentially incorporated into the iron layer due to its high degree of reactivity with iron. This same level of base pressure has been reported to have led to the incorporation of oxygen in titanium during the PVD of titanium onto platinum substrates [111]. This reporting of gas being incorporated into a deposited metal layer during PVD is not altogether uncommon. This is especially true of ion implantation and sputtering processes using noble gases. The incorporation of such a gas during PVD can embrittle the substrate or precipitate within the substrate material in the form of high localized concentrations or pockets [112-114]. Gases which are chemisorbed by a particular substrate are especially vulnerable to being trapped [115] as would be the case for oxygen chemisorption on iron. The exact chemical state of this oxygen within the iron layer is unknown. A small portion of the oxygen may have been present in the form of water vapor, a diatomic related complex such as a dioxide, peroxide, or super-oxide, etc., or an oxygen cluster such as a dimer or trimer anion [116-118].

As shown in Table 4, the Fe_{LMM} Auger electron energies are constant throughout the depth of the iron layer except for the outer surface while the O_{KLL} Auger electron energies are constant throughout the layer including the outer surface. This implies that the source

and form of the contaminant oxygen remained unchanged throughout the entire deposition process. As can be seen in Table 3, these energy values change substantially after the initial 30 minutes of heating and exposure to TBPP vapor indicating that a change in chemistry has taken place throughout the iron layer during this 30 minute time period. This is also observed in the 70 minute sample as shown in Table 4.

The concentration profiles of the elements within the iron layer prior to heating, as shown in Figure 37, also display apparent concentration gradients in both iron and oxygen. A comparison of the average concentrations in the unheated sample displayed in Figure 37 with the average concentrations in the exposed sample shown in Figure 38 shows that the concentration of the iron after the initial 30 minute exposure is approximately 20 percent less than the concentration in the bulk of the unheated/unexposed sample. Corresponding to this, the concentration of the oxygen appears to rise by this same amount. This is also seen in comparisons with the samples exposed to different gas phases for 70 minute time periods shown in Figures 39 and 40. Since there is no route by which iron could have been lost from the bulk of the sample, this change in concentration must be related to a change in the oxygen content alone. Since these same changes in concentrations were observed in all but the unexposed sample, this additional oxidation must be a process common to all samples that were heated in the modified TGA. Two sources of this additional oxygen are readily apparent. One source is the trace contaminant oxygen in the carrier gases. Even though the flow of carrier gas was directed through an oxygen trap to lower the concentration of oxygen to less than 1 part per billion, traces of oxygen could have entered the flow through unidentified leaks in the system during each experiment. These leak paths include the

septum and other points in the TGA system. Iron is very reactive with even small traces of oxygen. At 500° C the continued oxidation of iron oxide is thermodynamically favored at oxygen partial pressures far less than 10^{-9} atmospheres. Therefore, it is likely that some amount of extended oxidation occurred during each experiment. Since the same degree of oxidation is implied by the consistency of the concentrations found in zone I of each sample, the process involved must be identical to each experiment. This is true for both the 30 minute and 70 minute samples. Since it has been shown that the development of a small amount of surface product essentially seals the exterior surface from further oxidation, this additional oxygen must be part of a process that takes place before the formation of a product layer begins. This process begins with the 60 minute furnace purge that was common to each TGA experiment. In this portion of each experiment the sample was loaded into the furnace and the furnace sealed. Each sample was held within the furnace for 60 minutes during which time the furnace was purged with heated carrier gas to flush out the air that remained in the furnace chamber. Even though the furnace was not yet switched on, each sample was exposed to an ever-declining concentration of air in addition to the trace oxygen contamination in the carrier gas.

During the initial 30 minutes of exposure to the 500° C test temperature, the oxygen and iron within the layer interact and move toward the establishment of a homogeneous equilibrium distribution. This is evidenced by the elimination of the apparent oxygen and iron concentration gradients and the large shift in the Auger electron energies of these elements during this initial 30 minute time period. Additionally, the Fe_{LMM} and O_{KLL} Auger electron energies appear to remain constant within the bulk of the iron layer after

30 minutes indicating that the majority of the chemical changes take place in this layer during this 30 minute time period. Although the fact that the Fe_{LMM} and O_{KLL} Auger electron energies do not change does not in itself serve as a proof of equilibrium since these energies can have similar values when present in different forms of iron oxide [120, 121], this is an indication that the iron and oxygen within this layer are near to chemical equilibrium.

At the test temperature of 500° C, the equilibrium form of this mixture of oxygen and iron is a two phase combination of α -iron and magnetite (Fe_3O_4). In this case the α -iron consists of a body centered cubic arrangement of iron atoms while the magnetite consists of a spinel arrangement of oxygen anions with iron cations of mixed oxidation state occupying certain interstitial sites [122]. A comparison of Figures 33 and 34 also shows that the overall volume of the iron layer increases during the initial 30 minutes of exposure which can be attributed to the increased oxygen content of this layer as explained earlier. Since one side (face) of the iron portion of the iron/platinum laminated foil is physically restricted from expanding in directions normal to the edges, the incorporation of this oxygen will generate a stress in this layer that is normal to the face of the material. This will have had the effect of elongating the grains of oxide as the oxide is generated in a direction parallel to the edges of the foil.

The incorporation of oxygen and the reactions indicated by the changes in Fe_{LMM} Auger electron energies also leads to a change in the sputter rate of the material. The formation of oxygen-iron bonding and crystallization during the initial heating of the iron/platinum laminated foil is manifested by an increase in inter-atomic bond strength.

This increased bond strength will lead to a decrease in sputter yield. This decreased sputter yield is reflected in the decrease sputter rate as shown in Chapter 3.

After this initial 30 minutes the concentrations of the elements correspond to a mixture of approximately 35 mole percent magnetite and 65 mole percent α -iron.

Product Constituents

The reaction of the TBPP vapor with the ferrous surfaces used in this work yielded a solid product of the same color as that reported by others that were generated by the reaction between vaporous TCP and iron at 700° C [78]. The product did however detach from the surface to varying degrees on both the iron and iron/platinum laminated substrate materials and in doing so exposed what appeared to be a clean metal surface underneath. This detachment of the product became more prominent for the products formed at higher reaction temperatures. This product detachment is similar to that which was described by Graham and Klaus [10] in which case the surface product was formed on M50 steel at 600° C during a 5 minute exposure to a 1.2 percent concentration of vaporous di-*t*-butyl phenyl phosphate and di-phenyl phosphate in a nitrogen carrier gas. FTIR scans of the metal surfaces beneath the detached product exhibited only minor variations in IR absorption beyond that of a clean metal surface indicating the presence of very little organic material. This implies that the product detachment most likely occurred during the cooling process and not during the process of product generation. This is also an indication that an interface characterized by steep gradients in the concentrations of the product and metal are likely present at the location where the product separates from the substrate metal surface. This type of surface detachment is

also characteristic of a significant difference in the extent to which the product contracts as compared to the contraction of the metal during cooling.

Product also detached from the surfaces of the iron/platinum laminated foil samples but to a much lower extent. This is likely the result of the unique combination of materials each with different linear thermal expansion coefficients. As can be seen in Table 7, the coefficient of linear thermal expansion (α_T) for both iron and magnetite are larger than that of platinum. On cooling, since the platinum substrate has a lower α_T than either that of the iron or magnetite which are attached to the platinum, a tensile stress in the iron/magnetite layer would result. In this situation, the iron/magnetite mixture would contract to a lesser extent than would pure iron experiencing the same temperature changes. This would result in a somewhat reduced stress in the product layer on the iron/platinum laminated material as compared to the amount of stress that would be generated in a product layer formed on a pure iron substrate. The extent to which this reduction in stress took place may have been somewhat moderated by the tendency for the laminated foil sample to take on a slightly concave shape, thereby relieving a portion of the stress. This was also likely moderated by the previously generated compressive stress due to the incorporation of additional oxygen.

The FTIR examination of the exterior surface of the product was not considered to be particularly useful since during the cooling process the samples were exposed to air and small amounts of TBPP vapor, some of which could have condensed on the exterior surface of the product. Some of this condensate could also partially react with the surface during the cooling process. This would have resulted in changes to the product

Table 7. Thermal expansion properties of selected materials.

Material	α_T (at 500° C)
Platinum	$9.6 \times 10^{-6} / ^\circ\text{C}$
Iron [†]	$14.2 \times 10^{-6} / ^\circ\text{C}$
Magnetite [†] [119]	$17 \times 10^{-6} / ^\circ\text{C}$

[†] Interpolated from chart data

surface which would have masked the true chemical composition of the surface resulting exclusively from the process of product formation just prior to cooling.

For this reason, FTIR spectroscopy was only used to examine the interior surface of the product (the surface of the product which was formerly attached to the metal) and the surface of the metal from which the product detached. EDS was used to examine the product in the configuration where it was still attached to the metal surface.

The combined EDS and FTIR analyses indicate that the product was composed principally of a phosphatic material with the addition of a small amount of carbon. The relatively large width of the IR absorption bands is characteristic of a product composed of a variety of phosphate type compounds and is consistent with most past work using vaporous TBPP and TCP reactants on ferrous surfaces.

The experiments with the iron/platinum laminated samples also showed that the concentrations of the elements within the product are consistent with the product that is formed by the reactions between ferrous surfaces and TCP and TBPP under a variety of conditions as reported in many other works.

Product Formation

Although the weight of the product associated with the start-up and initial 30 minutes of the laminated foil exposure to TBPP vapor could not be ascertained, the small volume occupied by this product (as determined by the known dimensions of the product) implies a weight that is infinitesimal. No product growth (discernable by weight) took place until after this initial 30 minutes of exposure. This delay in product growth is quite different from that which occurred on the surface of plain iron foil under the same

conditions. The lack of reactivity during the initial 30 minutes of exposure is likely due to the processes by which the oxygen (incorporated during the PVD and during the purge process) and iron are changing and moving toward the establishment of an equilibrium distribution throughout the layer. These processes would include both chemical reaction and diffusive movement. Additionally, the rate of product formation on the iron/platinum laminated foil is much lower than the rate of formation on a bulk iron surface. For both the iron and laminated foils, the surfaces are in an oxidized state prior to exposure to TBPP vapor.

Previous work by Klaus et al. [125] has shown that iron oxide is very quickly reduced to phosphorous containing product when the oxide is exposed to high temperature TCP vapor. In keeping with this finding, Saba and Forster [104] have demonstrated that oxidized iron reacts with TBPP vapor at a higher rate than pure iron at 475° C. There is no doubt that this same initial reduction of the iron oxide takes place on the initial exposure of the iron and iron/platinum laminated foils used in this work. However, the continuation of product growth appears to only continue as long as un-oxidized iron is also present. The oxide that typically appears on the exterior of an iron foil is characterized by a gradient in iron concentration with the concentration increasing with the depth into the foil. When the bulk of this surface oxide is reduced, the underlying un-oxidized iron is exposed to the phosphorous product resulting from the reduction. In the case of the iron/platinum laminated foils, the amount of underlying iron is very small, i.e. between 10 and 20 percent by volume, and the overall reaction rate is correspondingly small. This then provides an explanation for the great disparity in the overall reaction rates observed with the iron foils compared to the iron/platinum laminated foils. The

evidence for this explanation is found through an examination of the concentration-depth profiles of the iron/platinum laminated foil. The changes in the concentration-depth profiles between the 30 and 70 minute samples are significant (see Figures 42 and 43). The material within the product formed by reaction with the TBPP vapor during 70 minutes of exposure consists of the same elements as that of the 30 minute sample. A comparison of the product formed on the 30 minute sample with that formed on the 70 minute sample demonstrates that for the most part the bulk of the product occupies space that was previously occupied by the substrate (zone I).

This indicates that either reactant is moving across the interface (zone II) from the product or gas phase into the iron (zone I) where reactions take place to form more product, or iron is moving across zone II from the iron (zone I) to react with the product or continue to move to the exterior of the product to react with the vapor forming more product.

Clearly the vaporous TBPP is not being absorbed in toto by the existent product and then diffusing through the product to react with the iron in zone II. The phosphorous, oxygen, and carbon that appear in the product must have come from the TBPP vapor. Since their proportion is very different from their proportion in the TBPP, it is clear that the TBPP molecules decompose at the surface of the product. The FTIR spectra of the product shows the oxygen to be covalently bonded to the phosphorous within the bulk of the product as a phosphate type of material. This has also been shown to be the case for the surface product resulting from the reaction between phosphate esters TCP, TBPP, and iron. The sheer size of the molecule would sterically hinder such movement. This also argues against any suggestion that the phosphate ion diffuses through the product.

Although phosphorous is known to be able to occupy iron vacancies, the diffusion of phosphorous through the product would be expected to result in a large concentration gradient in phosphorous throughout the product. Additionally, the diffusion of phosphorous through the iron phase would be expected to result in the generation of little iron phosphate and polyphosphate. In contrast to this, the iron exhibits a large concentration gradient in the product layer that decreases commensurate with a decrease in reaction rate. This leads to the conclusion that iron leaves the iron phase at the interface between the iron and the product (zone II) and moves through the product to the exterior where it reacts with TBPP vapor forming additional product.

This of course requires the generation of iron vacancies at the exterior of the product that move in opposition to the iron. Evidence for this can be found in observing that only the concentration-depth profiles that show a slight amount of platinum diffusion into the iron phase are those that were generating product. The interface between the iron and platinum was used as a reference datum against which the movement of elements could be observed. This interface was defined as the location at which the platinum had a concentration of 50 mole percent. During the exposure of the composite material to high temperatures, some inter-diffusion of these elements would be expected. However, at 500° C, the inter-diffusion of iron and platinum would not be significant during a 70 minute time period and is therefore not considered to have any significant effect on the use of this interface as a reference plane. The un-symmetric diffusion of platinum into the iron phase is due to the over abundance of iron vacancies which was subsequently due to the flow of iron vacancies through the product and substrate (see Figures 38-40). This implies that iron vacancies are moving in the direction of the interface opposed to the iron

concentration gradient and that a few of these vacancies are eventually occupied by platinum.

The product moves in concert with this process to occupy space left by iron vacancies remaining at the exterior of the iron phase. Although the actual viscous properties of this product are not known, most of the phosphate glasses reported in literature display a glass transition temperature far below the 500° C test temperature used here. This is especially true of mixed phase phosphate glasses. This process is also evidenced by the changes in the P_{LMM} Auger electron energies. The energies of the phosphorous electrons at the interface with the iron phase of zone I remain constant, i.e. independent of the depth. This implies that the chemistry of the product formed at the beginning of the process remains intact and that the product moves into the depth of the substrate material as additional product is being formed. This overall process slows as further product is generated due a decrease in the iron's concentration gradient and the subsequent decrease in the flux of the iron.

The AES depth-profile analyses of the product formed on the laminated samples were consistent with the EDS and FTIR analyses of the product formed on pure iron in that the elements iron, oxygen, phosphorous, and carbon were found to be the constituent elements. Additionally, the overall density of the material within the product layer formed on the laminated foil sample was estimated to be approximately 5.5 g/cm³. This value was calculated using the apparent surface area of the sample, the depth of the product layer as revealed by the depth-profiling, and the known weight of the product. As can be seen in Table 8, this density value is very close to, but higher than, that of

Table 8. Densities of selected iron compounds.

Material	Density (g/cm ³)
Fe	7.87
Fe ₃ P	6.74
Fe ₂ P	6.56
FeP	6.07
Fe ₃ O ₄	5.18
FePO ₄ 2H ₂ O	2.74
Fe ₃ (PO ₄) ₂ 8H ₂ O	2.58

magnetite. This is what would be expected for a compound that consisted mainly of magnetite along with a small amount of phosphorous-based material.

The energies of these Auger electrons throughout the product of the 70 minute sample show a continuous shift through the depth of the product to lower values from the 116.25 eV value at the product/metal interface to the 110.00 eV value found at the exterior surface of the sample. The consistency of the P_{LMM} energy at the product/metal interface for both of the samples (30 and 70 minute) also suggests that this shift in P_{LMM} energies is not due to a sputter-induced reduction of the phosphorous but is rather an indication that the product which first forms on the iron layer remains intact while a reaction product with a different chemistry continuously builds on the external surface. The shift to higher P_{LMM} energies throughout the product is characteristic of the difference in P_{LMM} energies found between the phosphate and a phosphide form of compounds with iron [59, 123].

This change in energy is accompanied by a broadening of the associated Auger peak which appears to be a combination of a low energy phosphate peak at around 111 eV and high energy phosphide peak at about 116 eV. This is consistent with a structure in which the exterior of the layer consists of phosphorous principally in the form of a phosphate while the interior consists of a combination of phosphate and phosphide. This is a similar form and position for the phosphorous as proposed by Klaus et al. [33] for the product formed by TCP vapors reacting with iron at 700° C. This trend in changing P_{LMM} energies throughout the product is unlike the trend found for the energies of the iron and oxygen Auger electrons. Within the product layer the Fe_{LMM} and O_{KLL} energies appear

to remain constant at 650.00 and 511.25 eV respectively. These changes in Auger energies are consistent with the previous explanation for product formation. The concentration of oxygen in the bulk of the iron layer does not change significantly as the product forms. This indicates that the oxygen that appears in the product is present in approximately the same proportions as that of the magnetite and is supplied by the TBPP vapor which in turn indicates that the chemical reactions taking place at the surface must include, to a great extent, the breaking of the C-O bonds of the TBPP molecule. The low concentration of carbon in the product also points to the TBPP molecule losing carbon in this way.

The element that exhibits the lowest concentration throughout the product and interfacial region is carbon. In all samples the relatively high concentration of carbon within the initial 6 nm of depth is attributed to the exposure of the sample to ambient air at room temperature. This is very different from the concentration profile for carbon as exhibited in the work by Forster [79]. This is a clear indication that one or more mechanisms associated with the dynamic conditions of rolling contacts and wear are responsible for the build up of such high concentrations of surface carbon.

It is clear that both chemical reaction(s) and the movement of elements are both involved in the overall process of surface product generation. Each of these steps are potentially responsible for setting the pace at which this product is generated. The experimental results provide insight into the mechanism(s) involved and which of the steps may be the slowest and thus responsible for controlling the over all rate.

Figures 21 and 22 show the extent to which surface product forms on iron phosphate powder that has been exposed to vaporous TBPP at 400° and 500° C. Since the iron

phosphate was in a powdered form, its surface area was several orders of magnitude greater than that of the metal samples. The dimensions of the sample pan holding the powder sample, the weight of the iron phosphate hydrate, and the approximate diameter of the individual crystals of phosphate are known. Assuming the powder samples to be a loosely packed bed of particles, the total surface areas of the two samples would have been on the order of 700 and 1,400 cm². Thus, the rate of product formation per apparent surface area at both temperatures is negligible. In addition, the exhibited functional form of the reaction rate is very different from that associated with the product formed on iron. This is evidence that in order for the product to form at the rate seen on iron, iron must not be depleted from the surface as further surface product forms. The product formation process requires a source of iron in addition to that which is bound to phosphorous and oxygen as in the form of a phosphate. In this way the rate of product formation is coupled directly to the mechanism by which iron is made available to the surface of the product.

In each experiment, the concentration of the vaporous TBPP remained constant as did the concentrations of elements in the products on the exterior surface. Under these circumstances, if the chemical reactions taking place on the exterior surface of the product were controlling the rate of the process, the rate would not change with time. Since in all cases the product formation rate decreases with exposure time, the rate controlling step of the overall process cannot be the reaction(s) taking place on the exterior surface of the product.

Iron is transported from the surface of the iron phase of the substrate through a product layer, and then through an exterior region where it reacts with TBPP vapor to form additional product. This movement through the product takes place in the presence of a

changing concentration gradient. As shown previously, the overall driving force for this transport can be expressed as the change in the concentration gradient. The term "driving force" is used here as it is in common practice to mean the motivation or cause for this transport. The use of this term in this way implies that iron cations are undergoing an accelerated motion in one direction or another. Expressing this driving force in terms of a change in chemical potential further implies that a gradient in activity may be in some way accelerating or "forcing" the cations in that direction. Here, the use of the term is something of a misnomer. The thermal energy of the iron cation is actually what causes the motion of the ion. The presence of a concentration gradient simply biases the direction of motion toward that which opposes the direction of the gradient, i.e. it is more energetically favorable to move in the direction opposing the gradient. This is the basis for diffusive movement as first described by Fick. This is also true in the case of a gradient in chemical activity coefficient across the product. Although this can be described as an additional possible "driving force," it is actually just another example of a directional bias for the thermally generated diffusive movement. However, in the case under consideration here, since the change in P_{LMM} Auger energies through the depth of the product is small, any change in activity coefficient is considered to be inconsequential in this analysis.

The modeling of the measured rate data clearly demonstrates a function whose second derivative is less than zero. This is consistent with past work using TCP and TBPP on ferrous surfaces. Within this past work it has been observed that the function is well fit by a parabolic rate expression. Since this type of parabolic function had been seen in the past resulting from oxidation processes that were controlled by diffusion, it was natural to

assume that this parabolic function similarly indicates a process that is controlled by diffusion as well. As can be seen from the data generated in this work, the rate data is modeled equally well by the parabolic function in time.

The rate law followed in the formation of this product has been shown to be logarithmic at 300° C and parabolic at higher temperatures. This behavior is characteristic of diffusion controlled processes where at relatively low temperature there is little energy available for the diffusion process and hence only a thin layer of product forms. The adherence to these two rate law forms is similar to the process of iron oxidation, i.e. the process follows a logarithmic form at low temperature and a parabolic form at high temperature. This in itself is not evidence for a diffusion controlled process such as the oxidation of iron but is consistent with such a mechanism.

Since the change in the iron concentration gradient is the only significant change in the nature of the system, this change can be taken as the rate controlling step in the product growth process.

The path followed by the moving product through the magnetite phase is not likely to have been ideally straight and likely consisted of irregular deviations. For this reason, the total path length (depth) through which the product moved is likely something greater than that determined by the sputter/AES concentration-depth analysis. For this reason, the estimation of the diffusivity value of $3 \times 10^{-15} \text{ cm}^2/\text{sec}$ should be considered as a conservative estimate.

This value for diffusivity falls between iron's diffusivity in $\text{Fe}_{.907}\text{O}$ and $\text{Fe}_{.748}\text{O}$ as shown in Table 9. In this table the diffusivity of iron has been estimated at a temperature of 500° C using the values for D_0 and Q shown in the table. These values were provided

Table 9. Iron diffusivities in various iron oxides.

Diffusing medium	D_0 , Q	Diffusivity at 500° C	Temperature range (°C)
Fe (BCC)		5.9×10^{-17}	-
Fe _{.907} O	0.118, -29.7	4.7×10^{-10}	700 - 1,000
Fe _{.748} O	5.2, -55.0	1.4×10^{-15}	750 - 1,000
Fe _{.666} O	4×10^5 , -112.0	8.2×10^{-27}	900 - 1,300

in the reference for the temperature ranges shown [124]. The estimated diffusivity of iron in this work is within an order of magnitude of that estimated by Forster [79] using TBPP vapor and a steel surface under dynamic wear conditions at 370° C. There are however significant differences between Forster's work and this work; differences which diminish the importance of a comparison between iron diffusivities. For example, Forester used air as a carrier gas. This inclusion of large amounts of oxygen may have had an effect on the surface reaction. This type of change was been observed experimentally with TCP on the surface of a chrome nickel alloy [68]. Additionally, since in Forster's work the reactions were occurring under dynamic wear conditions, the surface product was continuously being worn away exposing the underlying surface to TBPP vapor as opposed to the exterior surface of the product being exposed to the vapor.

The activation energy estimated for the diffusion controlled process of product formation on iron is characteristic of solid state diffusion processes. The activation energies for the chemical reactions taking place are expected to be lower. Wright [126] has shown that the gas phase decomposition of TBPP at temperatures between 300° and 600° C is characterized by an activation energy of approximately 11 kcal/mole. This decomposition involves the cleavage of the P-O bond of the TBPP molecule. This type of bond breaking would necessarily be involved in the formation of the phosphide form of the product. Makki and Graham [68] have determined that the activation energy for TCP reactions on a stainless steel surface is 13.85 Kcal/mole for short term exposures and 51.9 Kcal/mole for longer exposures. This difference in activation energies coincides with the energies found in this work and implies that the higher value associated with the long term exposures by Makki and Graham could be attributed to a diffusion process

taking place. These values for activation energy are characteristic of a vacancy diffusion mechanism as opposed to an interstitial mechanism.

CHAPTER V

CONCLUSIONS

A thermogravimetric analyzer with modifications has served as a means to quantify the extent and rate of the product formation process resulting from the interaction of vaporous TBPP and various surfaces. The reaction products generated using this device were found to be in all ways similar to the products found by others investigating the reactions of iron with TCP and TBPP vapor at high temperatures. These included phosphide, phosphate and polyphosphate glass as determined by EDS, AES, and FTIR. Although this equipment was not useful in studying the initial reaction process, it was found to be advantageous in making measurements after an initial product had formed on the surface. Since this device provided a nearly continuous recording of product weight as a function of time, the overall form of this function was determined with high resolution. The form of this function of time was found to be logarithmic at relatively low temperatures and parabolic at higher temperatures. This functional form is analogous to that found in the oxidation of iron which is known to be a diffusion controlled process. Based on this analogy, suggestions had been made in past work that the parabolic rate law for aryl phosphates such as TCP and TBPP reacting with iron is an indication that these reactions are also controlled by diffusion processes. Little had been done prior to this work to provide specific evidence regarding the rate controlling mechanism(s). In

particular, the elements that are mobile, the movement of these elements and the driving force for this movement, all of which constitute the mechanism(s). Inasmuch as the diffusion process involved with the iron/platinum laminated foils mimic the processes involved with pure iron, the motilities of these elements have been characterized. Iron appears to be the lone mobile element in the product formation process.

The lack of reactivity displayed between vaporous TBPP and the surfaces of pure iron (III) phosphate and the well known inert surfaces of silicon nitride and platinum demonstrates that iron must be present at the surface of the product in order for the product to formation process to continue. Additionally, the surface iron that becomes part of the product must be continuously re-supplied for further reactions with the vaporous TBPP to take place. The product formation process has been shown to consist of the formation of product at the exterior surface of the product where iron chemically reacts with the TBPP to form the product. The iron continuously diffuses to the exterior surface through the product, originating in the underlying iron layer. This is a type of flat-plate variation of the classic "shrinking core" model for solid-gas reactions. As the thickness of the product layer increases, the diffusion rate of the iron decreases due to a decrease in the iron concentration gradient through the product.

The activation energy and related diffusion parameters for the overall product formation process were estimated. These estimated parameters suggest that the mechanism involves the diffusion of iron by vacancies in the product layer. The change in the concentration gradient of the iron within the product was found to be the lone significant change in the nature of the system and has been concluded to be the rate controlling step in the product formation process.

The diffusivity of the iron is conservatively estimated to be two orders of magnitude higher than iron's self diffusion and consistent with iron in the higher order oxides. This diffusivity is within an order of magnitude of the range found by Forster in his measurements of wear rate in vapor phase lubricated bearings. The estimation of activation energy and the evidence of excess iron vacancies in the substrate indicate that the diffusion of the iron occurs via vacancies rather than interstitials.

CHAPTER VI

RECOMMENDATIONS FOR FUTURE WORK

1. Reaction product characterization. The surface reaction product could be better characterized by examining the chemical constituents of the product using X-ray Photoelectron Spectroscopy (XPS) and X-ray diffraction. In this case, a sample of the product could be grown on an iron surface, removed intact and embedded in a solid matrix oriented on-edge so that the edge of the sample could be easily analyzed. An analysis could be made across this sample edge resulting in a depth profile of the chemistry as it is distributed throughout the thickness of the product. This would provide further insight into the chemical make-up of the reaction product and how the chemistry changes throughout the depth of the product.

2. Effect of stress on product formation. The surfaces of iron samples could be exposed to TBPP vapor at high temperatures while the sample is held in a flexed position. This configuration of the sample would serve to generate tensile stress in the top surface of the iron and compressive stress in the bottom surface. These stresses should have a measurable effect on the rate that iron leaves the interfacial surface of the iron in the formation of the product. This should provide conformational evidence that nonreciprocal diffusion is taking place, i.e. the material under compressive stress should

slow the process if the process consists of material diffusing into the substrate and the material under tensile stress should show the opposite effect.

3. Effect of oxygen in the carrier gas. The form and rate of product formation could be measured for a mixture of TBPP vapor, carrier gas, and varying partial pressures of oxygen. This would provide insight into the role of oxygen in the formation of the product and could identify any possible differences that might be experienced at different altitudes.

4. Differential scanning calorimetric (DSC) measurements. Construct a set of DSC sample pans (top and bottom pieces) from iron foil that are able to be crimped and sealed in the same fashion as the standard aluminum pans. Several of these pans could be pre-oxidized to various extents. DSC measurements could then be performed with a small amount of liquid TBPP within an environment of helium. This may show the location of various exo- and endo-thermic events during the product growth process.

REFERENCES

1. Saba, C., Keller, M., Chao, K., Toth, D., Borchers and M., Smith, H., "Lubricant Evaluation and Performance II," Tech. Rpt., WL-TR-93-2126, Wright Laboratory (Air Force Research Laboratory), Wright-Patterson AFB, Oh., 1994.
2. Rao, A., "Vapor-Phase Lubrication: Application Oriented Development," *Lubr. Eng.*, 1996, pp. 857-862.
3. Perez, J., Ku, C., Hsu, S., "High Temperature Liquid Lubricant for Advanced Engines," SAE Technical Paper, 910454, Warrendale, Pa., 1991.
4. Treuren, K., Barlow, D., Heiser, W., Wagner, M., Forster, N., "Investigation of Vapor-Phase Lubrication in a Gas Turbine Engine," *J. Eng. Gas Turb. Pow.*, 120(2), 1998, pp. 1-8.
5. Ludema, K., in Friction, Wear, Lubrication, a Textbook in Tribology, CRC Press, Inc., New York, 1996, pp. 72-81.
6. Miller, R., in Lubricants and Their Applications, McGraw-Hill, Inc., New York, 1993, pp. 7-11.
7. Wagner, M., Forster N., Teuren, K. and Gerardi, D., "Vapor Phase Lubrication for Expendable Gas Turbine Engines," *J. Eng. Gas Tur. Pow.*, 122, 2000, pp. 185-190.
8. Treuren, K., Barlow, D., Heiser, W., Wagner, M. and Forster, N., "Investigation of Vapor-Phase Lubrication in a Gas Turbine Engine," *J. Eng. Gas Tur. Pow.*, 120, 1998, pp. 257-262.
9. Devine, M., "Lubrication of Ball Bearings With Volatile Organic Compounds," *ASLE Trans.*, 9, 1966, pp. 242-248.

10. Graham, E. and Klaus, E., "Lubrication From the Vapor Phase at High Temperatures," *ASLE Trans.*, 29 (2), 1985, pp. 229-234.
11. Wheeler, D. and Faut, O., "The Adsorption and Thermal Decomposition of Tricresylphosphate (TCP) on Iron and Gold," *App. Sur. Sci.*, 18, 1984, pp. 106-122.
12. Gunsel, S., Klaus, E. and Bruce, R., "Friction Characteristics of Vapor Deposited Lubricant Films," SAE Technical Paper, 890148, Warrendale, Pa., 1989.
13. Hanyaloglu, B. and Graham, E., "Effect of Surface Temperature on vapor Phase Lubrication," *Lubr. Eng.*, 49 (3), 1993, pp. 227-232.
14. Lauer, J. and Dwyer, S., "Tribiochemical Lubrication of Ceramics by Carbonaceous Vapors," *Tri ol. Trans.*, 34 (4), 1991, pp. 521-528.
15. Hanyaloglu, B. and Graham, E., "Vapor Phase Lubrication of Ceramics," *Lubr. Eng.*, 50 (10), 1994, pp. 814-820.
16. Hanyaloglu, B., Fedor, D. and Graham, E., "Vapor Phase Lubrication of a Ni-Based Superalloy," *Lubr. Eng.*, 51 (3), 1995, pp. 252-258.
17. Wheeler, D. and Faut, O., "The Adsorption and Thermal Decomposition of Tricresylphosphate (TCP) on Iron and Gold," *App. Surf. Sci.*, 18, 1984, pp. 106-122.
18. Klaus, E., Jeng, G. and Duda, J., "A Study of Tricresyl Phosphate as a Vapor Delivered Lubricant," *Lubr. Eng.*, 45 (11), 1989, pp. 717-723.
19. Davey, W. and Edwards, E., "The Extreme-Pressure lubricating Properties of Some Sulfides and Disulfides, in Mineral Oil, as Assessed by the Four-Ball Machine," *Wear*, 1, 1957/1958, pp. 291-304.
20. Davey, W., "The Development of Extreme Pressure Lubricating Properties by Reactive Sulfur in Mineral Oils," *J. Inst. Pet.*, 31, 1945, pp. 154-158.
21. Davey, W., "The Extreme Pressure Lubricating Properties of Some Chlorinated Compounds as Assessed by the Four-Ball Machine," *J. Inst. Pet.*, 31, 1945, pp. 73-88.
22. Prutton, C., Turnbull, D. and Dlouhy, G., "Mechanism of Action of Organic Chlorine and Sulphur Compounds in Extreme-Pressure Lubrication," *J. Inst. Pet.*, 32, 1946, pp. 90-118.
23. Godfrey, D., "Chemical Changes in Steel Surfaces During Extreme Pressure Lubrication," *ASLE Trans.*, 5, 1962, pp. 57-66.

24. Placek, D. and Shankwalkar, S., "Phosphate Ester Surface Treatment for Reduced Wear and Corrosion Protection," *Wear*, 173, 1994, pp. 207-217.
25. Barnick, N., Blanchet, T., Sawyer, W. and Gardner, J., "High Temperature Lubrication of Various Ceramics and Metal Alloys via Directed Hydrocarbon Feed Gases," *Wear*, 214, 1998, pp. 131-138.
26. Latendresse, J., Brooks, C. and Capen, C., "Pathologic Effects of Butylated Triphenyl Phosphate-Based Hydraulic Fluid and Tricresyl Phosphate on the Adrenal Gland, Ovary, and Testis in the Fischer-344 Rat," *Tox. Pathol.*, 22 (4), 1994, pp. 341-352.
27. Shubkin, R., in Synthetic Lubricant and High-Performance Functional Fluids, Marcel Dekker, Inc., New York, 1993, pp. 70-72.
28. Johannsen, F., Wright, P., Gordon, D., Levinskas, G., Radue, R. and Graham, P., "Evaluation of Delayed Neurotoxicity and Dose-Response Relationships of Phosphate Esters in the Adult Hen," *Tox. Appl. Pharm.*, 41, 1977, pp. 291-304.
29. Johnson, M., "Organophosphates and Delayed Neuropathy-Is NTE Alive and Well?," *Tox. Appl. Pharm.*, 102, 1990, pp. 385-399.
30. Kinkead, E., Wolfe, R., Salins, S. Godin, C. and Flemming, C., "Acute Delayed Neurotoxicity Evaluation of Two Jet Engine Oils Using a Modified Navy and EPA Protocol," Tech. Rpt., AL-TR-1992-0115, Armstrong Laboratory, Wright-Patterson AFB, Oh., 1992.
31. Latendresse, J., Azhar, S., Brooks, C. and Capen, C., "Pathogenesis of Cholesteryl Lipidosis of Adrenocortical and Ovarian Interstitial Cells in F344 Rats Caused by Tricresyl Phosphate and Butylated Triphenyl Phosphate," *Tribol. Appl. Pharm.*, 122, 1993, pp. 281-289.
32. Wright, R., "The Gas Phase Decomposition and Trimethylolpropane Phosphate Neurotoxin Formation Potential of Tricresyl and tert-Butylphenyl Phosphates," Ph.D. Dissertation, University of Dayton, 1995.
33. Klaus, E., Duda, J. and Chao, K., "A Study of Wear Chemistry Using a Micro Sample Four-Ball Wear Test," *Tribol. Trans.*, 34 (3), 1991, pp. 426-432.
34. Smith, J., Furey, M. and Kajdas, C., "An Exploratory Study of Vapor-phase Lubrication of Ceramics by Monomers," *Wear*, 181-183, 1995, pp. 581-593.

35. Dekoven, B. and Mitchell, G., "HREELS, XPS and In-Situ Friction Studies of Thin Polyphenyl Ether Films on Steel Surfaces," *App. Surf. Sci.*, 52, 1991, pp. 215-226.
36. Clark, D., Klaus, E. and Hsu, S., "The Role of Iron and Copper in the Oxidation Degradation of Lubricating Oils," *Lubr. Eng.*, 41 (5), 1984, pp. 280-287.
37. Masuko, M. and Kamio, N., "Comparison of Reacted Film Formation of Three Different Types of Perfluoropolyethers With a Heated Steel Surface," *Tribol. Trans.*, 41 (2), 1998, pp. 241-246.
38. Cowley, C., Ultee, C. and West, C., "Influence of Temperature on Boundary Lubrication," *Lubr. Sci. Technol.*, 1 (2), 1958, pp. 281-286.
39. Beeck, O., Givens, J. and Williams, E., "On the Mechanism of Boundary Lubrication II. Wear Prevention by Addition Agents," *Proc. Roy. Soc. (London)*, A177, 1940, pp. 103-118.
40. Klaus, E., Tewksbury, E. and Fenske, M., "Critical Comparison of Several Fluids as High Temperature Lubricants," *J. Chem. Eng. Data*, 6(1), 1961, pp. 99-106.
41. Bowden, F. and Tabor, D., in The Friction and Lubrication of Solids, Part II, The Clarendon Press, Oxford, 1964, pp. 358-359.
42. Furey, M., "Surface Roughness Effects on Metallic Contact and Friction," *ASLE Trans.*, 6, 1963, pp. 49-59.
43. Grownweg N., Hakim, N., Barber, G. and Klaus, E., "Vapor Delivered Lubrication of Diesel Engines-Cylinder Kit Rig Simulation," *Lubr. Eng.*, 47 (12), 1991, pp. 1035-1039.
44. Godfrey, D., "The lubrication Mechanism of Tricresyl Phosphate on Steel," *ASLE Trans.*, 8, 1965, pp. 1-11.
45. Barcroft, F., "A Technique for Investigating Reactions Between E. P. Additives and Metal Surfaces at High Temperatures," *Wear*, 3, 1960, pp. 440-453.
46. Borsoff, V., "On the Mechanism of Gear Lubrication," *J. Bas. Eng.*, Series D, 81, 1959, pp. 79-93.
47. Tung, S., Smolenski, D. and Wang, S., "Determination of Differences in Tribological Behavior and Surface Morphology Between Electrodeposited and Traditional Phosphate Coatings," *Thin Solid Films*, 200, 1991, pp. 247-261.

48. Klaus, E. and Bieber, H., "Effects of P³² Impurities on the Behavior of Tricresyl Phosphate-32 as an Antiwear Additive," *ASLE Trans.*, 8, 1965, pp. 12-20.
49. Bieber, H., Klaus, E. and Tewksbury, E., "A Study of Tricresyl Phosphate as an Additive for Boundary Lubrication," *ASLE Trans.*, 11, 1968, pp. 155-161.
50. Murphy, C., Ravner, H. and Timmons, C., "Factors Influencing the Lead Corrosivity of Ester Oils During Long-Term Storage," *J. Chem. Eng. Data*, 6(1), 1961, pp. 135-141.
51. Higgins, C. and Baldwin, W., "The Thermal Decomposition of Tributyl Phosphate," *J. Org. Chem.*, 26, 1961, pp. 846-850.
52. Chiantella, A., Affens, W. and Johnson, E., "Effect of High Temperatures on Stability and Ignition Properties of Commercial Triaryl Phosphate Fluids," *I & E C Prod. Res. Dev.*, 2, 1963, pp. 79-84.
53. Barcroft, F. and Daniel, S., "The Action of Neutral Organic Phosphates as EP Additives," *J. Bas. Eng.*, 87, 1965, pp. 761-770.
54. Goldblatt, I. and Appeldoorn, J., "Antiwear Behavior of Tricresylphosphate (TCP) in Different Atmospheres and Different Base Stocks," *ASLE Trans.*, 13(3), 1970, pp. 203-214.
55. Sanin, P., Shepeleva, E., Mannik, A. and Kleimenov, B., "Chemical Modification of Friction Surfaces," *J. Bas. Eng.*, 87D, 1965, pp. 771-777.
56. Donovan, M., Scott, J. and Shreir, L., "Phosphoric Acid Treatments for Steel. I. The Nature of Coatings Produced by the Action of Phosphoric Acid on Steel," *J. App. Chem.*, 8(2), 1958, pp. 87-95.
57. Faut, O. and Wheeler, D., "Mechanism of Lubrication by Tricresylphosphate (TCP)," Tech. Rpt. No. 2053, NASA Technical Information Branch, Washington, D. C., 1983.
58. Shafrin, E. and Murday, J., "Analytical approach to ball-bearing surface chemistry," *J. Vac. Sci. Technol.*, 14(1), 1977, pp. 246-253.
59. Shafrin, E. and Murday, J., "Auger Compositional Analysis of Ball Bearing Steels Reacted with Tricresyl Phosphate," *ASLE Trans.*, 21(4), 1978, pp. 329-336.
60. Kasrai, M., Fuller, M., Scaini, M., Yin, Z., Brunner, R., Bancroft, G., Fleet, M., Fyfe, K. and Tan, K., "Study of Tribochemical Film Formation Using X-ray Absorption and Photoelectron Spectroscopies," *Lubricants & Lubrication*, 1995, pp. 659-669.

61. Kasrai, M., Cutler, J., Gore, K., Canning, G. and Bancroft, G., "The Chemistry of Antiwear Films Generated by the Combination of ZDDP and MoDTC Examined by X-ray Absorption Spectroscopy," *Trib. Trans.*, 41(1), 1998, pp. 69-77.
62. Fuller, M., Yin, Z., Kasrai, M., Bancroft, G., Yamaguchi, E., Ryason, P., Willermet, P. and Tan, K., "Chemical Characterization of Tribochemical and Thermal Films Generated From Neutral and Basic ZDDPs Using X-ray Absorption Spectroscopy," *Trib. Int.*, 30(4), 1997, pp. 305-315.
63. Cann, P. and Spikes, H., "In Lubro Studies of Lubricants in EHD Contacts Using FTIR Absorption Spectroscopy," *Trib. Trans.*, 34(2), 1991, pp. 248-256.
64. Ma, Y., Liu, J., Wu, Y. and Gu, Z., "The Effect of Oxy-Nitrided Steel Surface on Improving the Lubricating Performance of Tricresyl Phosphate," *Wear*, 20, 1997, pp. 287-290.
65. Wang, S. and Tung, S., "A Reaction Mechanism for Producing Low-Friction Iron Phosphate Coatings," *Trib. Trans.*, 34(1), 1991, pp. 45-50.
66. Lacey, I., Kelsall, H. and Spikes, H., "Thick Antiwear Films in Elastohydrodynamic Contacts. Part II: Chemical Nature of the Deposited Film," *ASLE Trans.*, 29(3), 1985, pp. 306-311.
67. Makki, J. and Graham, E., "Formation of Solid Films From the Vapor Phase on High Temperature Surfaces," *Lub. Eng.*, 47(3), 1991, pp. 199-206.
68. Makki, J. and Graham, E., "Vapor Phase Deposition on High Temperature Surfaces," *Tribol. Trans.*, 33 (4), 1990, 595-603.
69. Forster, N. and Trivedi, H., "Rolling Contact Testing of Vapor Phase Lubricants-Part I: Material Evaluation," *Tribol. Trans.*, 40 (3), 1997, pp. 421-428.
70. Forster, N. and Trivedi, H., "Rolling Contact Testing of Vapor Phase Lubricant-Part II: System Performance Evaluation," *Tribol. Trans.*, 40 (3), 1997, pp. 493-499.
71. Liu, W., Klaus, E. and Duda, J., "Wear Behavior of Steel-On-Si₃N₄ and Si₃N₄-On-Si₃N₄ Systems With Vapor Phase Lubrication of Oleic Acid and TCP," *Wear*, 214, 1998, pp. 207-211.
72. Johnson, D., Morrow, S., Forster, N. and Saba, C., "Vapor Phase Lubrication: Reaction of Phosphate Ester Vapors with Iron and Steel," *Chem. Mater.*, 14, 2002, pp. 3767-3775.

73. Saba, C. and Forster, N., "Reactions of Aromatic Phosphate Esters with Metals and Their Oxides," *Trib. Let.*, 12(2), 2002, pp. 135-146.
74. Paciorek, K., Kratzer, R., Kaufman, J., Nakahara, J., Christos, T. and Hartstein, A., "Thermal Oxidative Degradation Studies of Phosphate Esters," *J. Am. Ind. Hyg. Assoc.*, 39(7), 1978, pp. 633-639.
75. Paciorek, K., Kratzer, R., Kaufman, J., Nakahara, J. and Hartstein, A., "Thermal Oxidative Decomposition Studies of Neoprene Compositions," *J. Am. Ind. Hyg. Assoc.*, 36(10), 1975, pp. 10-16.
76. Sung, D. and Gellman, A., "The surface chemistry of alkyl and arylphosphate vapor phase lubricants on Fe foil," *Trib. Int.*, 35, 2002, pp. 579-590.
77. Sung, D. and Gellman, A., "Thermal decomposition of tricresylphosphate isomers on Fe," *Trib. Let.*, 13(1), 2002, pp. 9-14.
78. Klaus, E., Duda, J., Jeng, G., Hakim, N., Groeneweg, M. and Balnaves, M., "Vapor Phase Tribology for Advanced Diesel Engines," SAE Technical Paper, 890889, Warrendale, Pa., 1989.
79. Forster, N., "High Temperature Lubrication of Rolling Contacts With Lubricants Delivered From the Vapor Phase and as Oil-Mists," Tech. Rpt., WL-TR-97-2003, Wright Laboratory, Wright-Patterson AFB, Oh., 1997.
80. Forster, N., "Rolling Contact Testing of Vapor Phase Lubricants-Part IV: Diffusion Mechanisms," STLE Preprint, 98-AM-2A-I, 1998.
81. Hamilton, L., in Regression With Graphics, A Second Course in Applied Statistics, Duxbury Press, California, 1992, pp. 163-167.
82. Yin, Z., Kasrai, M., Fuller, M., Bancroft, G., Fyfe, K. and Tan, K., "Application of soft X-ray absorption spectroscopy in chemical characterization of antiwear films generated by ZDDP Part I: the effects of physical parameters," *Wear*, 202, 1997, pp. 172-191.
83. Shubkin, R., in Synthetic Lubricant and High-Performance Functional Fluids, Marcel Dekker, Inc., New York, 1993, pp. 80-85.
84. Wright, R., "The Gas Phase Decomposition and Trimethylolpropane Phosphate Neurotoxin Formation Potential of Tricresyl and tert-Butylphenyl Phosphates," Ph. D. Dissertation, University of Dayton, 1995, pp. 48.

85. Wright, R., "The Gas Phase Decomposition and Trimethylolpropane Phosphae Neurotoxin Formation Potential of Tricresyl and tert-Butylphenyl Phosphates," Ph. D. Dissertation, University of Dayton, 1995, pp. 48-56.
86. Perry, A., Green, D. and Maloney, J. (ed), Perry's Chemical Engineers' Handbook, McGraw-Hill Inc., New York, 1984, pp. 5-6.
87. Perry, A., Green, D. and Maloney, J. (ed), Perry's Chemical Engineers' Handbook, McGraw-Hill Inc., New York, 1984, pp. 3-249, 3-250.
88. Want, C., Duda, J. and Klaus, E., "A Kinetic Model of Lubricant Deposit Formation Under Thin Film Conditions," *Tribol. Trans.*, 37(1), 1994, pp. 168-174.
89. Wright, R., "The Gas Phase Decomposition and Trimethylolpropane Phosphae Neurotoxin Formation Potential of Tricresyl and tert-Butylphenyl Phosphates," Ph. D. Dissertation, University of Dayton, 1995, pp.
90. Dulcy, C., Lin, M. and Hsu, C., "Thermal Desorption of the PO Radical From Polycrystalline Pt Surfaces," *Chem. Phys. Lett.*, 115(6), 1985, pp. 481-485.
91. Henderson, M. and White, J., "Adsorption and Decomposition of Dimethyl Methylphosphonate on Platinum (111)," *J. Am. Chem. Soc.*, 110, 1988, pp. 6939-6947.
92. Stuve, E., Madix, R. and Sexton, B., "An EELS Study of CO₂ and CO₃ Adsorbed on Oxygen Covered Ag(110)," *Chem. Phys. Lett.*, 89(1), 1982, pp. 48-53.
93. Matsumoto, T., Kubota, J., Kondo, J., Hirose, C. and Domen, K., "Adsorption Structures of Carbon Dioxide on NiO(111) and Hydroxylated NiO(111) Studied by Infrared Reflection Adsorption Spectroscopy," *Langmuir*, 15, 1999, pp. 2158-2161.
94. Nyquist, R. and Kagel, R. in Infrared Spectra of Inorganic Compounds, Academic Press, Inc., New York, 1971, pp. 170-174.
95. Forster, N., "Rolling Contact Testing of Vapor Phase Lubricants-Part III: Surface Analysis," *Tribol. Trans.*, 42(1), 1999, pp. 1-9.
96. Corbridge, D.E.C. in Topics in Phosphorous Chemistry, No. 6, University of Leeds, Leeds, 1969, pp. 280-281.
97. Bellamy, L. J. in The Infrared Spectra of Complex Molecules, Richard Clay & Co. Ltd., Bungay, 1958, pp. 324-325.

98. Silverstein, R., Bassler, G. and Morrill, T. in Spectrometric Identification of Organic Compounds, John Wiley & Sons, New York, 1981, pp. 109-153.
99. Muneyama, E., Kunishige, A., Ohdan, K. and Ai, M., "Reduction and Reoxidation of Iron Phosphate and Its Catalytic Activity for Oxidative Dehydrogenation of Isobutyric Acid," *J. Cat.*, 158, 1996, pp. 378-384.
100. Fang, X., Ray, C., Milankovic, A. and Day, D., "Iron Redox Equilibrium, Structure, and Properties of Iron Phosphate Glasses," *J. Non-Crystalline Solids*, 283, 2001, pp. 162-172.
101. Moedritzer, K., "Synthesis and Properties of Phosphinic and Phosphonic Acid Anhydrides," *140th Meeting of the American Chemical Society*, Chicago, Ill., 1961, pp. 4381-4384.
102. Corbridge, D. E. C., "The Infrared Spectra of Phosphorous Compounds," *Topics in Phosphorous Chemistry*, No. 6, 1969, pp. 235-365.
103. Balamurugan, A., Kannan, S., Selvaraj, V. and Rajeswari, S., "Development and Spectral Characterization of Poly(Methyl Methacrylate)/Hydroxyapatite Composite for Biomedical Applications," *Trends Biomater. Artif. Organs*, 18 (1), 2004, pp. 41-45.
104. Saba, C. and Forster, N., "Reactions of Aromatic Phosphate Esters with Metals and Their Oxides," *Tribology Letters*, 12 (2), 2002, pp. 135-146..
105. Nowacki, J., "Morphology and Properties of Phospho-Nitrided Layers," *Proc. Fourth ASM Heat Treat. Surf. Eng. Conf.*, 1998, pp. 263-266.
106. Ma, Y., "The Effect of Oxy-Nitrided Steel Surface on Improving the Lubrication Performance of Tricresylphosphate," *Wear*, 210, 1997, pp. 287-290.
107. Takaki, S. and Nakamura, N., "Metallurgy of Nitrogen Absorption Process in High Cr Steels," *Mat. Sci. For.*, 318-320, 1999, pp. 723-732.
108. Takaki, S. and Nakamura, N., "Structural Control of Stainless Steel by Nitrogen Absorption in Solid State," *ISIJ Inter.*, 36 (7), 1996, pp. 922-926.
109. Williams, R. and Homerberg, V. in Principles of Metallography, McGraw-Hill Book Company, Inc., New York, 1948, pp. 162-164.
110. Twigg, M. (ed), Catalyst Handbook, Manson Publishing Ltd., Frome, 1996, pp.

111. Firebaugh, S., Jensen, K. and Schmidt, M., "Investigation of High-Temperature Degradation of Platinum Thin Films with an In Situ Resistance Measurement Apparatus," *J. Microele. Syst.*, 7(1), 1998, pp. 128-135.
112. Lee, W. and Oblas, C., "Argon entrapment in metal films by dc triode sputtering," *J. App. Phys.*, 46(4), 1975, pp. 1728-1732.
113. Cuomo, J. and Gambino, R., "Incorporation of rare gases in sputtered amorphous metal films," *J. Vac. Sci. Tech.*, 14(1), 1977, pp. 152-157.
114. Lee, W. and Oblas, D., "Argon Concentration in Tungsten Films Deposited by dc Sputtering," *J. Vac. Sci. Tech.*, 7, pp. 129-133.
115. Winters, H. and Kay, E., "Gas Incorporation into Sputtered Films," *J. Appl. Phys.*, 38(10), 1967, pp. 3928-3934.
116. Schroder, D., Fiedler, A., Schwarz, J. and Schwarz, H., "Generation and Characterization of the Anionic, Neutral, and Cationic Iron-Dioxygen Adducts [FeO₂] in the Gas Phase," *Inorg. Chem.*, 33, 1994, pp. 5094-5100.
117. Li, R., Hanold, K., Garner, M., Luong, A. and Continetti, R., "Excited state dynamics in clusters of oxygen," *Faraday Discuss.*, 108, 1997, pp. 115-130.
118. Wang, L., Wu, H. and Desai, S., "Sequential Oxygen Atom Chemisorption on Surfaces of Small Iron Clusters," *Phys. Rev. Lett.*, 76(25), 1996, pp. 4853-4856.
119. Osgerby, "Oxide Scale Damage and Spallation in P92 Martensitic Steel," *Materials at High Temperatures*, 17 (2), 2000, pp. 307-310.
120. Smentkowski, V. and Yates, J., "The Adsorption of Oxygen on Fe(110) in the Temperature Range of 90 to 920K," *Sur. Sci.*, 232, 1990, pp. 113-128.
121. Madden, H., "Chemical Information From Auger Electron Spectroscopy," *J. Vac. Sci., Tech.*, 18(3), 1981, pp. 67-689.
122. Askeland, D. in The Science and Engineering of Materials, PWS Publishing Co., Boston, 1994, pp. 419.
123. Bernett, M., Murday, J. and Turner, N., "An Interpretation of the Auger LVV Transitions From Oxides of Third-row Elements," *J. Elec. Spec. Rel. Phen.*, 12, 1977, pp. 375-393.

124. Hauffe, K. in Oxidation of Metals, Plenum Press, New York, 1965, pp. 282-285.
125. Klaus, E., Phillips, J., Lin, S., Wu, N. and Duda, J., "Structure of Films Formed During the Deposition of Lubrication Molecules on Iron and Silicon Carbide," *Tribol. Trans.*, 33 (1), 1990, pp. 25-32.
126. Wright, R., "The Gas Phase Decomposition and Trimethylolpropane Phosphate Neurotoxin Formation Potential of Tricresyl and tert-Butylphenyl Phosphates," Ph.D. Dissertation, University of Dayton, 1995.

R702033408